NORTHWESTERN UNIVERSITY

Multiscale Modeling and Mechanics of Graphene-based Nanomaterials and Carbon Fiber Reinforced Epoxy Resin Composites

A DISSERTATION

SUBMITTED TO THE GRADUATE SCHOOL

IN PARTIAL FULFILLMENT OF THE REQUIREMENTS

for the degree

DOCTOR OF PHILOSOPHY

Field of Civil and Environmental Engineering

By

Zhaoxu Meng

EVANSTON, ILLINOIS

September 2018

ABSTRACT

Carbon-based materials, such as graphene and carbon fibers, have good prospects for applications in reinforcements of polymers as advanced structural composites. Hence, the study of the mechanical properties of the constituents and the composites is becoming increasingly popular in both academia and industry.

Graphene has been shown to have a comparative advantage over traditional materials as composite reinforcements. There is a rapid rise of interest in harnessing the mechanical properties of graphene and its derivatives, like graphene oxide (GO), at larger length scales and higher material hierarchies, i.e. multi-layer assemblies. Despite the great progress in developing synthesis and characterization methods for these materials, the physical mechanisms governing the mechanical performance of multi-layer graphene (MLG) and GO sheets remain poorly understood. Experimental techniques offer limited insights into atomic-scale deformation processes, while atomistic simulations have proved prohibitively expensive in investigating the large-deformation and failure mechanisms of the multi-layer assemblies. Similar bottlenecks also exist for the characterization of matrix materials, such as epoxy resins. Previous atomistic investigations of epoxy resins fall short in linking nanoscopic observations to macroscopic properties, and thus, it limits the use of simulations in the computational design of new materials.

To overcome these critical issues, we first develop coarse-grained (CG) models of MLG and GO sheets, which are incorporated into molecular dynamics (MD) simulations that are capable of quantitatively reproducing their mechanical responses in both elastic and fracture regimes. Additionally, the CG model of GO accurately captures the heterogeneous mechanical properties of GO with different chemistries. With two to three orders of magnitude increase in computational efficiency, CG MD simulations are then used to elucidate the mechanisms of deformation and

failure of MLG and GO sheets by collaborating with experimentalists. Specifically, we discover for the first time an atomic-level interlayer slippage process in MLG, which leads to repeatable energy dissipation of MLG sheets under film deflection tests. We also successfully elucidate the experimentally measured thickness-dependent strength of MLG sheets. In addition, differences in the failure modes of GO membranes under nanoindentation are shown to be due to differences in the chemistries of the contact area. We also show the potential of these CG models to study the fracture toughness of mesoscale graphene and GO sheets, as well as to investigate the mechanical properties and failure mechanisms of nacre-inspired nanocomposites. We also utilize our CG MD approach to study the ballistic impact behavior of thin MLG sheets. The simulation results reveal distinctive failure mechanisms that deteriorate the ballistic resistance of MLG sheets. Specifically, we have observed the in-plane cone wave formed upon impact can reflect from clamped boundaries and induce early perforation. In addition, the compressive wave in the thickness direction could result in spalling-like failure, similarly to the failure mechanism in the impact on macroscopic concrete specimen. To relate the observed failure mechanisms to microballistic experiments, we also develop analytical relationships, based on continuum mechanics theories, to bridge the size scales and provide a full picture of the deformation processes.

Among all the matrix materials, epoxy resin is promising in graphene-based nanocomposites as well as in carbon fiber reinforced composites with its excellent mechanical properties and temperature resistance. However, developing new and better ones always take a long time as we have limited understanding of the physics underlying their properties. To characterize its structure-property relationship from molecular scale, we first develop a robust atomistic model for its crosslinked structure and investigate the effect of resin functionality, crosslink degree, and component ratio on resin thermomechanical properties. More importantly, we link atomistic tensile

simulations of the resin with its macroscopic fracture energy, using a theoretical fracture mechanics model developed for the polymeric system. With this theoretical model, we also provide physical insight into the molecular mechanisms that govern the fracture characteristics of epoxy resins. Then, to establish the structure-property relationship of carbon fiber composites from a multiscale perspective, we utilize MD simulation results and an analytical gradient model to characterize the properties of the interphase region between fiber and matrix, which are then integrated into finite element analysis to investigate the failure behavior of composites. Using this multiscale framework, we explicitly elucidate that the nanoscale interphase region is crucial to capture the realistic mechanical properties of composites, especially the non-linear response at large deformation.

The studies presented here illustrate important mesoscale physical mechanisms governing the mechanical performance of composite constituents such as MLG and GO sheets and epoxy resins as well as the entire composites. The insights obtained from the studies would lay the foundation for developing future impact and failure resistant composites.

Thesis Advisor:

Dr. Sinan Keten

Department of Civil and Environmental Engineering and Department of Mechanical Engineering

Final Examination Committee:

Dr. Sinan Keten (Chair)

Dr. Horacio D. Espinosa

Dr. Gregory Wagner

ACKNOWLEDGEMENTS

I am extremely lucky to be surrounded by many excellent people that help and support me during my Ph. D. study and life here at Northwestern University.

I would first like to thank my advisor, Professor Sinan Keten, for leading me to the exciting world of nanomaterials and computational mechanics, and for his continued support and guidance throughout the entirety of my graduate research. I am always inspired by his commitment to research and teaching and all the outstanding accomplishments of our group. Throughout the years, he has been a tremendous source of inspiration, which motivates me to address challenging scientific problems as well as develop impactful research projects. This fantastic five-year journey would not have been possibly made without his guidance and mentoring.

I would like to thank my dissertation committee members, Prof. Horacio D. Espinosa and Prof. Gregory Wagner. I feel privileged to have the opportunity to collaborate with Prof. Espinosa on the graphene-based nanomaterials project, and I have benefited from every discussion. His mentorship and support give me further confidence in my future endeavor. I thank Prof. Wagner for showing me the enthusiasm and genuineness in research and teaching, which has been a true inspiration for me in my graduate study. I also thank Prof. Wing Kam Liu for his valuable advice on my research and for being part of the thesis proposal committee.

I would like to thank my many other collaborators that have provided invaluable guidance, support, and discussion. I have had the opportunity to collaborate experimentally with Dr. Xiaoding Wei on the graphene-based nanomaterials project. The experimental efforts have been greatly beneficial in characterizing the physical mechanisms of multilayer graphene sheets. I thank Dr. Rafael A. Soler-Crespo and Dr. Wei Gao for their input in the atomistic calculation of graphene

oxide. I have also had the opportunity to collaborate experimentally with Dr. Xuming Su, Dr. Danielle Zeng and Mr. Qingping Sun. These collaborations have led to meaningful and fruitful research and helped enhance the impact of our work by linking the atomistic level characterization of epoxy resins with multiscale modeling of carbon fiber reinforced epoxy resin composites.

I would also like to thank my colleagues and friends for their friendship and support. It is a great honor to work and collaborate with such an outstanding team in our group. Thanks to Wenjie Xia, Robert Sinko, David D. Hsu, and Luis Ruiz for their great help when I first joined the group. Their commitment to research and the fruitful discussions with them motivate me a lot during my graduate study. Thanks to Yao Zhang, Xin Qin, Elizabeth DeBenedictis, Dan Ma and Benjamin Marchi for their fruitful discussion in research and great help in life. I would like to thank my friend, Jialun Han, for going to the gym with me every day and for sincerely sharing each other's sorrow or joy. I would also like to thank my friend and roommate, Hai-xin Lin, for inspiring me in research and cooking dinner for me. Thank you to my many other friends as well.

Last but not least, my warmest feelings and deepest thanks to my loving parents, my mom Aituan Ma and my dad Ligen Meng, who have always wholeheartedly supported me during my graduate studies, and to my friend for life, my soulmate, and my girlfriend, Guanyu Wang, for her constant source of support and encouragement. I feel blessed to have them by my side.

This work is mainly supported by the Ford Motor Company with funding from the U.S. Department of Energy under award DE-EE0006867. I also acknowledge the funding by the Army Research Office under award #W911NF1710430. I acknowledge the great support from the Department of Civil and Environmental Engineering and Mechanical Engineering at Northwestern University. The main computational work has been done through the supercomputing grants from Northwestern University High Performance Computing Center.

DEDICATION

I dedicate this dissertation to my loving parents, Aituan Ma and Ligen Meng, and to my girlfriend, Guanyu Wang, because without their love and support none of this would have been possible.

Table of Contents

Table of Figures

Table of Tables

Chapter 1: Introduction and Background

In this chapter, I will start with the Introduction and Background of my Ph.D. dissertation, which focuses on the multiscale modeling and mechanics of graphene-based nanomaterials and carbon fiber reinforced epoxy resin composites. The overall objective of my research is to explore molecular and meso-scale mechanisms governing the mechanical performance of carbon-based materials and their polymers composites. In the first section, I will briefly introduce the "wonder material" - graphene, its derivative graphene oxide, and their related nanocomposites. I will highlight their excellent mechanical properties and applications for structural materials. In the following section, I will introduce typical matrix polymeric materials used in nanocomposites and composites. Then, in the third section, I will discuss the common characterization methods for investigating mechanical properties of nanomaterials and composites. I will conclude the chapter with an overview of the entire dissertation and how different characterization methods have been utilized to investigate the mechanics of graphene-based nanomaterials and carbon fiber reinforced epoxy resin composites.

1.1 The era of graphene and its related nanocomposites

Graphene, a so-called "wonder material", has been attracting worldwide interest since the first report of its existence [1]. This is not surprising given that its 2D-atomic crystal structure with covalently bonded carbon atoms possesses unique properties such as high thermal and electrical conductivity [2], large surface area [3], high elastic modulus and intrinsic strength [4]. Graphene has been applied in the areas such as high-performance composite materials [5-7], electronics [8], strain sensors [9-11], hydrogen storage [12], supercapacitors [13, 14], and solar cells [15, 16]. Among all these applications, graphene-based nanomaterials and composites in structural applications are becoming increasingly popular. Pristine graphene has the highest recorded elastic

modulus (1 *TPa*) and intrinsic strength (~120 *GPa*) [4]. This extraordinary mechanical strength gives graphene a comparative advantage over other reinforced fillers commonly used in structural materials [17]. To achieve its theoretical intrinsic strength, it requires high-quality graphene with defect-free lattices [18-20]. While it is still challenging to fabricate inch-size single-crystalline graphene, large-area polycrystalline graphene (poly-graphene) containing internal grain boundaries and defects has been successfully synthesized via chemical vapor deposition (CVD) [21]. The strength of poly-graphene is substantially lower than the intrinsic strength of pristine graphene, but still higher than most of the engineering materials [22-24]. Interestingly, the fracture toughness of poly-graphene was found to be higher than that of pristine graphene due to the branching of the cracks during fracture [25-28], which demonstrates the idea of utilizing geometrical and topological engineering concepts to make poly-graphene a better candidate than pristine graphene for structural applications.

Graphene oxide (GO), a derivative of graphene, contains oxygen-rich functional groups, which deteriorates its mechanical and electronical properties compared to pristine graphene. However, these functional groups also facilitate the dispersion of GO flakes in many solvents and polymer matrices [29-31], which allows facile preparation of polymer nanocomposites and scale-up production of GO. In addition, enhancement of damage tolerance and the interfacial interactions among GO layers, as well as between GO and matrix materials make GO a more favorable reinforcement [32-37]. There is an increasing amount of evidence that the key factor governing the mechanical response of composites is not the stiffness of reinforcements, but the interfacial interactions between the reinforcement and the matrix [7, 17, 38, 39]. Moreover, it has been reported that thermal stability of polymers could be greatly improved by incorporation of GO sheets [40, 41].

Production and preparation of graphene-based nanocomposites have been widely studied in the materials community. The most important aspect during the preparation of such nanocomposites is to ensure that graphene or GO flakes disperse adequately within the matrix. To design the optimal filler geometry, people often refer to biological materials for inspiration. Nacre, possessing both high strength and toughness after billions of years of evolution [42], has been a source of inspiration in the design of nanocomposites [43, 44]. The nacre-inspired nanocomposites possess a brick and mortar layered architecture. They overcome the bottleneck of traditional nanocomposites, such as poor dispersion, low loading, and weak interface interactions [45-48]. Many nanocomposite fabrication strategies have been presented in the literature. Among these, layer by layer assembly [49, 50] and vacuum-assisted filtration self-assembly [51] are two versatile techniques that are promising for preparing nacre-inspired nanocomposites. Recently, nacre-inspired nanocomposites with graphene and GO serving as the brick building block have been fabricated and shown excellent mechanical properties [46, 51]. Such nanocomposites demonstrate promise for applications in many fields, including aerospace, race cars, and flexible electronic devices [52-54].

1.2 Matrix materials used in composites

As alluded to in the previous section, one of the most popular matrix materials used in composites is polymeric materials. Depending on the chemical structures of the polymers (or how the polymers chains are linked), the polymers can be classified as thermoplastics or thermosets polymers [55]. Methacrylate-based polymers are an important family of thermoplastics. They have been widely used in manufacturing thin films, nanocomposites, and nanoelectronics because they are easily processable and they possess remarkable mechanical properties [56-58]. In the category of thermosets polymers, epoxy resins, characterized by a highly crosslinked structure that evolves

during the curing process [59], possess excellent thermomechanical properties as well as good bonding quality to reinforcements. Epoxy resins generally have higher stiffnesses than thermoplastic polymers due to their crosslinked nature, and they are better suited to high-temperature applications as the crosslinking gives rise to higher glass transition temperatures [60]. Epoxy resins have been applied in wide range of areas, most notably as structural adhesives and matrix materials in graphene-reinforce nanocomposites and fiber-reinforced composites. In Chapter 6, I will present a framework for the characterization of thermomechanical properties of epoxy resins. In Chapter 7, I will discuss designing and characterizing nacre-inspired nanocomposites system with poly (methyl methacrylate) (PMMA) as matrix material.

1.3 Characterization methods for mechanical properties of materials

Typically, there are three approaches in scientific research: experimental, analytical, and computational methods. The experimental method is usually the most convincible, but also very challenging to conduct, especially at the nanoscale. The analytical (or theoretical) method has the capability to generalize a scientific finding into broader principles so that it can be broadly applicable to similar systems and processes. The computational method has the ability to provide insights into problems that are hard to be tackled analytically or experimentally. During scientific research, it is always better and more valuable to integrate more methods together.

A variety of recently developed experimental characterization techniques have been used to investigate the properties of carbon-based nanoscale materials. Here, I would like to mention several of them. Raman spectroscopy has been proved useful in characterization and study of the mechanical properties of graphene flakes and their interfacial stress transfer capability. Atomic force microscopy (AFM) has been used to characterize the number of graphene layers [1]. In addition, it has been used to indent free-standing monolayer graphene to measure its mechanical

properties [4]. Laser-induced projectile impact tests (LIPIT) [61] were recently used to investigate the dynamic mechanical behavior of multi-layer graphene (MLG) sheets under micron-size projectile impact. These experimental techniques have provided significant insights into the deformation mechanisms of graphene sheets and graphene-based nanomaterials. Nevertheless, these experimental techniques suffer from the limited resolution at the nanoscale and are typically destructive, consuming time and material.

A number of theories have been proposed to study and predict the mechanical properties of composites and nanomaterials. In the traditional composites area, micromechanics theories are typically employed to predict the effective behavior of heterogeneous composites. The simplest of these to describe the reinforcement achieved from a high-modulus in a low-modulus matrix is the rule of mixtures [55]. Later theories have aimed to account for the orientation and size of the filler among other effects [62]. There are also semi-empirical methods to describe the reinforcing efficiency by considering more factors, such as Halpin-Tsai model [63], and Mori-Tanaka model [64, 65]. When considering the mechanical properties of polymer-based nanocomposites, some have suggested that classical micromechanical models developed for normal composites cannot be generally applied and that the interactions and interphases at the molecular scale play a major role [66]. Even if they may be somewhat phenomenological at times, there is still overwhelming evidence that micromechanics models and theories can effectively describe the mechanical behavior of nanocomposites [67, 68]. Among these modeling approaches, the classical shear-lag model is particularly noteworthy [69, 70] because it has been successfully applied to study the interfacial shear stress distributions [71-74] and explain the optimal length scales emerging from shear load transfer in biological materials [75, 76].

Another important characterization method for nanomaterials is computation and modeling. Among all the computational techniques, molecular dynamics (MD) simulations have been successfully applied to investigate thermal and mechanical properties of nanoscale materials and systems. In particular, many studies have utilized MD simulations to investigate graphene and its related nanomaterials. One major portion of these studies focus on all-atomistic (AA) simulations, in which every atom in the systems is represented. Another portion focuses on coarse-grained (CG) simulations, where groups of atoms are clustered into beads that interact through an effective force-field. With fewer particles and degrees of freedom, CG simulations are able to investigate mesoscale physical processes, while retaining certain molecular details of the systems. More details about MD simulations and CG technique will be introduced in **Chapter 2**.

1.4 Thesis outline

Despite recent developments in characterization methods, there are still certain aspects of research areas in which experimental methods have limited resolution and AA MD simulations are prohibitively expensive to conduct. For instance, the physical mechanisms governing the mechanical performance of multi-layer graphene system span multiple length scales [7]. Neither experimental techniques nor AA MD simulations can access all the relevant length scales, and there is a huge gap between them in terms of spatio-temporal scales. In addition, there have been long-existing challenges in applying MD simulation results to predict macroscopic materials properties and investigate fracture mechanisms, especially for polymer systems [77, 78].

To bridge the current gap between experimental and computational characterization methods and further empower MD simulations, this work starts with developing multiscale computational approaches, in particular, CG MD models for MLG and GO sheets. The detailed calibration approach and model performance are presented in **Chapter 3**. With 2 to 3 orders of magnitude

computational efficiency increase gained by these CG models, they are utilized to elucidate the mechanisms of deformation and failure of graphene-based nanomaterials, which corroborate recent findings of nanomechanical experiments. Specifically, in **Chapter 4**, I focus on the nanoindentation characterization of MLG and GO sheets and fracture toughness measurements, and, in **Chapter 5**, I focus on dynamic loading conditions, i.e., ballistic impact. These two chapters explicitly show that MD simulations utilizing the developed CG models are able to not only illustrate unique deformation processes, but also reveal failure mechanisms that are not easily obtained from experimental methods. Along the way, I also present analytical models that are developed to generalize these findings and unravel size-dependent properties of different systems.

For the characterization of matrix material – epoxy resin, a robust atomistic model for its crosslinked structure is developed in **Chapter 6** and used to investigate the effect of resin functionality, crosslink degree, and component ratio on resin thermomechanical properties. More importantly, atomistic tensile simulations of the resin are linked with its macroscopic fracture energy, using a theoretical fracture mechanics model developed for polymeric systems. With this theoretical model, it is possible to provide physical insight into the molecular mechanisms that govern the fracture characteristics of epoxy resins. Then, in **Chapter 7**, to establish the structure-property relationship of carbon fiber reinforced epoxy resin composites from a multiscale perspective, MD simulation results and an analytical gradient model are combined to characterize interphase properties, which are integrated into finite element analyses to investigate the failure behavior of composites. In addition, in the same chapter, I also present the work in understanding the failure mechanisms of a nacre-inspired nanocomposites with layered MLG/PMMA structure.

At last, in **Chapter 8**, I summarize the contributions of these studies and indicate possible research directions to conduct in the future. Throughout this dissertation, I especially focus on how

different characterization methods, with MD simulation as a basic tool, have been used to advance the understanding of the mechanics of graphene-based nanomaterials and carbon fiber reinforced epoxy resin composites.

Chapter 2: Computational Method

In this chapter, the basic computational tool – molecular dynamics (MD) simulation will be discussed. The first section provides an overview of MD, as well as some practical considerations that are employed. The second section discusses different force fields, some of which will be used in our simulations. The third section introduces the general coarse-graining methods for different systems as well as common CG models in the literature. While an overview of the techniques is included in this chapter, more specific details can be found in the following chapters.

2.1 Molecular dynamics simulations

MD simulations basically simulate the movement of particles based on Newton's Law of Motion:

$$\vec{F} = \frac{d}{dt}(m\vec{v}) = m\vec{a} \tag{2-1}$$

Thus, two basic elements for conducting MD simulations are the initial positions of the particles, i.e., the atomistic or molecular structure of your system, and the interactions between the particles, i.e., the force field. All-atomistic (AA) systems would exactly follow the atomistic structure of the system, for instance, graphene possesses hexagonal lattice with a side length of 1.4 Å, polymers have repetitive structure of monomers, and metals have distinctive lattices (FCC, BCC etc.) and lattice constants. For the force field, in order to differentiate the interactions between covalent bonded and non-bonded interactions, different function forms and disparate steepness of potential well are adopted. For instance, a stiff harmonic potential is usually used to represent covalent bond for small bond stretching and compressing. In this case, the covalent bond behaves like a stiff spring between a pair of atoms:

$$V_b(d) = K(d - d_0)^2 \tag{2-2}$$

where d_0 is the equilibrium bond length, and K is the spring constant.

However, for scenarios that require bond breaking, Morse potential can be used to represent the behavior of typical bonds, in which a bond is breakable at the maximum point of the bond force. The potential form is written as:

$$V_b(d) = D_0[1 - e^{-\alpha(d-d_0)}]^2 \tag{2-3}$$

where D_0 is the depth of potential well and α relates to the width of the well.

Other covalently bonded interactions include angle, dihedral, and improper interactions, which are used to capture the realistic angle bending, bond torsion, and the out-of-plane bending angles, respectively. Specifically, in Chapter 3, we will show that both bond and angle interactions govern the in-plane tensile and shear modulus of a sheet composed of hexagonal lattice, as in the case graphene, while the dihedral interaction influences the out-of-plane bending stiffness of the sheet. For polymer system, the dihedral and improper interactions are especially important for the chain relaxation dynamics [79].

For non-bonded multi-atom interactions such as van der Waals (vdW) interaction, pair-wise potentials are often used. The pair-wise potentials usually include both attractive and repulsive interactions, and one typical potential form is known as 12-6 Lennard-Jones (LJ) potential:

$$V_{nb}(r) = 4\varepsilon_{LJ}[(\frac{\sigma_{LJ}}{r})^{12} - (\frac{\sigma_{LJ}}{r})^{6}] \tag{2-4}$$

where ε_{LJ} and σ_{LJ} are the two independent parameters governing depth and width of the potential well, respectively.

With the two essential components: structure and force field, one can obtain the forces exerted on each particle, and by integrating Eq. (2-1) in time, the trajectory of the particles (i.e. their

position and velocity) can be traced and many system properties can be extracted including temperature, pressure, energy, etc. For large systems involving millions of particles as common in an MD simulation, efficient numerical integration technique must be implemented in order to obtain the whole trajectory. There are several factors to consider when choosing the specific numerical algorithm to solve Eq. (2-1) numerically, including stability and accuracy of the method as well as programming simplicity and memory requirements. One of the most popular algorithms is the Velocity Verlet Algorithm [80], which is also adopted by software packages such as LAMMPS [81], NAMD [82], and GROMACS [83]. These packages have been developed over 20 years and offer a great amount of flexibility to simulate and analyze systems from different perspectives. For most of our MD simulations, we utilize LAMMPS package as it provides more versatility in performing specific simulation techniques. Typically, time steps are used that are 1/10 the time of the fast period of relevant motion in the system. In fully atomistic simulations, the time step used for time integration is on the order of femtoseconds (10^{-15} seconds). When utilizing CG models in which several atoms are clustered into one single bead, it allows for an increase in time step.

In addition to the numerical algorithms, another practical method to run MD simulations is to use a statistical ensemble that describes the possible microstates of the system [84]. During these ensembles, a separate constraint is applied to the system dictated by the quantities that are held fixed in a simulation. Three ensembles of interest are the microcanonical ensemble (NVE), canonical ensemble (NVT), and isothermal-isobaric ensemble (NPT), where N represents the number of particles, V represents the system volume, T is the system temperature, and P is the pressure of the system. The specific ensembles used in our simulations will be specified in each chapter of the text.

2.2 Typical force fields

Many sets of force fields have been developed and verified for different systems. For instance, OPLS [85], AMBER [86], CHARMM [87], and GROMOS/GROMACS [88] are commonly used force fields for biomolecules. Especially, CHARMM force field has been used by my colleagues to study cellulose nanocrystals [89-91] and protein secondary and tertiary structures [92, 93], and the force field has been integrated into the NAMD software package. In addition, DREIDING [79] is a generic force field for polymeric systems, which has been validated for both PMMA [94] and epoxy resin systems [78, 95]. In Chapter 6, I will apply DREIDING force field to the crosslinked atomistic epoxy resin models and investigate the glass transition temperature of epoxy resins. Embedded-atom method (EAM) [96] force field is particularly appropriate for metallic systems. ReaxFF [97], a reactive force field, is able to simulate continuous bond formation and breaking and could consider possible chemical reactions. It is used to capture the uniaxial tensile failure of epoxy resin including network breaking in Chapter 6.

For graphene, a widely used force field for AA configuration is called adaptive intermolecular reactive empirical bond order (AIREBO) potential [98], in which the interatomic interactions have strong coordination-dependence through a bond order parameter, which adjusts the attraction between two atoms based on the position of other nearby atoms. It has been shown to capture the realistic mechanical behavior of graphene sheets, including in-plane elastic properties [99], temperature and strain rate dependence of fracture strength [100], in-plane shear performance [101], nanoindentation of suspended sheets [102], fracture properties of polycrystalline graphene sheets [20, 25], dynamical failure under projectile impact [103, 104]. All these AA simulations using AIREBO potential have provided significant insights into different deformation mechanisms and mechanical properties, but the system sizes are often limited.

2.3 Coarse-graining methods

Even though AA simulations have shown accurate descriptions of different systems ranging from polymers to graphene regarding their thermomechanical properties, they are prohibitively expensive to study large-deformation or failure mechanisms at mesoscale, i.e., larger than 50 nm in size. In addition, when long simulation time is needed, for instance, equilibration of polymer system with long chains, AA simulations are even more restricted.

As aforementioned, CG models, where groups of atoms are clustered into beads that interact through an effective force field (which needs to be newly designed), offer great promise as they allow simulating much larger systems and much longer physical process, while still retaining the molecular detail of each system. Many CG models have been developed for a wide variety of systems, based on principles such as Boltzmann inversion [105], free-energy calculations [106], and strain-energy conservation [107]. Here, I will briefly discuss current CG models for lipids or proteins, polymers, and graphene.

One of the most popular CG models for lipids or proteins is the MARTINI model [106], which is residue based and uses a mapping scheme of four-to-one, i.e., an average of four heavy atoms are represented by a single interaction bead [106, 108, 109]. Usually, the bead locates at the center of mass of these four atoms. So, for typical protein amino acid structures, the backbone unit is usually represented by one bead while the side chain is represented by one or more beads, depending on its dimensional degrees of freedom [108]. To represent the variety of non-bonded interactions in the lipid or protein structure, first, four types of basic interactions are defined: polar, nonpolar, apolar, and charged. Within these main types, subtypes are also defined to precisely capture the interactions. For instance, hydrogen-bonding capacities are differentiated by four subtypes: donor, accepter, both, and none [106]. The potential forms in the MARTINI model are

similar to those used in CHARMM force field. For instance, harmonic potentials are applied to represent the bonds and angles. A shifted 12-6 LJ potential energy function together with a Coulombic function is used for the vdW interaction and electrostatic interaction, respectively.

The CG models for polymers can be divided into two categories, and one is generic CG models, and the other is systematic CG models. In the former category, the molecular details are ignored, and the force field is identical for different types of polymers. However, because fewer details are considered, larger spatial and temporal scales are easily approached by these generic models [110]. One of the most widely used generic CG models is the finite-extensible non-linear elastic (FENE) model [111-113]. Using this model, insights have been achieved on the effect of molecular weight on the dynamics or rheology of polymer systems [114, 115], and they have also been validated with the prediction from the Rouse [116] or tube [117] model, as well as with experiments [118]. For systematic CG models, they keep many intrinsic chemical and physical features of specific polymers. The potentials developed in the force fields of these CG models have more specific physical meanings, thus they have good transferability and can be systematically modified to represent similar polymer systems. My colleagues (Hsu and Xia) have contributed significantly in developing such models as well as developing thermomechanically consistent coarse-graining (TCCG) technique [94, 119] and temperature transferable coarse-graining technique [120, 121]. By retaining crucial chemical details of specific polymers and capturing diffusion coefficient, glass-transition temperature, and mechanical properties of different polymer systems, these CG model has been applied to study mechanical properties of polymer thin films [122-125] and nanocomposites [39].

There have been some efforts on CG model development of graphene [107]. The basic approach for developing CG models of such systems with specific lattice structure and mechanical

properties is strain energy conservation approach, where the new force field for the CG model is specifically calibrated to capture the strain energy of the materials, which is related to Young's modulus and strength. The CG model developed previously for graphene has suffered a few shortcomings. First, it only considers the linear elastic regime of graphene sheets given that the covalent bond adopts harmonic potential without any bond breaking criteria. Second, due to a high level of coarse-graining mapping (~250 carbon atoms to 1 CG bead), it is challenging to capture many intrinsic properties of graphene sheets, for instance, orientation dependent interlayer shear stiffness [126]. Moreover, this CG model of graphene is not compatible with current CG models of polymer mentioned earlier, thus it cannot be utilized to study graphene-polymer nanocomposite behavior. Starting from next chapter, I will illustrate our strategy to tackle these shortcomings and present our CG model of graphene.

Chapter 3: CG Model Development for Graphene and GO

This chapter focuses the efforts to develop CG models for graphene and GO sheets. The developed models aim to capture the unique mechanical properties of these two systems. The structures of the CG models are inspired by their actual chemical structures. A systematic strain energy conservation approach is adopted in developing these models. Portions of the text and figures within this chapter are reprinted or adapted with permission from Ruiz et al. Carbon 2015 [127] and Meng et al. Carbon 2017 [128].

3.1 CG model of graphene

3.1.1 CG model description

We use a 4-to-1 mapping scheme to conserve the hexagonal lattice of graphene, in which a carbon atom with its nearest three atoms is mapped into one bead in the CG model, as shown in Fig. 3-1(a). We later show that this mapping scheme can capture unique mechanical properties of graphene sheets, such as anisotropic in-plane tensile properties [100] and stacking orientation dependence of interlayer shear [129, 130]. This coarse-graining level is in line with MARTINI model [106] and typical CG models of polymers [94, 119]. The force field of the CG model includes the contributions from bonds, angles, dihedrals and pair-wise non-bonded interactions, which are illustrated in Fig. 3-1(b). The function of each potential is given as:

$$V_b(d) = D_0[1 - e^{-\alpha(d-d_0)}]^2 \tag{3-1}$$

$$V_a(\theta) = k_\theta(\theta - \theta_0)^2 \tag{3-2}$$

$$V_d(\phi) = k_\phi[1 - \cos(2\phi)] \tag{3-3}$$

$$V_{nb}(r) = 4\varepsilon_{LJ}[(\frac{\sigma_{LJ}}{r})^{12} - (\frac{\sigma_{LJ}}{r})^{6}] \tag{3-4}$$

where we use Morse-type potential to represent the bond interaction, and d_0 is the equilibrium bond length, which equals to 2.8 Å, double the length of sp^2 bonds in graphene lattice, D_0 is the depth of potential well of the Morse bond and α relates to the width of the potential well; k_θ is the spring constant of the harmonic angle potential, θ_0 is the equilibrium angle, which equals to 120° based on the hexagonal lattice; k_ϕ is the spring constant of the dihedral interaction, ε_{LJ} and σ_{LJ} are the two independent parameters of the 12-6 LJ potential to represent the interlayer pair-wise interaction. To assure an interlayer equilibrium spacing of $\Delta z_{eq} = 3.35$ Å, we calibrate $\sigma_{LJ} = 3.46$ Å. We note that the pair-wise interaction is only applied between beads in different layers.

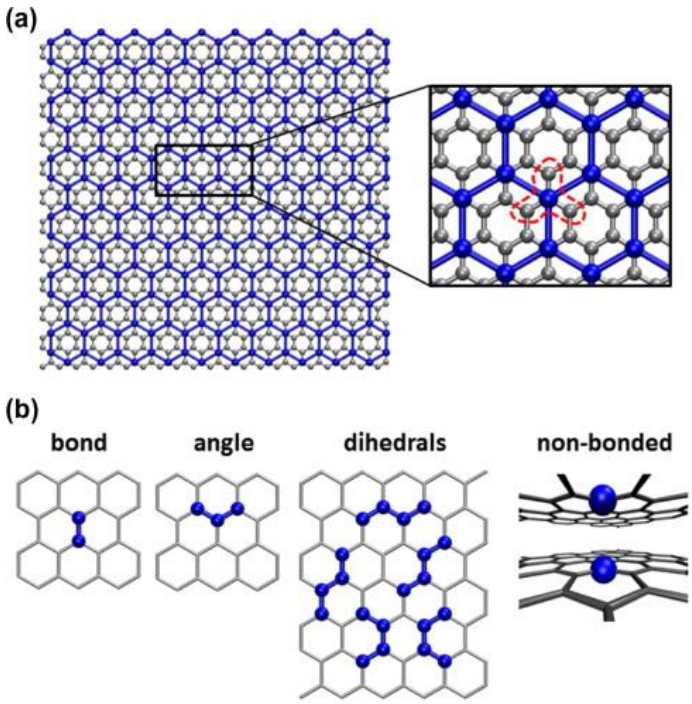

Figure 3-1. Schematics of the coarse-grained model of graphene. (a) CG lattice (blue) overlaid over the atomistic structure (grey). The magnified image shows that each bead in the CG model represents 4 carbon atoms. (b) illustration of the contributions of the CG force field. Different energy contributions are highlighted with ball-stick representation in blue.

To calibrate the 5 parameters in the force field (D_0, α, k_θ, k_ϕ, ε_{LJ}), we adopt the strain energy conservation approach such that the elastic and fracture properties of the model, namely the in-plane Young's modulus (E), the in-plane shear modulus (S), the failure strain of the bond (ε_{max}), the bending rigidity of graphene monolayer (M), and the adhesion energy per surface area (U_a), are consistent with realistic properties obtained experimentally or from atomistic simulations.

From both computational and experimental studies, we know that Young's modulus of graphene is approximately 1 TPa, the failure strain of the bond is set as 25% [4, 131], and we choose $S = 450\ GPa$ as the target value for in-plane shear modulus [101]. The reported values of the bending rigidity of monolayer graphene range from 0.7 to 2.1 eV [107, 132-134]. Here, we use an intermediate value of $M = 1.6\ eV$. A wide range of adhesion energy per surface area is also found in the previous studies [107, 135-137], and we use $U_a = 260\ mJ/m^2$ as our target value.

The bond and angle interactions govern the in-plane properties of the CG model. Gillis has derived the relationship between the elastic constants of graphene and the force constants of the harmonic bonds and angles of the hexagonal lattice, k_b and k_θ respectively [138], where $k_b = \sqrt{3}ES\Delta z_{eq}/(4S - E)$ and $k_\theta = \sqrt{3}d_0^2 ES\Delta z_{eq}/6(3E - 4S)$. Using our target values ($E = 1\ TPa$ and $S = 450\ GPa$), we obtain the values of the spring constants $k_b = 470\ kcal/mol \cdot \text{Å}^2$ and $k_\theta = 409.4\ kcal/mol \cdot rad^2$ by using Δz_{eq} and d_0 values of the model. The spring constant of k_b can be related to the Morse bond as $k_b = D_0\alpha^2$. In addition, the parameter α is directly related to the failure strain of the bond (ε_{max}), $\alpha = log2/(\varepsilon_{max}d_0)$. For $\varepsilon_{max} = 25\%$, we have $\alpha = 0.99\ \text{Å}^{-1}$, then it gives rise to $D_0 = 479.5\ kcal/mol$. The out-of-plane bending response of the model is governed by the dihedral term. By prescribing a bending deformation to the sheet at constant curvature κ and measuring the bending strain energy U_{bend} of the sheet, we can get the

bending rigidity $M = 2U_{bend}/\kappa^2$. By changing the dihedral parameter k_ϕ, we find $k_\phi = 4.15\ kcal/mol$ to preserve the target value $M = 1.6\ eV$. Similarly, we conduct bilayer sheet adhesion energy test and obtain $\varepsilon_{LJ} = 0.82\ kcal/mol$ to match the targeted adhesion energy. A summary of all the functional form and parameters in the force field is presented in Table 3-1.

Table 3-1. Functional forms and calibrated parameters of the force field of MLG CG model.

Interaction	Functional Form	Parameters
Bond	$V_b(d) = D_0[1 - e^{-\alpha(d-d_0)}]^2$ for $d < d_{cut}$	$d_0 = 2.8$ Å $D_0 = 479.5\ kcal/mol$ $\alpha = 0.99$ Å^{-1} $d_{cut} = 3.5$ Å
Angle	$V_a(\theta) = k_\theta(\theta - \theta_0)^2$	$\theta_0 = 120^\circ$ $k_\theta = 409.4\ kcal/mol \cdot rad^2$
Dihedral	$V_d(\phi) = k_\phi[1 - \cos(2\phi)]$	$k_\phi = 4.15\ kcal/mol$
Non-bonded	$V_{nb}(r) = 4\varepsilon_{LJ}[(\frac{\sigma_{LJ}}{r})^{12} - (\frac{\sigma_{LJ}}{r})^6]$ for $r < r_{cut}$	$\sigma_{LJ} = 3.46$ Å $\varepsilon_{LJ} = 0.82\ kcal/mol$ $r_{cut} = 12$ Å

3.1.2 Protocols for the MD simulations

The MD simulation package LAMMPS is used to carry out all the CG MD simulations. We choose a time of 4 fs for all the simulations. The x and y directions correspond to the zigzag and the armchair edges respectively. Next, uniaxial stretching, in-plane shear, and sliding of a graphene flake over a graphene substrate are carried out to evaluate the performance of the model.

To measure the in-plane mechanical response of the model, we use 10-layer square sheets of edge size around 10 nm. Periodic boundary conditions (PBC) are applied in all directions. The system is first minimized and then equilibrated in the NPT ensemble at $T = 300\,K$ and zero pressure for 1 ns. After equilibration, the strain-controlled uniaxial tensile test is performed by deforming the simulation box in either direction at a strain rate of $5 \times 10^8\,s^{-1}$. During the deformation, the pressure is kept zero in all directions except the loading direction.

The in-plane shear simulations are performed on the same multi-layer system as the tensile test but using NVT ensemble. The same shear rate of $5 \times 10^8\,s^{-1}$ is used. We perform two types of simulations depending on the applied constraints. In the first type, the beads of the different sheets are constrained to move just in the sheet plane, and as a result, out-of-plane buckling of the sheets is not allowed. In the second type, no such constraints are applied. The shear stress in both cases is determined from the off-diagonal component of the stress tensor in the direction of shear.

To evaluate the interlayer shear response of the model, we simulate a graphene flake sliding on top of a graphene substrate. The flake dimensions are $87.3 \times 81.2\,\text{Å}^2$ and the substrate $378.3 \times 333.2\,\text{Å}^2$. The graphene substrate is constrained in all directions and the flake is constrained in the in-plane direction perpendicular to the pulling direction. To minimize the thermal noise, the system is equilibrated in the NVT ensemble at $T = 5\,K$ for 200 ps. After equilibration, the flake is pulled using steered molecular dynamics (SMD). During SMD simulations, a spring is attached to the center of mass of the flake and the spring is pulled at a constant velocity of $10^{-6}\,\text{Å}/fs$. We choose a spring constant $k_{SMD} = 470\,kcal/mol \cdot \text{Å}^2$. We measure the force vs. displacement response during SMD pulling. In addition, we have confirmed that the interlayer shear landscape is independent of the flake size as long as the spring constant of the SMD is adjusted accordingly.

3.1.3 Performance of the CG model

The anisotropy or chiral dependence of the in-plane mechanical properties of the model is shown in Fig. 3-2 (a). We note that this dependence arises naturally from the honeycomb lattice configuration, a distinctive feature of our CG strategy. The non-linear softening response is due to the anharmonic Morse potential in large deformation. We can also capture the failure behavior of the graphene sheets, marked by the drop in the stress-strain curves. This is another distinctive feature of our CG model that it enables bond breaking, which lead to the failure of graphene sheets. For small deformations, the zigzag and armchair directions behave similarly, and we obtain identical Young's modulus in either direction by fitting the slope of the stress-strain curve in small deformation, which is around 960 GPa. This value is very close to the experimental measure value [4]. The nominal failure strength of our model in the zigzag direction is 121 GPa, while 97 GPa in the armchair direction, which is also consistent with the experimental value of approximately 120 GPa [4].

The in-plane shear response along the zigzag direction is shown in Fig. 3-2(b). If the motion of the beads is confined to the plane of the corresponding layer, the response is linear elastic with a shear modulus in the zigzag direction very close to the target value used for the calibration of the model, $S_{cons}^{zig} = 445\ GPa$. If constraints are not applied, the system reaches an instability point where the sheets buckle at a very small shear strain of 0.5%. The response is non-linear after the instability, and the critical in-plane shear strain is $\gamma_{max}^{zig} = 21\%$ and the shear strength is $\tau_{max}^{zig} = 44.6\ GPa$. These values are in reasonable agreement with these reported by Min and Aluru using atomistic simulations and the AIREBO force field [101]. The reduction in strength in the unconstrained case compared to the constrained case is also in good agreement.

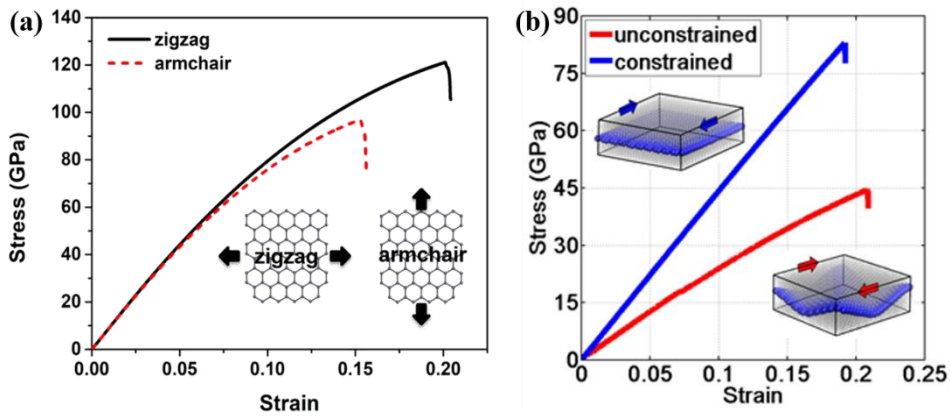

Figure 3-2. In-plane mechanical behavior of the CG model. (a) Uniaxial tensile test in both zigzag (black) and armchair (red) directions. (b) Comparison of in-plane shear testing along the zigzag direction between the case when the sheets are not allowed to buckle and the case when no constraints are applied.

The interlayer shear response governs the mechanical property of large-scale MLG assemblies, such as reinforcements in nanocomposites [139] or graphene papers [74, 140]. To evaluate the shear response of the model, we define the interlayer shear strain as $\varepsilon_s = \Delta d/t$, where Δd is the displacement in the pulling direction, and t equals the interlayer equilibrium distance Δz_{eq}, and the shear stress as $\tau_s = f/A_{flake}$, where f is the pulling force and A_{flake} is the area of the graphene flake. The shear stress-strain curve shows a periodic response. We define the interlayer shear modulus as the maximum slope in one period of the response. We find that the shear modulus is strongly flake orientation dependence, with the shear modulus measured for orientation angles $\theta = 0^{\circ}$ and $\theta = 60^{\circ}$ (commensurate stacking) 2 and 3 orders of magnitude larger than the other orientation angles (non-commensurate stacking), as shown in Fig. 3-3(b). This existence of low friction for non-commensurate stacking orientations is known as superlubricity, which has been observed experimentally [126, 130]. In addition, the measured shear modulus in commensurate stacking lies in the range of experimental measured values.

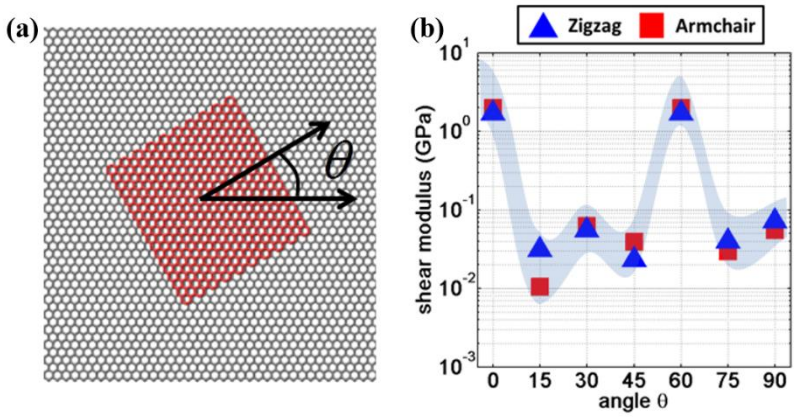

Figure 3-3. Interlayer shear response of the CG model. (a) Schematic of the simulation set up. A graphene flake sits on top of a graphene substrate at an angle θ. (b) Interlayer shear modulus as a function of orientation θ.

In sum for the CG model of graphene, we use a strain energy conservation approach for calibration, where the force field parameters are calibrated using well-known elastic mechanical properties of graphene. Despite the simplicity of the force field, we show that the model can quantitatively capture complex mechanical properties and behaviors such as non-linear elasticity, anisotropy in the zigzag and armchair directions, and buckling of the sheets under shear deformation. Moreover, the model naturally captures the complex interlayer shear response of graphene, such as superlubricity. Additionally, the model is compatible with other existing models of proteins and polymers, which makes it very appealing for the use in the modeling of graphene-based nanocomposite.

3.2 CG model of GO

3.2.1 CG model description

Most prior investigations on GO modeling were carried out using AA simulations or first principle calculations, which provide valuable insights into molecular mechanisms and unique

mechanical properties of GO sheets. Specifically, it has been shown that the in-plane mechanical properties, i.e. Young's modulus and intrinsic strength, monotonically decrease with increasing degree of oxidation [141, 142]. Soler-Crespo and coworkers have found that the composition of GO also affects the mechanical behavior of GO, and epoxide-oxidized GO sheets have relatively larger failure strain than hydroxyl-oxidized GO [143]. Nevertheless, there are still many drawbacks in these detailed computational approaches. The most critical one is that the simulated GO systems are limited to the sizes lower than 10 nm, thus limited our understanding the mechanical behavior of GO sheets at larger scales. However, typical coarse-graining methods are not applicable to the highly heterogeneous GO systems. For instance, MARTINI-type method requires a determined chemical structure of the system, while GO sheets differ from each other with different composition and distribution of functional groups. In addition, the chemical structures influence the properties of GO system significantly, and it is impossible to utilize strain energy conservation approach exhaustively for every targeted property of specific structures. These issues require a highly versatile coarse-graining method that could consider different chemical structures of GO and their distinctive influences on mechanical properties and achieve greater computational efficiency as well.

Our proposed CG model of GO still conserves a similar hexagonal lattice structure, since the basic planar structure of GO is similar to graphene and in this way, we could also take advantage of our previous work on CG model of graphene. But different from the CG model of graphene, the CG model of GO also includes two other different types of beads, representing hydroxyl- and epoxide-oxidized functional regions as illustrated in Fig. 3-4. By directly varying the percentages of each type of beads in the CG model, we are able to generate CG structures of GO with different degrees of oxidation and compositions. To capture the diversity of mechanical properties of GO

arising from different structures, we also differentiate the bonded and non-bonded interactions for these types of beads. However, to maximize the computational efficiency, we only include bond, angle and non-bonded interactions, and bonds and angles are for intralayer interactions while non-bonded interactions are for interlayer ones. In addition, we categorize the bonds and angles into three types, and the categorizations are listed in Fig. 3-4.

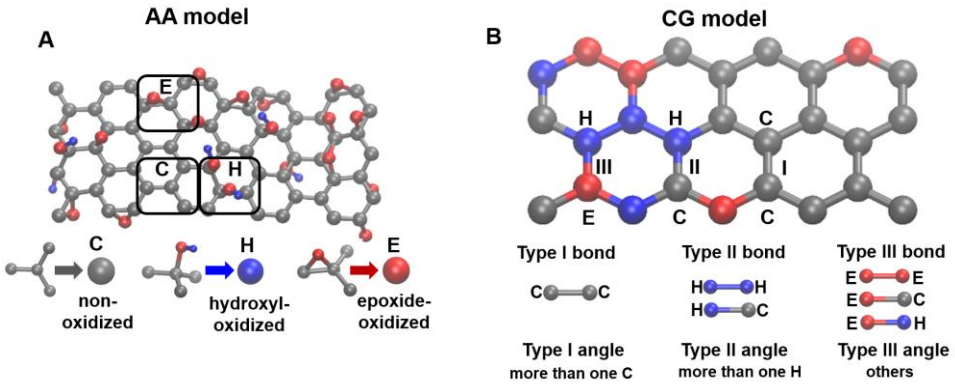

Figure 3-4. Schematic illustration of CG model of GO. Panel A shows the all-atomistic (AA) GO structure and the AA to CG mapping scheme, where three types of CG beads: non-oxidized (C), hydroxyl-oxidized (H) and epoxide-oxidized (E), represent different AA lattices. Panel B shows the resulting CG structure with different types of CG beads and the classification of bond and angle types.

In our CG model, the percentage of bonds and angles can be simply changed by prescribing the percentage of different beads. The functional form of bond type I ($V_{b,I}$) is the same as that in the CG model of pristine graphene, which is represented by Morse potential. For bond types II and III ($V_{b,II}$ and $V_{b,III}$), we choose a piecewise harmonic functional form in order to capture the unique non-linear behavior of GO of either hydroxyl-oxidation or epoxide-oxidation. To represent the distorted hexagonal structure by functional groups, we use different equilibrium bond lengths (d_0) for the three types of bonds herein, which are double the equilibrium C-C bond length in pristine

graphene, with a hydroxyl group connected, and with an epoxide group connected, respectively, calibrated using density functional-based tight binding (DFTB) method. Fig. 3-5 shows the typical energy and force profiles for this piecewise harmonic bond potential and a corresponding stress-strain curve of GO sheets by adopting this bond potential. The initial harmonic part in the potential gives rise to linear elastic properties. The change of the slope in the force profile at d_{c1} results in a non-linear behavior in the stress-strain curve. The bond failure strain is controlled by the critical bond length where the maximum force is achieved (i.e. the bond length d_{c2}). We adopt a harmonic functional for all the angle interactions (V_a) and the equilibrium angle (θ_0) is maintained at 120°. We adopt the 12-6 LJ potential for the non-bonded interactions (V_{nb}). The detailed function forms are listed in Table 3-2.

The three sets of parameters are calibrated respectively according to three sets of target properties obtained from DFTB calculation. Specifically, we calibrate the parameters of type I bonds and angles and pair-wise interactions between C beads according to the properties of pristine graphene, and Type II and H beads parameters according to the properties of maximum hydroxyl-oxidation GO sheets, Type III and E beads parameters according to the properties of maximum epoxide-oxidation GO sheets, respectively. Later we show that it is sufficient to capture the dependence of in-plane properties and interlayer adhesion energy of GO sheets on composition and degree of oxidation when combining these three sets of interactions. The detailed calibration process will be discussed shortly.

Table 3-2. Functional forms and calibrated parameters of the force field in the CG model of GO

Interaction	Functional form	Parameters
Bond	Type I: $V_{b,I}(d) = D_0[1 - e^{-\alpha(d-d_0)}]^2$ $d_0 = 2.86\text{Å}$	$D_0 = 443.07\frac{\text{kcal}}{\text{mol}}$ $\alpha = 1.154$ $d_{\text{cut}} = 3.7\text{Å}$
	Type II & III: $V_{b,II\,\&\,III}(d) =$ $\begin{cases} k_{be}(d-d_0)^2 & d < d_{c1} \\ k_{bp}(d-d_{c1})^2 + 2k_{be}(d_{c1}-d_0)(d-d_{c1}) + C_1 & d_{c1} < d < d_{c2} \\ k_{bf}(d-d_{c2})^2 + \left[2k_{bp}(d_{c2}-d_{c1}) + 2k_{be}(d_{c1}-d_0)\right](d-d_{c2}) + C_2 & d_{c2} < d \end{cases}$ $C_1 = k_{be}(d_{c1}-d_0)^2$ $C_2 = k_{bp}(d_{c2}-d_{c1})^2 + 2k_{be}(d_{c1}-d_0)(d_{c2}-d_{c1}) + C_1$	Type II: $d_0 = 2.94\text{Å}$ $d_{c1} = 3.12\text{Å}$ $d_{c2} = 3.46\text{Å}$ $d_{\text{cut}} = 3.5\text{Å}$ $k_{be} = 317.34\ \frac{kcal}{mol\text{Å}^2}$ $k_{bp} = 126.94\ \frac{kcal}{mol\text{Å}^2}$ $k_{bf} = 634.68\ \frac{kcal}{mol\text{Å}^2}$
		Type III: $d_0 = 2.80\text{Å}$ $d_{c1} = 3.00\text{Å}$ $d_{c2} = 4.20\text{Å}$ $d_{\text{cut}} = 4.3\text{Å}$ $k_{be} = 256.1\ \frac{kcal}{mol\text{Å}^2}$ $k_{bp} = 21.34\ \frac{kcal}{mol\text{Å}^2}$ $k_{bf} = 512.2\ \frac{kcal}{mol\text{Å}^2}$
Angle	$V_a(\theta) = k_\theta[\theta - \theta_0]^2$ $\theta_0 = 120^\circ$	Type I: $k_\theta = 456.61\frac{kcal}{mol}$
		Type II: $k_\theta = 259.47\frac{kcal}{mol}$
		Type III: $k_\theta = 189.93\frac{kcal}{mol}$
Non-bonded	$V_{nb}(r) = 4\varepsilon_{LJ}[\left(\frac{\sigma_{LJ}}{r}\right)^{12} - \left(\frac{\sigma_{LJ}}{r}\right)^{6}]$ $\sigma_{LJ} = 7.48\text{Å}$	Type C: $\varepsilon_{LJ} = 0.0255\frac{kcal}{mol}$
		Type H: $\varepsilon_{LJ} = 0.128\frac{kcal}{mol}$
		Type E: $\varepsilon_{LJ} = 0.0797\frac{kcal}{mol}$

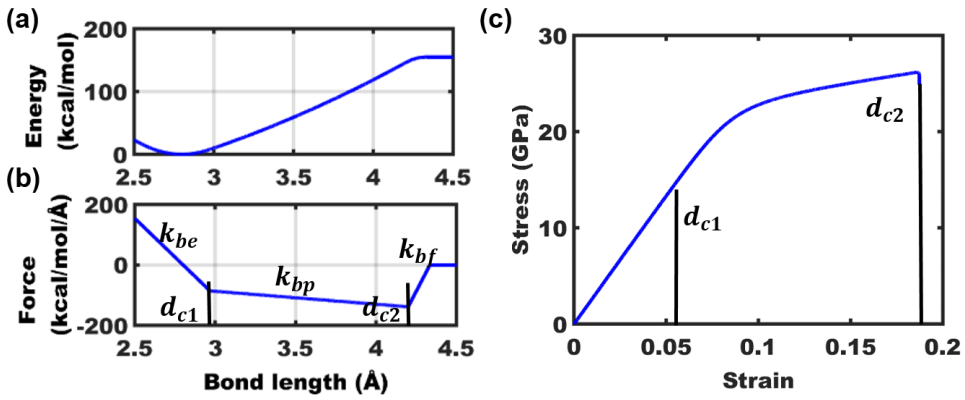

Figure 3-5. Piecewise bond potential used in the CG model. Typical energy (a) and force (b) profiles for type II and III bond potentials. (c) Representative stress-strain curve of a GO sheet with 60% degree of epoxide oxidation using the bond potential shown in (a) (b).

3.2.2 Target GO mechanical property characterization using DFTB

In this part, we collaborate with Dr. Soler-Crespo to carry out a series of semi-empirical DFTB calculations using the open-source code CP2K (http://www.cp2k.org/) to determine the mechanical properties of GO as a function of its chemical compositions. A Monte Carlo-based algorithm is employed to determine the favorable locations for functional groups from random choices according to Boltzmann-like distributions, as discussed in previous work [143-145]. Through the calculations, we first determine the elastic modulus, failure strain under uniaxial tension and interlayer adhesion energy of three targeted GO sheets: non-oxidized, maximum hydroxyl-rich oxidation, and maximum epoxide-rich oxidation. We note that 72% hydroxyl-rich oxidation and 80% epoxide-rich oxidation are the maximum oxidation degrees for each functionalization type. Further increasing the functional group coverage would result in chemical instability of the systems during DFTB calculations. Additionally, GO sheets with a fixed degree of oxidation (70%) but variable chemical compositions (different hydroxyl/epoxide ratio) are generated, and their properties are also obtained for validation purpose.

First, we determine the in-plane properties of the three targeted GO sheets. The all-atomistic GO monolayer sheets have in-plane dimensions of 20×20 Å^2. We apply uniaxial tension on the armchair direction until failure. Stress-strain curves are determined by assuming the effective monolayer thickness as $\Delta z_{eq} = 7.5$ Å for all the sheets. The Young's moduli (E) are obtained by fitting the slope of the linear section in the stress-strain curves. The in-plane shear moduli (S) are calculated by using the linear-elastic relationship $S = E/2(1+v)$, assuming the Poisson's ratio v is a constant equal to 0.16 for all GO sheets, which is taken as the average value for all the degree of oxidation cases according to DFTB calculation results.

To characterize the interlayer adhesion energy, we generate bilayer GO sheets for the three scenarios: non-oxidized, 72% hydroxy-rich, and 80% epoxide-rich. The UFF force field is included to account for the dispersion effects in the material, as implemented in CP2K. The adhesion energy can be determined by calculating the total energy of the bilayer system after optimization and subtracting the energy of two separate single sheets.

A summary of the target properties is shown in Table 3-3.

Table 3-3. Target Properties for GO

	Young's modulus ($\boldsymbol{E}$) GPa	In-plane shear modulus ($\boldsymbol{S}$) GPa	Elastic strain ($\boldsymbol{\varepsilon_{ela}}$)	Failure strain ($\boldsymbol{\varepsilon_{max}}$)	Adhesion energy $\mathbf{mJ/m^2}$
Graphene	530	228	-	21%	31
Hydroxyl-oxidized GO	285	121	8%	10%	156
Epoxide-oxidized GO	230	99	8%	25%	97

* The elastic modulus is calculated by assuming the effective thickness of the monolayer GO as 7.5 Å [143].

3.2.3 Derivation of CG model force field parameters

Next, we derive the parameters of the three sets of interactions (including bond, angle and non-bonded interaction) according to the target properties (Table 3-3) by employing the strain energy conservation approach.

Since type I bonds and angles are similar to the ones used in CG model of pristine graphene, we utilize the same method as in 3.1.1 to derive the parameters in the Morse bond potential and harmonic angle potential. The k_{be} parameter in type II and III bonds as well as k_{θ} of type II and III angles are also similarly derived according to the relationship proposed by Gillis [138]. We find that the parameter d_{c1} in bond types II and III linearly scales with the linear elastic limit strain ε_{ela}. We conduct uniaxial tensile simulations using the CG model with different values of $d_{c1}$and pick the value that conserves ε_{ela} of DFTB results. The slope of the second linear part is related to the nonlinearity in the stress-strain curve before failure, Fig. 3-5. The average slope of the post-elastic region observed from DFTB calculations is conserved by choosing a corresponding k_{bp} value. The d_{c2} parameter is directly related to failure strain and is calibrated to match the failure strain from DFTB calculations. Our CG results also suggest that the slope parameter k_{bf} does not affect the failure strain and stress-strain curve, and thus we specify $k_{bf} = -2k_{be}$. During simulations, we delete bonds once they are stretched to d_{cut}, which is slightly larger than d_{c2}. Thus, all the parameters of the bond and angle potential can be determined.

For the non-bonded interaction parameters, we follow the same method adopted in CG model of pristine graphene that calculates the parameter σ_{LJ} according to the interlayer spacing while tunes the parameter ε_{LJ} based on adhesion energy. As a result, we use $\sigma_{LJ} = 7.48$ Å for all the bead types, and the calibrated ε_{LJ} values are listed in Table 3-2. An identical cutoff value of 20 Å is

adopted for all the pairwise interactions. The pair coefficient for interactions between different types of beads is obtained via a Lorentz-Berthelot mixing rule: $\sigma_{AB} = (\sigma_{AA} + \sigma_{BB})/2$, $\varepsilon_{AB} = \sqrt{\varepsilon_{AA}\varepsilon_{BB}}$. A summary of all the CG force field functional forms and the corresponding calibrated parameters is presented in Table 3-2.

3.2.4 Protocols for the CG MD simulations

LAMMPS is used to conduct all the CG-MD simulations. We choose the same time step of 4 fs as that used in the CG model of graphene. To simulate the in-plane uniaxial tensile test, we use a monolayer sheet of dimensions ~ $50 \times 50\ nm^2$. The system contains ~ 24,000 beads in total and PBC are applied in all the directions, while a 10 nm empty space exists on either side of the sheet in the out-of-plane direction to keep consistent with DFTB calculations. This appropriate model size is determined by running different model sizes until convergence is achieved in the stress-strain results. We find that for smaller systems, the failure strain and maximum are relatively higher, and this size effect might arise from the specific classification of bonds and angles in the CG model. The systems are first minimized and equilibrated in NPT ensemble at $T = 300\ K$ and zero pressure in the in-plane directions. After equilibration, the strain-controlled uniaxial tensile test is performed by deforming the simulation box at a constant rate of $1 \times 10^8\ s^{-1}$ in the armchair direction. During deformation, we constrain the out-of-plane displacements of all the beads in order to maintain the uniaxial tensile condition and minimize the entropic elastic behavior [20].

The bilayer adhesion simulations involve two GO sheets parallel to each other with dimensions ~ $20 \times 20\ nm^2$. PBC are applied om the in-plane directions, and again there is a 10 nm empty space on either side of the sheets in the out-of-plane direction. We also test different sizes of systems ranging from $8 \times 8\ nm^2$ to $40 \times 40\ nm^2$, and the variation of the adhesion energy calculated in within 5%. After initial minimization, the system is equilibrated in the NVT ensemble

at temperature $T = 300\ K$. After equilibration, the energy of interlayer pair-wise interactions is measured. The adhesion energy at 10 K is also calculated, and it is found to be less than 5% higher than the adhesion energy at room temperature, thus verifying that the entropic effect on the adhesion energy is negligible.

3.2.5 Performance of CG model

Having derived all the force field parameters for the CG model based on the three target properties, we validate the CG model by testing it for different degrees of oxidation and compositions. First, in Fig. 3-6 and Fig. 3-7, we compare CG and DFTB uniaxial tensile results in the armchair direction for GO sheets with different degrees of oxidation of either hydroxyl oxidized or epoxide oxidized. We can see that the brittle failure of the hydroxyl oxidation case is captured by using the piecewise potential form of bond type II. The epoxide oxidation cases exhibit a relative larger failure strain and ductility with bond type III. The model also reproduces the general increase of failure strain with increasing epoxide coverage. There is an excellent qualitative agreement between CG model and DFTB calculation.

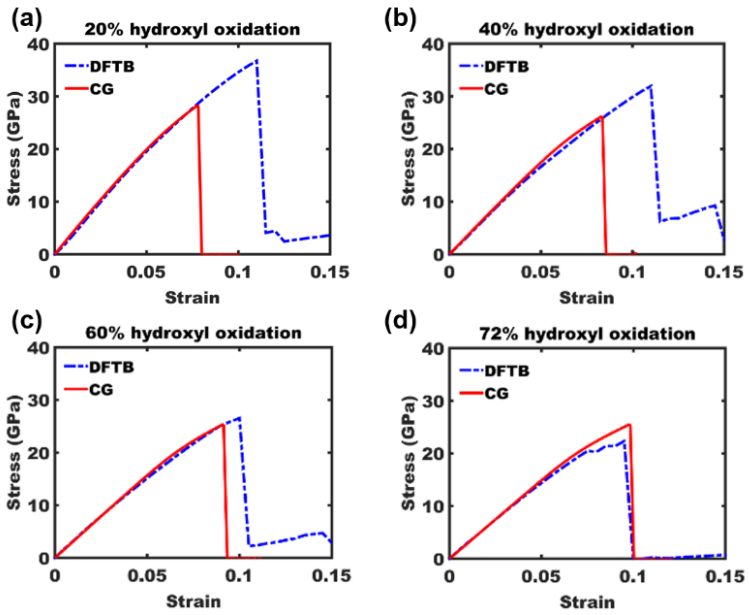

Figure 3-6. Comparison of uniaxial tensile test results from CG model and DFTB calculations for hydroxyl oxidation cases.

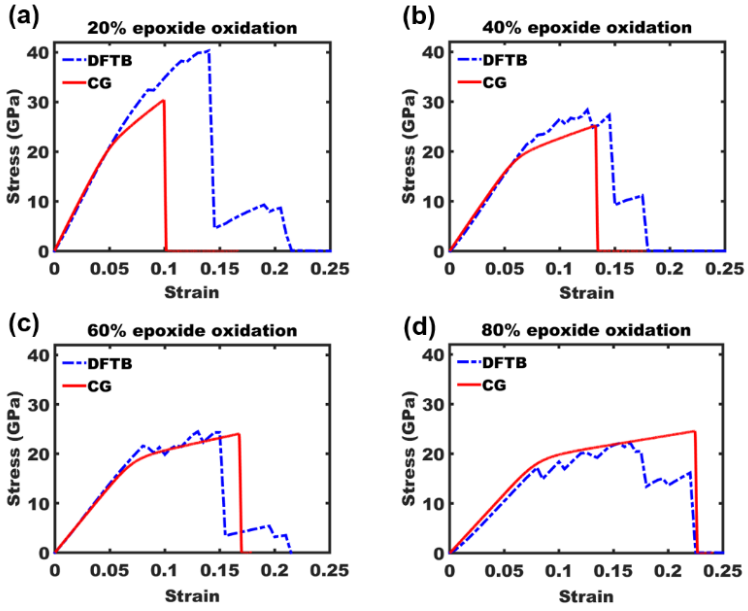

Figure 3-7. Comparison of uniaxial tensile test results from CG model and DFTB calculations for epoxide oxidation cases.

In Fig. 3-8, we compare the elastic moduli and strengths for both oxidation cases obtained from CG model and DFTB calculations. The Young's modulus for each case is within 10% difference. It is a remarkable accomplishment of the model that parameterization for the maximum oxidation case is sufficient to capture the uniaxial tensile behaviors of other degrees of oxidation cases with reasonable accuracy. The strength deviations are typically larger, but the general decreasing trend with increasing degree of oxidation is well preserved.

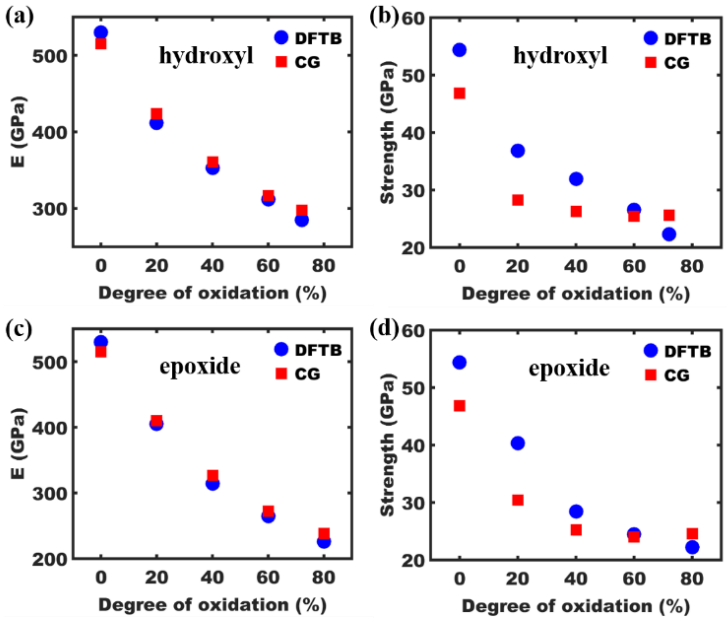

Figure 3-8. Comparison of Young's modulus and tensile strength at different degrees of oxidation between CG model and DFTB calculations.

Having verified the CG model for both hydroxyl and epoxide oxidation cases, we then test the CG model for a wider set of compositions that include combinations of epoxide and hydroxyl functionalization. First, we define the ratio of epoxide and hydroxyl functional groups as $\delta = \frac{N_{epoxides}}{N_{epoxides}+N_{hydroxyls}}$, where $N_{epoxides}$ and $N_{hydroxyls}$ are the total number of epoxide and hydroxyl groups in DFTB calculations, while they represent the total number of type E and type H beads in

CG model. DFTB calculations have indicated that for a given degree of oxidation (70% in this case), brittle to ductile failure behavior can be observed by increasing δ [143]. As shown in Fig. 3-9, the CG model is able to quantitatively reproduce the increasing failure strain trend with increasing δ for combined functionalization cases. Fig. 3-9 (c) also compares the ductility, which is defined as the difference between linear elastic limit strain ε_{ela} and failure strain ε_{max}, between DFTB results and our CG model. The agreement is remarkable. These results demonstrate the predictive capabilities of our CG model given that the model is only calibrated based on three target cases.

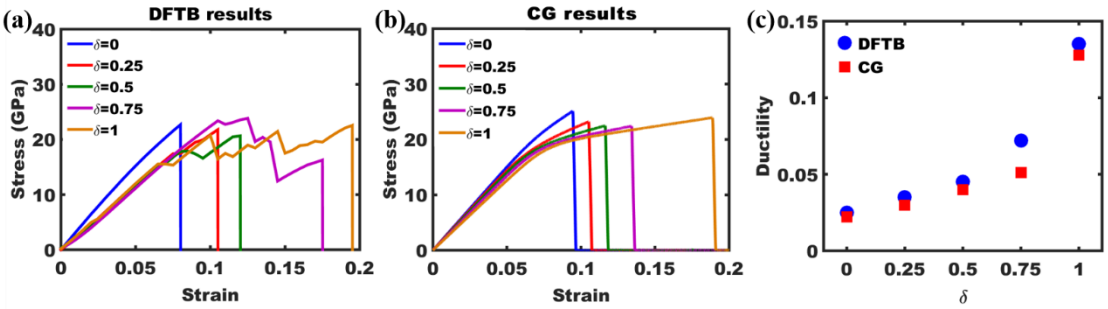

Figure 3-9. In-plane mechanical behavior of combined functionalization cases. (a) DFTB results for different δ at 70% degree of oxidation, and δ is defined as the ratio between the number of epoxide groups and the total number of oxidation groups. (b) CG model results for different δ at 70% degree of oxidation, and δ is defined as the ratio between the number of type E beads and the total number of type E and type H beads. (c) Ductility vs. δ for both DFTB (circle) and CG (square) results.

For the interlayer interaction performance, Fig. 3-10 shows the interlayer adhesion energy for three functionalization cases predicted from the CG model: hydroxyl oxidization, epoxide oxidization, and a combined composition with 1:1 ratio between hydroxyl and epoxide beads. By differentiating the interactions for the three types of beads, our CG model can quantitatively match

the relationship between adhesion energy and degree of oxidation, and also capture the interlayer adhesion difference resulted from different functionalization. We also carry out DFTB calculations on four atomistic cases of combined compositions. The DFTB results all lie near the CG predictions as shown in Fig. 3-10, and this consistency further shows the predictive capability of the CG model for the interlayer adhesion energy.

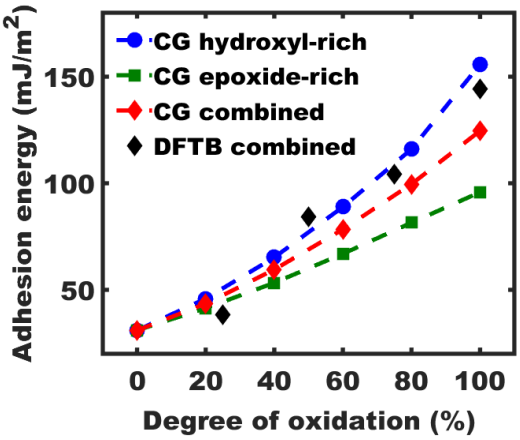

Figure 3-10. Adhesion energy comparison between CG model and DFTB calculations.

In summary, the developed CG model of GO is capable of reproducing the deteriorating mechanical properties of GO with increasing degree of oxidation (functional group density) while improving the interfacial adhesion energy. Compared to DFTB calculations, the model achieves at least ~8000-fold increase in computational speed. With this significant computational efficiency gain, the model would enable us to study the large-deformation and failure mechanisms of mesoscale structures, which are going to be presented in the following chapters.

3.3 Conclusion

This chapter presents the systematic methodology for developing CG models of both graphene and GO and the performance of these models in capturing the mechanical responses of MLG sheets

and GO sheets. Specifically, hexagonal lattice structure is adopted in both models. Then, a strain energy conservation approach is adopted to calibrate the force field parameters according to the basic mechanical properties informed from nanomechanical experiments or higher-level simulations such as DFTB calculations. The CG model of graphene is able to quantitatively reproduce MLG's mechanical response in both elastic and fracture regimes, as well as the orientation-dependent interlayer shear properties. The CG model of GO, by adopting the heterogeneous structure, captures the heterogeneous properties of GO which depend on compositions, such as the deteriorating mechanical properties of GO with increasing degree of oxidation (functional group density) while improving the interfacial adhesion energy. With two to three orders of magnitude increase in computation efficiency, these models help to elucidate the mechanisms of deformation and failure in mesoscale multilayer assemblies. With these models, the mechanical properties of nanocomposites systems will be studied in the following chapters with great computational efficiency.

Chapter 4: Application of CG Model in Quasi-Static Loading Cases

Investigating the mechanical properties and deformation mechanisms of graphene and GO sheets in their multilayer assembly form is especially important, as these multilayer assemblies are to be directly used in nanocomposites as reinforcements. Although direct measurement of Young's modulus and strength has been conducted on free-standing monolayer graphene by using nanoindentation in an AFM, there are still many unsolved physical mechanisms in the multilayer form due to the limited resolution of current experimental technique at the nanoscale. For instance, a nonlinear behavior in the force vs. deflection curves for multilayer graphene (MLG) is observed during nanoindentation, as a repeatable hysteresis always exists during loading/unloading cycles. Moreover, there is strong thickness-dependent strength measured experimentally. The mechanisms cannot be explained by experimental characterization alone. Here, the developed CG model of MLG is utilized to investigate the deformation mechanisms during nanoindentation on MLG films. Furthermore, when applying nanoindentation tests on GO membranes, different force vs. deflection curves were observed. The difference has been attributed to the influence of chemical structures on the mechanical properties, but no direct evidence has been found. Here, using the CG model of GO, the simulation results explicitly illustrate the different nanoindentation behaviors of GO sheets with different compositions, which corroborate the experimental findings. Additionally, the fracture toughness of graphene or GO membranes has been measured experimentally recently but show large scatter. In this chapter, I will show that the CG models have great advantages in estimating fracture toughness and investigating size-dependence of fracture properties as well. Portions of the text and figures within this chapter are reprinted or adapted with permission from Wei & Meng et al. ACS Nano 2016 [146] and Meng et al. Carbon 2017 [128].

4.1 Recoverable slippage mechanisms in multilayer graphene under nanoindentation

During nanoindentation of MLG samples, a closed hysteresis loop during a loading/unloading cycle is observed in the experiments. This hysteresis loop is repeatable in different cycles, as shown in Fig. 4-1, which indicates repeatable energy dissipation. To find out the deformation mechanism corresponding to this hysteresis loop, we adopt the CG model of MLG to conduct nanoindentation simulations at scales comparable to experiments.

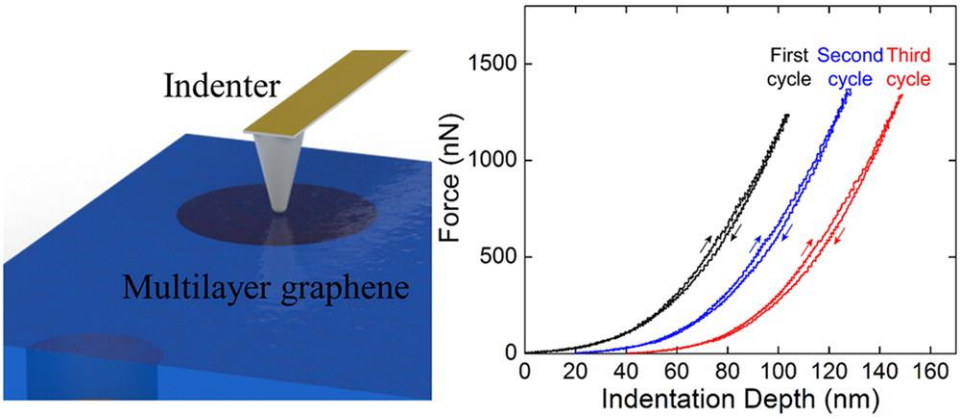

Figure 4-1. Experimental observation of hysteresis during loading and unloading cycles. (a) Illustration of the AFM experimental setup. (b) Three-cycle tests on bilayer graphene sheets to show the repeated energy dissipation.

4.1.1 Simulation setup and elastic properties of MLG

We begin by summarizing experimentally observed linear elastic properties of single and multilayer graphene samples. In the experiments, a diamond probe with a semispherical tip is used to load freestanding circular films at the center using an AFM (XE-100, Park Systems). Typical force vs. deflection curves for monolayer, bilayer and trilayer graphene at small deflections (less than 30% of the deflection required to rupture the specimen) are obtained. We note that in the

small deflection range, no hysteresis is observed during loading and unloading cycles. To obtain Young's modulus, the force vs. deflection behavior can be expressed as [4]:

$$F = \sigma_0 \pi t \delta + \frac{Et}{q^3 a^2} \delta^3 \quad (4\text{-}1)$$

where F is the applied force, δ is the central deflection or indentation depth, a is the film radius, $q = 1.02$ is a dimensionless constant, $t = n\Delta z_{eq}$ is the thickness of the graphene sheets, and $\Delta z_{eq} = 0.34\ nm$ is the equivalent graphene monolayer thickness and n is the number of layers.

The measured monolayer graphene elastic modulus is $1.06 \pm 0.08\ TPa$, and the elastic moduli of bilthe ayer and trilayer graphene sheets are $1.04 \pm 0.04\ TPa$ and $0.98 \pm 0.06\ TPa$, respectively. Within experimental error, the elastic moduli for graphene flakes up to three layers are identical and do not exhibit size-dependence.

Using the CG model developed previously, we carry out nanoindentation simulations on graphene sheets up to 5 layers. Multilayer graphene sheets have an in-plane area of $100 \times 100\ nm^2$. The square sheets are suspended over a circular hole at the center, with a diameter of 50 nm. The fact that the sheet size is much larger than the suspended region makes it possible to mimic the boundary conditions in the experiments. Specifically, the area outside of the suspended region in the bottom layer are fixed by a stiff harmonic spring with spring constant 10,000 $kcal/mol \cdot Å^3$. The other layers are laid on the bottom layer and held in place only by non-bonded interactions. In MLG, two stacking configurations are considered: commensurate stacking and non-commensurate stacking. The commensurate stacking configuration chosen in this study is similar to the Bernal stacking [147], corresponding to the minimum energy configuration of the sheets with no rotational stacking fault. The non-commensurate stacking configuration chosen herein is obtained by having a 90° offset angle between adjacent layers. This non-commensurate stacking configuration, being a higher energy state and having a lower interlayer shear stiffness, is

stable for the sizes of the sheets studied here, as spontaneous rotation is not a kinetically accessible pathway for large sheet overlaps.

The MLG sheets are first relaxed using energy minimization with the conjugate gradient algorithm and further relaxed in the NVT ensemble at temperature $T = 10\ K$ for 200 ps to reduce thermal noise. After the equilibration process, the center of the MLG sheets are indented by a spherical indenter with radius of 4 nm at a constant rate using the command '*fix indent*' in the LAMMPS package. The indenter interacts with CG graphene beads via a repulsive harmonic force, $F(r) = k_{in}(r - R)^2$, where k_{in} is a force constant set to be 1000 $kcal/mol \cdot Å^3$ that can be treated as a rigid indenter, r is the distance between the center of the indenter and beads, and R is the radius of the indenter. Through the process, the forces on the indenter and the corresponding indentation depths are gathered for analysis.

The indentation simulation results of MLG for the commensurate stacking configuration are shown in Fig. 4-2, with the force normalized by the number of layers (i.e. F/n). The normalized forces are superposed with each other at small deflections. The elastic moduli extracted by using deflection smaller than 2.5 nm are found to be approximately $1.02 \pm 0.06\ TPa$ for all the cases. Simulations are also performed on MLG with the non-commensurate stacking configuration, and the results indicate that the elastic modulus is insensitive to the stacking configuration. At larger deformation, however, the curves deviate from the linear elastic model, and the deviation increases with increasing number of layers. We attribute this to the nonlinear elastic response of graphene sheets as well as the greater inhomogeneity in the strain distribution among layers.

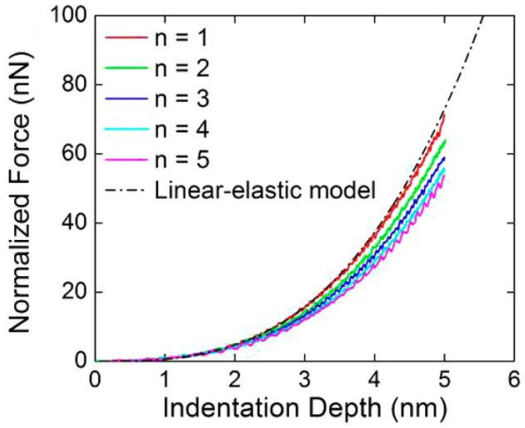

Figure 4-2. Simulation results of indentation force vs. deflection for multilayer systems. The forces are normalized by *n* and all the curves are plotted up to the same indentation depth (~ 60% of maximum indentation depth).

4.1.2 Reversible interlayer slippage mechanism

Fig. 4-3 shows more details of the hysteresis loop during loading/unloading cycles in experiments for both bilayer and trilayer sheets. At deflection of approximately 80 nm, kinks in the experimental force vs. deflection curves can be seen in both cases. The unloading segments do not follow the kink, thus creating the hysteresis. Interestingly, the unloading segments coincide with the loading segment when the film deflection is below 50 nm, suggesting the system goes back to its original energy state.

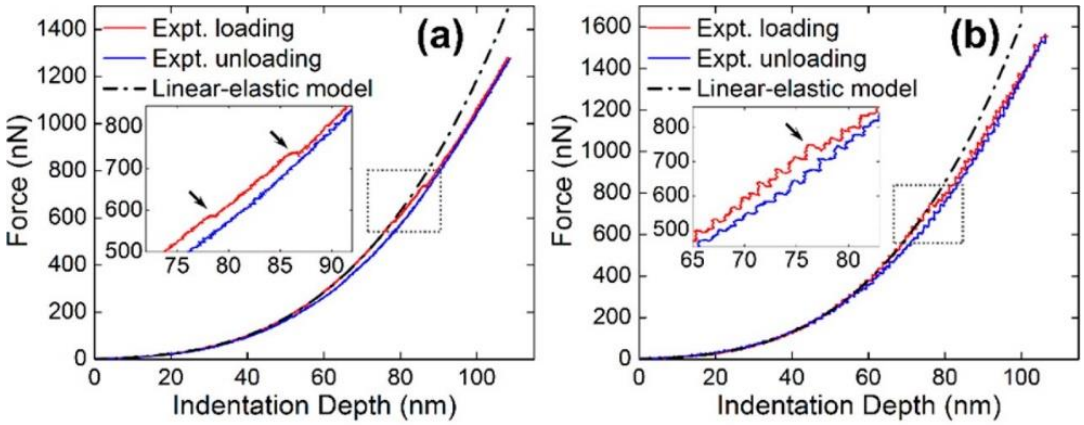

Figure 4-3. Experimental curves highlighting the hysteresis in bilayer (a) and trilayer (b) graphene sheets.

The CG MD simulation reproduces the kink as the deflection increases and the hysteresis takes place during the loading/unloading cycle, as shown in Fig. 4-4(a) for trilayer commensurate and non-commensurate stacking cases. The activation force for the kink for the commensurate stacked trilayer (~ 550 nN) is higher than that for the non-commensurate stacked trilayer (~ 380 nN). This can be attributed to the strong interlayer interactions between graphene layers in commensurate stacking compared to non-commensurate cases. Interestingly, in the CG-MD simulations, the unloading segments also coincide with the loading segments as the tip retracts to its original position, indicating the systems return to their original state when fully unloading.

A close inspection of the CG beads trajectories during the loading/unloading process reveals that recoverable interlayer slippage is the corresponding mechanism for this repeatable energy dissipation phenomenon, where the onset of the interlayer slippage coincides with the kinks in the force vs. deflection curves. Each slippage event corresponds to part of the interface overcoming energy barriers from initial energy minima state to the adjacent energy minima state, due to the shear force induced by indentation. During unloading, the whole system will return to the initial

energy minima state. Thus, it gives rise to the close hysteresis loop. This type of mechanically activated slippage has also been suggested by first-principles calculations [148, 149].

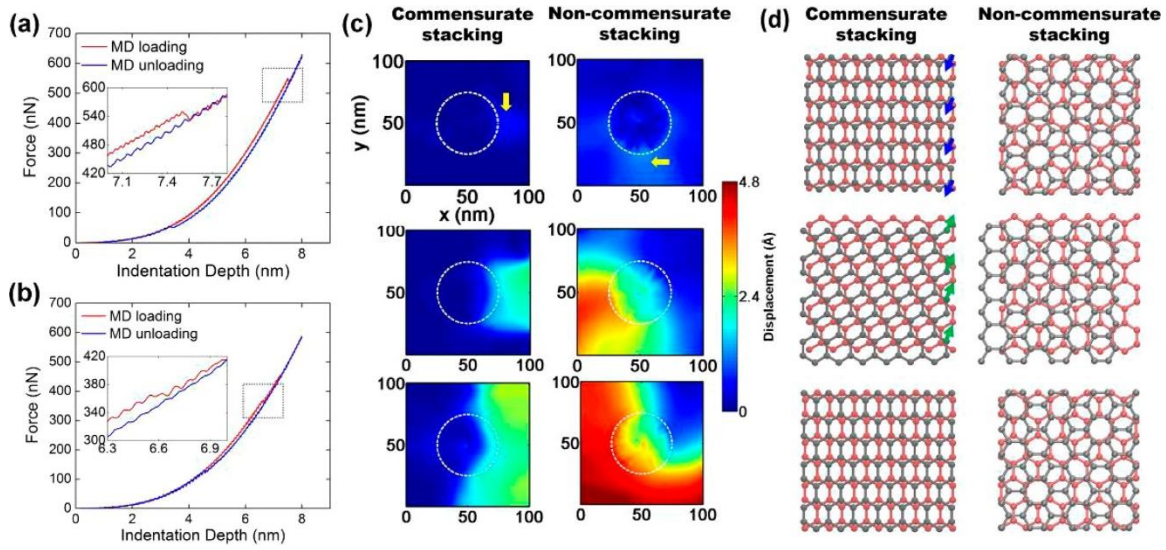

Figure 4-4. Characterization of recoverable interlayer slippage mechanism using CG MD simulation. (a) and (b) show both commensurate and non-commensurate stacked trilayer graphene hysteresis observed through simulations. (c) Time evolution of the slippage events responsible for the onset of hysteresis in commensurate stacked (left column) and non-commensurate stacked (right column) trilayer system. Each plot shows the in-plane (x-y plane) accumulated relative displacement between the middle layer and the bottom layer. The white dash circle indicates the hole rim and the yellow arrow indicates the position where the slippage is initiated. (d) Recoverable atomic slippage between the middle layer and bottom layer for commensurate stacking (left column) and non-commensurate stacking (right column). The arrows show the slippage direction of the lattices.

In Fig. 4-4(c), we characterize the slippage process observed in simulations by measuring the accumulated relative displacements between the middle layer and bottom layer projected in the basal plane (x-y plane) for both commensurate and non-commensurate stacked trilayer graphene.

As film deflection increases, slippage initiates at a location near the boundary of the circular suspended region and subsequently propagates along the periphery. This is logical since the interlayer shear stress maximizes there. Afterwards, the slippage propagates along the contour of the sheet. Fig. 4-4(d) shows more detailed information about the atomic-level slippage between the bottom and middle layers of a small region near the periphery. For the commensurate stacking case, the slippage follows a stick-slip mechanism, with sharp jumps between different states during loading and unloading. For non-commensurate stacking, the periodic energy barriers in the interlayer shear landscape still exist but their magnitude is significantly smaller. As a result, the slippage is observed to be more progressive, especially during the unloading process. It is worth noting that similar dislocation reversibility was reported in penta-twinned silver nanowires [150, 151]. This recoverable slippage process leads to an energy dissipation mechanism. The dissipated energy scales with the stacking order, as shown in Fig. 4-4(a), and we also expect that the dissipated energy would scale up if the slippage could be activated in multiple interfaces as the number of layers increases. This repeatable energy dissipation mechanism has great potential in future applications such as enhanced acoustic damping in nanoelectronics devices.

4.2 Size-dependent measured strength of multilayer graphene

From the nanoindentation experiment, one can also derive the intrinsic strength of the materials. The previously measured intrinsic strength of monolayer graphene is 130 GPa [4]. Previous work suggests that there is a scaling relationship between rupture force and the strength: $\sigma \propto \sqrt{F/t}$, where t is the thickness of the film under nanoindentation [152]. Thus, from the rupture forces for monolayer, bilayer, and trilayer graphene sheets, we can derive the effective strength (measured by nanoindentation) for bilayer and trilayer sheets using $\sigma_{eff} = \sigma_{mono}\sqrt{F_f \big/ nF_{mono}}$,

where $\sigma_{\text{mono}} = 130\ GPa$, $n = 2\ or\ 3$, and F_{mono} and F_f are the rupture forces for monolayer graphene and n-layered, respectively.

The nanoindentation measured effective strengths for mono-, bi-, and trilayer systems are 130 GPa, 127 GPa, and 109 GPa. This decreasing trend of measured strength is similarly observed for the simulation data using the same calibration approach, as shown in Fig. 4-5(b). This can be explained by the CG MD simulation results that the strain across layers is inhomogeneously distributed in the thickness direction with tensile strain is larger and more spread out in the bottom layer, as shown in Fig. 4-5(a). The interlayer slippage, once it occurs, magnifies uneven stress distributions among individual layers. The higher stress level in the bottom layer then leads to the premature failure of multilayer systems, and thus lowers the effective material strength. Interestingly, the non-commensurate stacked systems show a more significant decreasing trend. This is due to the lower interlayer shear strength and earlier interlayer slippage in the non-commensurate stacked systems.

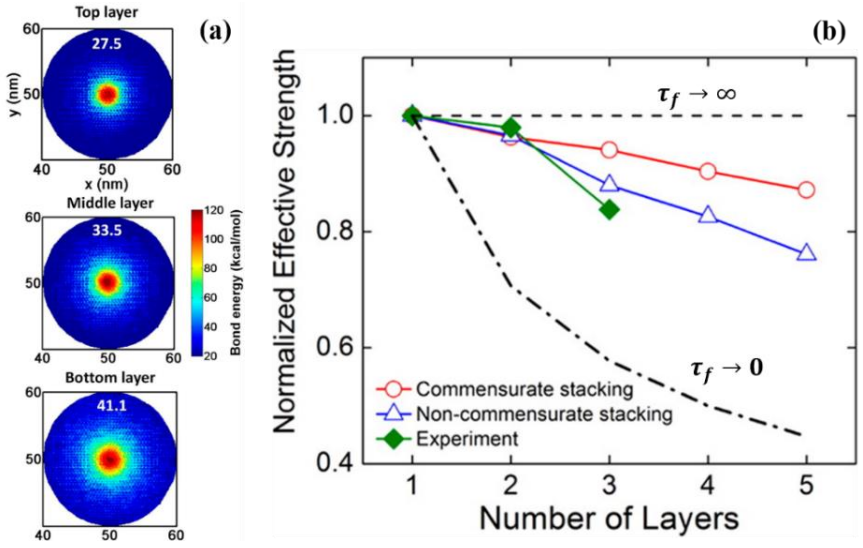

Figure 4-5. Inhomogeneous strain distribution among layers and thickness-dependent effective strength.

To emphasize the effect of interlayer shear behavior on effective strength measured under nanoindentation, we consider two limiting hypothetical cases. First, if interlayer shear strength is infinitely large ($\tau_f \to \infty$), the multilayer system behaves as a single sheet and the strain distribution among layers would be identical. Thus, the effective strength will remain close to the value of monolayer graphene regardless of the number of layers, assuming the bending contribution is negligible. Second, the individual layers are perfectly lubricated ($\tau_f \to 0$). In this case, the bottom layer carries most of the load, and the rupture force of the multilayer system would be close to that of a monolayer system. Thus, the effective strength would decrease with $n^{-1/2}$. To further prove the two hypothetical cases, we simulate two systems, one with very high interlayer interaction, and the other with extremely low interaction between layers. By changing the interlayer interaction, we can modify the interlayer shear strength accordingly. We find that for the higher interlayer shear strength case, the effective strength is higher than those in the original commensurate stacking case and approaches the limiting value of 1. For the lower shear strength case, the effective strength decreases more significantly. Therefore, the effective strength extracted from nanoindentation measurement is greatly affected by the interlayer shear strength, which should be taken into account in the strength measurements of other 2D materials [153].

4.3 Composition-dependent of nanoindentation behavior of GO membrane

The mechanical properties of GO sheets have been experimentally studied using the same nanoindentation technique [145]. Different from pristine graphene case where there are small variances in the force vs. deflection curves and derived effective strength, GO membranes not only show a large range of rupture force, but also exhibit two types of force vs. deflection responses for suspended GO membranes that correspond to ductile and brittle failure modes, respectively, as shown in Fig. 4-6. In the ductile failure mode, only the initial stage of deflection can be fit to linear

elastic membrane model (Eq. 4-1), beyond which the GO deform inelastically until rupture. In contrast, the linear elastic behavior through the deflection with sudden rupture is observed in the brittle failure mode.

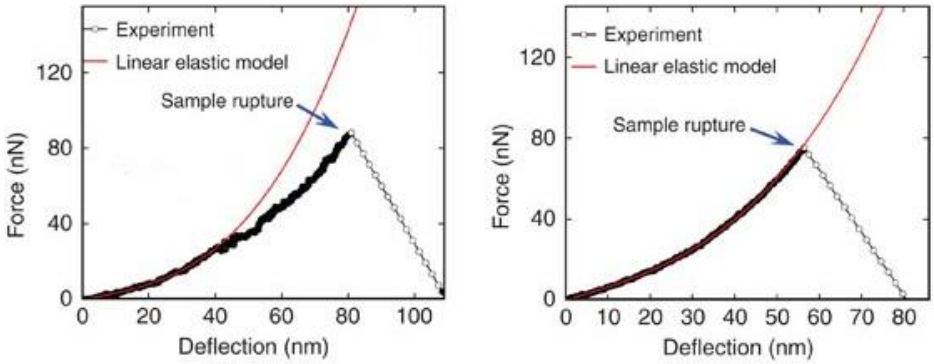

Figure 4-6. Characterization of GO membrane using nanoindentation. Typical ductile (left) and brittle (right) force vs. deflection curves for different GO membranes. Adapted from Wei et al., Nat. Commun. 2015.

Then, we carry out nanoindentation simulation on monolayer GO with the CG model we have developed. Specifically, we compare three types of GO sheets: one without functional groups, same as a monolayer pristine graphene sheet, one with 70% hydroxyl oxidation, and the last case is a 70% epoxide oxidation GO sheet. We use the same in-plane dimensions as the ones used in the graphene sheets in the last section. Same simulation procedures are also applied.

Fig. 4-7 depicts the force vs. deflection curves for the three GO sheets studied here. We apply the linear elastic membrane model (Eq. 4-1) to fit the small deflection range (~ 50% of maximum indentation depth) for each case. The results show that the force vs. deflection curve of graphene slightly deviates from the analytical model in the large deformation range, similar to what we have observed in the last section. This deviation has been attributed to the nonlinear elastic behavior of graphene, as also shown in Fig. 3-2. For the epoxide oxidation case, the deviation from analytical

model happens earlier and it is more obvious. This large deviation comes from the obvious nonlinear ductility of epoxide-oxidized GO sheets, as illustrated in Fig. 3-7. The ductility of this type of GO sheet also results in the largest rupture depth, although the rupture force of epoxide-oxidized GO sheet is lower than that of the graphene sheet. For hydroxyl oxidized case, given that 70% hydroxyl oxidation renders the GO sheet brittle (Fig. 3-6), we see no observable deviation between the force vs. deflection curve and the analytical model, and the rupture depth is the smallest.

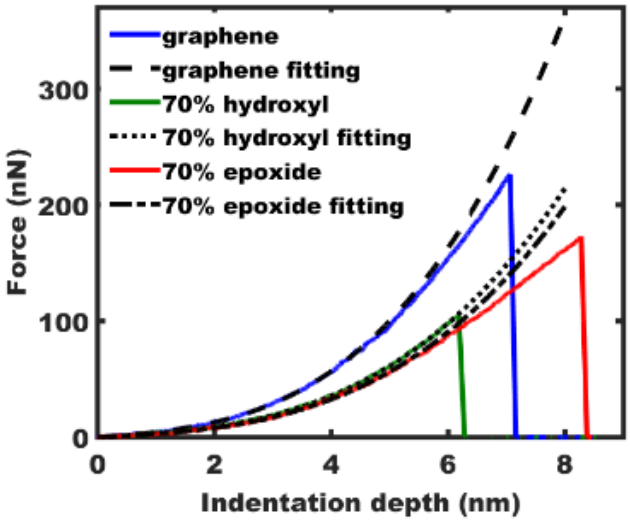

Figure 4-7. Simulation results of nanoindentation on three types of GO sheets. The linear elastic membrane model for each case is also plotted with dashed lines.

The comparison between the hydroxyl-oxidized case and epoxide-oxidized case corresponds to the two typical modes observed experimentally. Our CG MD simulation results suggest that the failure mode highly depends on the chemistry composition of the contact area between the indenter and membrane. If the contact area is predominantly occupied by epoxide groups, we anticipate a ductile failure model, while brittle failure could occur when the indenter interacts with a hydroxyl-rich area. The fact that our CG MD simulations help to explain the experimental data for the GO

nanoindentation case further demonstrates the prediction potential of our CG model. It also illustrates the importance of explicit representation of discrete heterogeneity regions in the CG model to capture the intrinsic mechanical properties of the target systems.

4.4 Fracture toughness of graphene and GO sheets

Fracture toughness is defined as the capability of a material with preexisting cracks and defects to resist total fracture or failure [154]. It is a critical mechanical property as it determines the structural integrity and reliability. The usefulness of a material is thus usually determined by its fracture toughness rather than its intrinsic strength. Theoretical and computational modeling in recent literature has provided insights into the fracture mechanisms of graphene and GO sheets [20, 27, 155-158]. Recently, the fracture toughness of graphene and GO have been measured separately [26, 159, 160]. Specifically, it has been found that Griffith theory of brittle fracture applies to continuum bilayer graphene specimen, and the fracture toughness was measured as the critical stress intensity factor of $4.0 \pm 0.6\ MPa\sqrt{m}$ and the equivalent critical strain energy release rate of $15.9\ Jm^{-2}$ [26]. The intricacies of the crack tips were difficult to consider purely by the experimental method. Then, Wei and coworkers applied finite element analysis to resolve the stresses at the crack tips and determined the critical stress intensity factor of multilayer graphene to be $12.0 \pm 3.9\ MPa\sqrt{m}$ [159], much higher than the values for that of bilayer graphene. The energy release rate of multilayer GO specimen was determined to be two times higher than graphene and it was found that linear fracture analysis, i.e. Griffith theory, overestimates the fracture toughness [160]. The reason was attributed to the nonlinear nature of GO sheets [160]. However, in this study, the crack shape was not precisely controlled and there was obvious crack tip blunting due to the electron irradiation method used, and this should be the primary reason for the inapplicability of linear fracture analysis. As a result, the experimental characterization

methods still suffer from many technical difficulties, such as generating cracks and controlling crack shape. In addition, the experimental measured fracture toughness has very large variances.

Here, we apply our CG models to investigate the fracture toughness of monolayer graphene and GO sheets by accurately controlling the crack shape and size. According to the Griffith fracture criterion for a central crack of length $2a_0$:

$$\sigma_c\sqrt{\pi a_0} = \sqrt{2\gamma E} \tag{4-2}$$

where the left-hand side is the critical stress intensity factor $K_c = \sigma_c\sqrt{\pi a_0}$, σ_c is the failure far-field stress, and the right-hand side term depends only on material properties (E is the Young's modulus and γ is the surface energy, i.e. edge energy for 2D materials like graphene).

We first generate graphene systems with different initial crack length, and the width of the crack is kept constant as 1 nm. Fig. 4-8(a) shows the initial configuration of the system with $a_0 = 3\ nm$. Fig. 4-8(b) shows the propagating crack after reaching critical stress σ_c. The catastrophic crack propagation verifies the nature of the brittle failure, which is also manifested by the linear response in the stress-strain curves shown in Fig. 4-8(c).

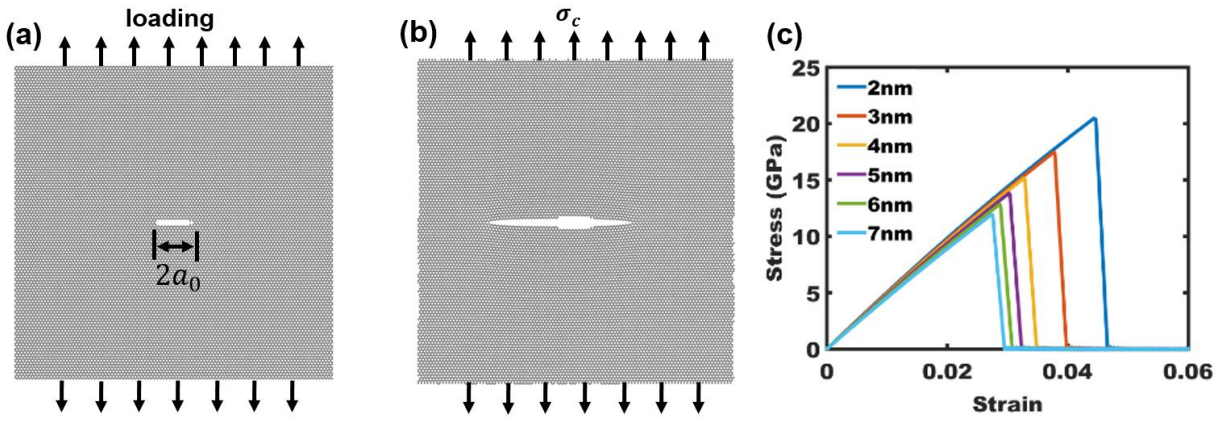

Figure 4-8. Schematic of the simulation setup for calculating fracture toughness of monolayer graphene. (a) Initial configuration of a graphene sheet with a central crack $a_0 = 3\ nm$. (b) The

state of catastrophic crack propagation. (c) Stress-strain relationships for sheets with different crack lengths.

Table 4-1 lists the results of σ_c for systems with different crack lengths and the calibrated K_c values. Here, the K_c is calibrated by using monolayer thickness of graphene as 0.34 nm. We note that the curves shown in Fig. 4-8(c) assume the thickness of the system is 0.75 nm, to be consistent with GO sheets shown later. The converted results show that K_c is approximately constant, further corroborating that Griffith criterion is applicable to describe the fracture of monolayer graphene. In addition, the obtained K_c value of 3.77 $MPa\sqrt{m}$ is consistent with the experimental measured value for bilayer graphene sheets, thus validating each other and indicating that there is not much crack tip blunting effect in the experiments. Since we also capture the Young's modulus of graphene accurately, according to Eq. 4-2, the edge energy is also conserved in our CG model.

Table 4-1. Simulation data of crack size, critical fracture stress and critical stress intensity factor K_c of monolayer graphene.

$a_0\ (nm)$	$\sigma_c\ (GPa)$	$K_c\ (MPa\sqrt{m})$
2	45.2	3.60
3	38.6	3.75
4	33.5	3.75
5	30.4	3.82
6	28.2	3.88
7	26.3	3.88
Average		3.77
Standard Deviation		0.11

The same procedure is used to measure the fracture toughness of both hydroxyl-oxidized and epoxide-oxidized GO sheets with a 70% degree of oxidation. Interestingly, although epoxide-oxidized GO without cracks shows an obvious non-linear response during uniaxial tension, it exhibits nearly linear response before failure and much smaller failure strain when a defect is present, as shown in Fig. 4-9. The linear stress-strain behavior as well as the catastrophic crack propagation observed indicate the likely applicability of Griffith theory. The measured K_c is $1.00 \pm 0.04\ MPa\sqrt{m}$ for the hydroxyl case, and $1.16 \pm 0.03\ MPa\sqrt{m}$ for the epoxide case, by assuming monolayer thickness as 0.75 nm. Notably, the measured K_c of epoxide-oxidized GO is 16% larger than that of hydroxyl-oxidized GO, which further corroborate the influence of chemistry on the fracture toughness and in agreement with previous reports that epoxide-rich GO has higher toughness [143]. We note with interest that the difference between K_c obtained herein and experimentally [160] indicates potential fracture toughness enhancement in the multilayer structures, such as possible crack pathway deflections. In addition, the fracture toughness of materials can be influenced by crack blunting and polycrystalline microstructure, as investigated in recent studies for graphene case [20].

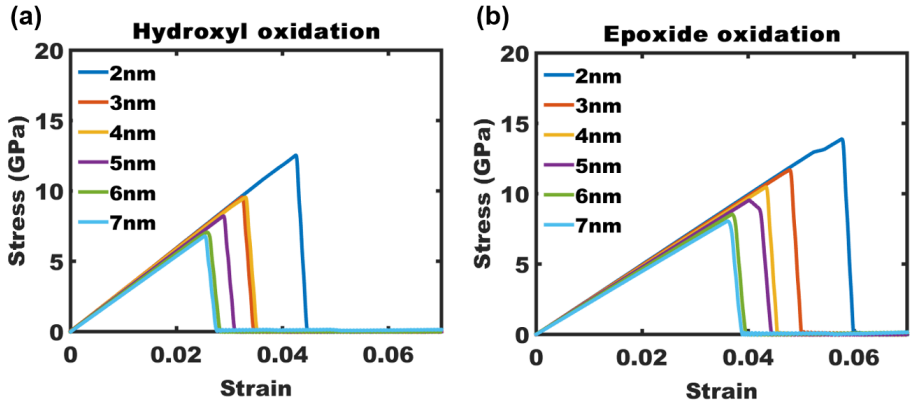

Figure 4-9. Stress-strain relationships for hydroxyl-oxidized and epoxide-oxidized GO sheets with different crack lengths.

4.5 Conclusion

In conclusion for this chapter, the applicability and potential of CG models of graphene and graphene oxide in studying the deformation mechanisms and properties involving large deformation and failure are demonstrated. Firstly, CG-MD simulations have been utilized to thoroughly characterized the deformation and effective strength of MLG combined with nanoindentation experiments. The CG-MD simulations provide new physical insights into the mechanical behavior of MLG during the indentation loading and unloading processes. A recoverable slippage mechanism between graphene layers is observed to account for the closed hysteresis loop observed in experimental loading/unloading cycle. More interestingly, the interlayer slippage is activated when an orientation-dependent critical shear stress threshold is reached. In addition, the simulation results illustrate that the finite interlayer shear strength would lead to a difference in nanoindentation measured strength when graphene samples are scaled in the thickness direction. Next, the mechanical response of monolayer GO under nanoindentation is studied. Either ductile or brittle failure occurs depending on different contact area chemistries, thus corroborating previous experimental observations. Lastly, the CG models are also applied to measure the fracture toughness of both pristine graphene sheets and GO sheets. The measured fracture toughness of pristine graphene is consistent with previous experimental and computational studies, and the results suggest the applicability of classic Griffith theory of brittle fracture. The chemistry at the crack tip is shown to influence the fracture toughness of the GO sheets. Additionally, the lower K_c values measured here for GO sheets compared to experiments suggest potential fracture toughness enhancement in the multilayer structures.

Chapter 5: Application of CG Model in Ballistic Impact

Understanding the ballistic impact response of materials is important for diverse applications that occur at small as well as large scales, including therapeutic delivery of nanoparticles to cells [161, 162], designing impact-resistant electronics [163], body armors [164], or space debris shields [165]. Microscale ballistic experiments, most notably the laser-induced projectile impact tests (LIPIT) established recently broke new ground in this area [61], bringing projectile and membrane sizes down to the micro and nanoscale [166-168]. This now allows direct characterization of the influence of nanostructures on ballistic resistant performance, leading to new barrier concepts based on polymer nanocomposites and 2D nanomaterials. LIPIT experiments on MLG have shown that the specific penetration energy for MLG membrane is about 10 times than the corresponding literature values for macroscopic steel sheets [166], which shows MLG's potential as a ballistic barrier material. These findings correspond to the delocalization of concentrated stress, i.e. an impact propagation zone (IPZ), as well as graphene's exceptional specific strength. Specifically, the failure process of MLG membrane involves a cone wave developed in the wake of impact, which forms the IPZ, and radially propagating cracks that give rise to petals [166]. Inspired by this experiment, atomistic MD simulations have been applied to simulate the failure mechanisms of graphene membrane under ballistic impact [103, 104, 169]. But these simulations are limited to very small sizes to minimize computational effort. Multiscale computational approaches and continuum theories offer greater promise to bridge different length and time scales in order to better understand the failure processes.

In this chapter, the CG model of graphene is utilized to investigate the ballistic impact behavior of thin MLG sheets. The characteristics of the dynamic process are accurately captured. The simulation results also reveal distinctive failure mechanisms that deteriorate the ballistic resistance

of MLG sheets. Specifically, the cone wave formed upon impact – which travels in-plane at a very high speed in thin graphene membranes – can reflect from clamped boundaries and induce early perforation [170]. In addition, the compressive wave in the thickness direction could result in spalling failure [171], a phenomenon previously observed in the impact on the macroscopic concrete specimen. Portions of the text and figures within this chapter are reprinted or adapted with permission from Meng et al. Extreme Mechanics Letters 2017 [170] and Meng et al. Carbon 2018 [171].

5.1 Cone wave effect on ballistic resistance of graphene membrane

In this section, we study the effect of finite specimen size on the ballistic response of single and MLG membranes, particularly focusing on the effect of cone wave reflection from boundaries on the deterioration of ballistic resistance, by performing MD simulations with the CG model of graphene. We also study the projectile impact behaviors of graphene membranes with different sizes, thicknesses, and shapes for the suspended free-standing region. Finally, we present an analytical relationship, verified by simulation data, which predicts the relationship between the critical membrane size below which the cone wave reflections return to the projectile surface and induce perforation and system's geometrical factors.

5.1.1 Simulation setup

The CG model of graphene is used for the square graphene sheets with varying number of layers and different dimensions. The in-plane direction of the sheets is along the x-y plane. In the default setting, a circular region is defined in the center of the square sheets to represent the free-standing impact region, and the beads outside of the free-standing region are fixed to represent the clamped boundaries used in experiments. At the center point of the square sheet with a vertical distance larger than 5nm, we generate the spherical projectiles by adopting a diamond cubic lattice

structure with a lattice constant of 0.72 nm. The default projectile bead mass is 96 g/mol, which gives rise to a projectile density of 3.42 g/cm^3. During the simulation, the projectile is treated as a rigid body, since no appreciable deformation of the projectile is found in the microballistic experiments [166]. The interactions between the projectile and graphene membrane are modeled by the same 12-6 LJ potential as the ones used for interlayer interactions in the CG model of graphene: $\varepsilon_{LJ} = 0.82\ kcal/mol$ and $\sigma_{LJ} = 3.46$ Å. We have verified that LJ parameters have a negligible effect on the ballistic impact response. Specifically, the reactive force and projectile velocity evolution are approximately the same with varying ε_{LJ} parameter. The system is first equilibrated under an NVT ensemble at 10 K with the projectile fixed at the initial position. A low temperature is chosen to minimize thermal noise in the results. To simulate the ballistic impact, the projectile is given an initial velocity vertically towards the graphene membrane. And, the system is run under an NVE ensemble to conserve the total energy.

5.1.2 Reduced ballistic limit velocity due to cone wave reflection

Fig. 5-1 shows the typical residual velocities (V_r) vs. initial velocities (V_0) relationship for a circular freestanding monolayer graphene membrane with a radius of $a = 100\ nm$ impacted by projectiles with different radii (r_p). The ballistic impact behavior of the membrane can be broken into three distinct regions based on V_r. Region I corresponds to the scenario when the projectile cannot penetrate the membrane and bounces off, as indicated by the negative values of V_r. At greater V_0, V_r suddenly changes from negative to positive, marking the onset of region II and a transition from projectile bouncing back to penetration. We take the lowest V_0 that results in penetration as ballistic limit velocity (V_{50}). In this regime, an obvious IPZ forms and expands outwardly through the cone wave propagation. Further increasing V_0 leads to region III, where V_r scales linearly with V_0. In this regime, the projectile immediately perforates the membrane locally,

and the linear scaling can be expected from conservation of momentum. By comparing the responses of different projectile sizes, we can see that V_{50} decrease with increasing projectile sizes. But interestingly, for a much larger projectile with radius $r_p = 15\ nm$ plotted in magenta, even very small V_0 results in perforation.

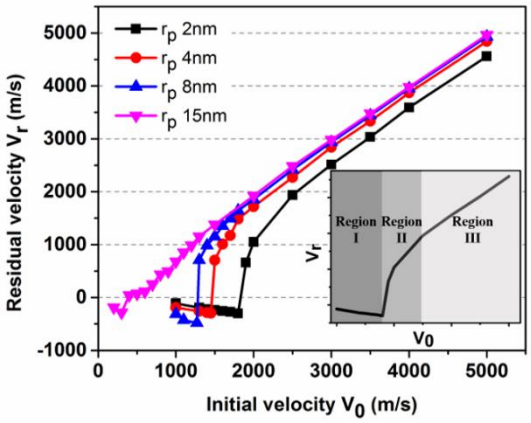

Figure 5-1. Residual velocity vs. initial velocity relationship for different radii projectiles impacting on a circular membrane with a radius of 100 nm. The inset shows the general shape of the relationship and three corresponding regions.

The specific V_{50} values for a wider range of projectile sizes are presented in Fig. 5-2. An analytical expression for the V_{50} of an infinite, linear elastic, thin isotropic membrane has been derived as [172]:

$$V_{50} = \sqrt{2}(1+\Gamma)c_0(\varepsilon_{max}/K_{max})^{3/4} \tag{5-1}$$

where $\Gamma = \frac{m_m}{m_p}$ is the mass ratio of the part of the membrane (m_m) in contact with the projectile (m_p), $c_0 = \sqrt{\frac{E}{\rho}}$ is the elastic wave speed in the membrane, ε_{max} is the in-plane failure strain of the membrane and K_{max} is a strain concentration factor depending on both Γ and ε_{max}. For simplicity, we assume that K_{max} mildly depends on Γ, so for a given membrane material, ε_{max} and K_{max} can

be taken as constants. Given that $m_m \sim r_p^2$, and $m_p \sim r_p^3$ for spherical projectiles, a rough scaling yields that $V_{50} \sim A + B/r_p$ from Eq. (5-1). Then, we fit the scaling curve for the results of the projectile radius smaller than 8 nm. The V_{50} values for smaller projectiles follow this scaling, however, for larger projectiles, the V_{50} deviates considerably from the predicated relationship. This size-dependent deviation cannot be explained by current theoretical models. It should be related to the finite size of the simulation systems.

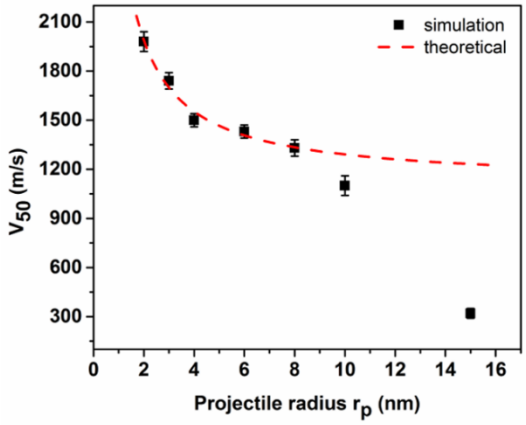

Figure 5-2. Ballistic limit velocity vs. projectile radius with the analytical scaling relationship shown in red dashed line.

To better understand the deviation, we visualize the complete impact process from simulation trajectories. We observe that for a large projectile, the cone wave propagates outward radially until it reflects from the circular clamped boundary, as seen in Fig. 5-3(b). The reflected cone wave travels back towards the projectile, further deforming the membrane downward, and upon reaching the surface of the projectile, it generates a large local strain that leads to immediate perforation of the membrane, Fig. 5-3(c). We note that the perforation would not happen if the cone wave did not return. This observation indicates that when the projectile to membrane size ratio is relatively large, the membrane loses part of the projectile-proof capability due to the cone wave reflection

from the boundaries. This issue brings forward the following interesting questions: What is the critical size relationship between the membrane and the projectile that governs cone wave reflection? Which material properties influence this scaling relationship?

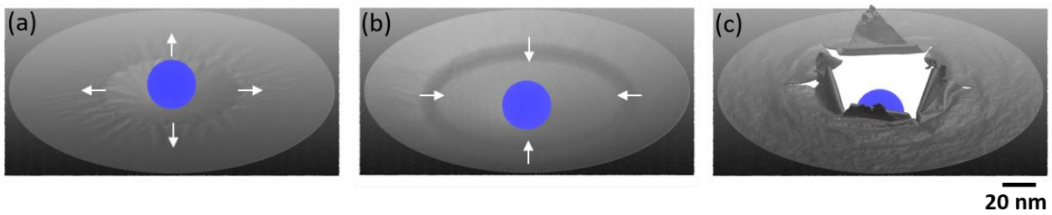

Figure 5-3. Simulation snapshots of the cone wave reflection process in monolayer graphene. (a) Cone wave propagates outwardly. (b) Cone wave gets reflected and returns towards the center. (c) Cone wave encounters the projectile surface and subsequent catastrophic failure. The simulation conditions are: $a = 100\ nm$, $r_p = 100\ nm$ and $V_0 = 500\ m/s$.

5.1.3 Derivation of the critical size relationship

We define the critical membrane size a_c for a given projectile size r_p as the size at which the cone wave returns to the projectile at the instance of maximum deflection. We calculate two periods of time: (a) the total time t_c taken by the cone wave to reflect from the boundary and return to the surface of the projectile, and (b) the time t_p taken by the projectile to come to a full stop. Setting these two times as equal will yield the critical size relationship.

According to Phoenix and Porwal's work [172], after a sharp increase in the speed of expanding cone wave, the wave speed stays approximately constant (v_{c0}) afterwards. However, the speed of the reflected cone wave will be different because the wave speed depends on the local membrane strain of the wave front, and during reflection, the membrane is in stretched state. The total traveled time of cone wave t_c has been derived rigorously in our work [170]:

$$t_c = k_1 \frac{2a_c}{v_{c0}}, k_1 \cong 0.78 \tag{5-2}$$

where k_1 is introduced to account for the higher reflected cone wave speed.

To calculate t_p, the reactive force expression for a 2D linear elastic isotropic membrane is used [172]:

$$F = \pi \rho_m h_m V(t) d(r_c)^2/dt \tag{5-3}$$

where r_c is the cone shape region radius, ρ_m and h_m are the membrane density and thickness, respectively, and $V(t)$ is the projectile velocity as a function of time, which decreases with time during impact. Although r_p does not appear in Eq. (5-3), the deceleration rate depends on m_p, and thus, r_p plays a role inside $V(t)$.

In the finite system, Eq. (5-3) is valid before the cone wave reaches the boundary at time t_1. To get a more accurate expression of the reactive force, we divide the overall process into two phases. In the first phase, the cone wave expands outwardly with constant speed $r_c = v_{c0}t$, so the reactive force can be written as:

$$F_1 = 2\pi \rho_m h_m V(t) v_{c0}^2 t \tag{5-4}$$

During the second phase, when the cone wave gets reflected, r_c cannot increase any further. Simulations indicate that the reactive force stays approximately a constant in this phase, Fig. 5-4(a). Thus, it is reasonable to express the constant force as:

$$F_2 = 2\pi \rho_m h_m V(t_1) v_{c0}^2 t_1 \tag{5-5}$$

We compare force estimation from Eq. 5-4 and 5-5 with simulation results in Fig. 5-4(a). It shows good agreement. Specifically, it captures the increasing-decreasing trend in the first phase. The total error is less than 15%, which is obtained by calculating the total areas under the force

curves. The final peak in the actual force curve occurs when the reflected wave encounters the projectile. Finally, the force drops to zero sharply, indicating failure of the membrane.

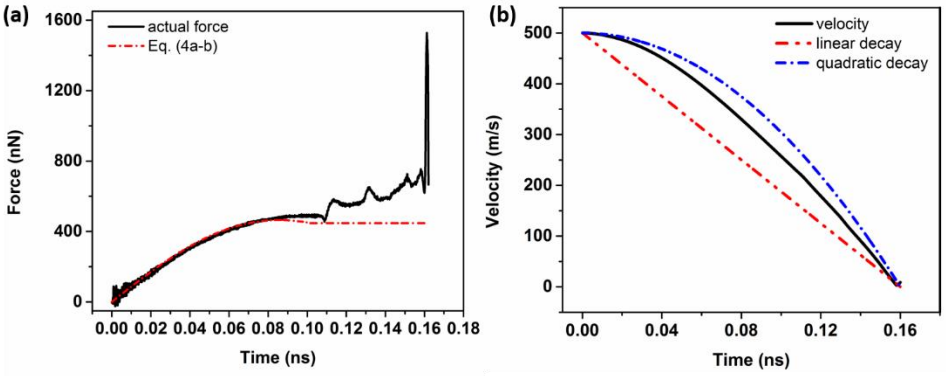

Figure 5-4. Estimation of reactive force and projectile velocity.

For the complete impact process, the impulse given to the projectile in time t_p by the reactive force is equal to the total change in its momentum. This can be expressed as:

$$\int_0^{t_p} F dt = \int_0^{t_1} F_1 \, dt + \int_{t_1}^{t_p} F_2 \, dt = m_p v_p \tag{5-6}$$

Solving the above equation by assuming that the velocity decays with a scaling that lies between linear ($V(t) = v_p - v_p t/t_p$) and quadratic function of time ($V(t) = v_p - v_p t^2/t_p^2$), as shown in Fig. 5-4(b), we then obtain the projectile halting time:

$$t_p = \frac{2k_2}{v_{c0}} r_p^{1.5} \left(\frac{\rho_p}{\rho_m}\right)^{0.5} \left(\frac{1}{h_m}\right)^{0.5} \tag{5-7}$$

where k_2 lies in the range of 0.75-0.91, and the lower and upper bounds correspond to quadratic and linear velocity decay, respectively.

Setting $t_p = t_c$, we finally have:

$$a_c = \frac{k_2}{k_1} r_p^{1.5} \left(\frac{\rho_p}{\rho_m}\right)^{0.5} \left(\frac{1}{h_m}\right)^{0.5} \quad (5\text{-}8)$$

In our simulations, $\frac{\rho_p}{\rho_m} = 1.55$ ($\rho_p = 3.42\ \frac{g}{cm^3}$ and $\rho_m = 2.2\ \frac{g}{cm^3}$), $h_m = 0.34\ nm$ for monolayer graphene, as a result $\frac{k_2}{k_1}\left(\frac{\rho_p}{\rho_m}\right)^{0.5}\left(\frac{1}{h_m}\right)^{0.5}$ lies between 2.05-2.49, and the lower and upper bounds correspond to quadratic and linear velocity decay, respectively.

From CG MD simulations, we determine the critical membrane sizes for different projectile sizes by tracking whether the failure caused by the reflected cone wave happens at approximately the same time when the projectile attains zero velocity. The results are shown in Fig. 5-5, where the theoretical predictions $a_c = Cr_p^{1.5}$ with C equals to 2.05 and 2.49 (linear and quadratic velocity decay bounds) are also plotted. The theoretical fitting agrees very well with our simulation results.

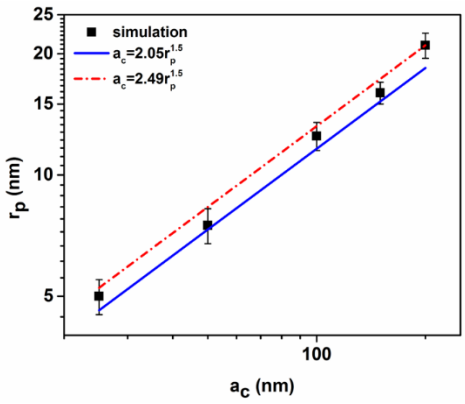

Figure 5-5. Comparison of the simulation results and the analytical critical relationship.

5.1.4 Validation of the critical size relationship

To further validate the accuracy of the critical scaling relationship of Eq. 5-8, such as the density ratio and the membrane thickness. We have conducted several additional simulations. First, we change the densities of the projectile and membrane while keeping their ratio $\frac{\rho_p}{\rho_m}$ a constant and we observe that the critical size relationship between the membrane and the projectile remains the

same. Then, by doubling the projectile density ρ_p while keeping the same membrane density, we find that the critical projectile size decreases for a given membrane size, as shown in Table 5-1. Given a_c, ρ_m and h_m as constants, Eq. 5-8 yields $(\frac{r_{p1}}{r_{p2}})^{1.5} = (\frac{\rho_{p2}}{\rho_{p1}})^{0.5}$, where $\frac{\rho_{p2}}{\rho_{p1}} = 2$. From our simulation data, we also have $log_2\left(\frac{r_{p2}}{r_{p1}}\right)^{1.5} \approx 0.5$, thus verifying the scaling order for $\frac{\rho_p}{\rho_m}$ as 0.5. Finally, we have also run monolayer to trilayer membrane simulations, and we find that the projectile density should increase double and triple times accordingly for bilayer and trilayer membrane to keep the critical size relationship between membrane and projectile, thus verifying the exponent of $\frac{1}{h_m}$ also as 0.5. Specifically, Fig. 5-6 shows the cone wave reflection process for a bilayer membrane with $a_c = 100nm$, $r_p = 12.5nm$ and $\rho_p = 6.84\ g/cm^3$. The reflected cone wave also emerges (Fig. 5-6(a)), and when it encounters the bullet surface, immediate perforation occurs (Fig. 5-6(b)).

Table 5-1. Verifying the scaling order of the density factor.

$a_c\ (nm)$	$r_{p1}\ (nm)$ (projectile density 3.42 g/cm^3)	$r_{p2}\ (nm)$ (projectile density 6.84 g/cm^3)	$log_2\left(\frac{r_{p1}}{r_{p2}}\right)^{1.5}$
50	7.5	6	0.48
100	12.5	10	0.48
150	16	12.5	0.53
200	21	16.5	0.52

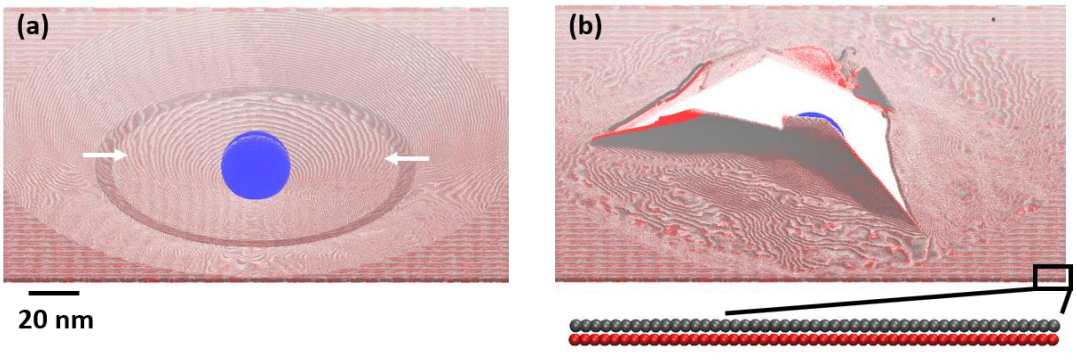

Figure 5-6. Simulation snapshots of the cone wave reflection process in bilayer graphene.

Moreover, Eq. 5-8 has several important ramifications. First, the critical membrane size increases with the projectile size to the power of 1.5, showing greater increase of membrane radius needed to achieve criticality as the projectile size increases. For a silica projectile with size $r_p = 2\,\mu m$, used in recent experiment [166], the calculated critical membrane size is $\sim 200\,\mu m$ for monolayer graphene. A larger thickness alleviates the reflected cone wave effect, while even for multilayer graphene, say 50 graphene layers, the critical membrane size is still $\sim 28\,\mu m$. It should also be noted that the reflected cone wave effect intensifies with higher projectile density. If gold projectiles instead of silica were used in recent experiments [166], the corresponding critical membrane size would increase by 2.7 times. These estimations indicate that it should be possible to observe and study the cone wave reflection effect with current microballistic techniques [61, 166]. Second, Eq. 5-8 is independent of the material properties, such as the Young's modulus. To validate this, we modify the force field parameters of the CG model in order to generate different membrane systems. Specifically, the bond and angle stiffness parameters are changed accordingly, which linearly scale with the Young's modulus of hexagonal symmetry sheet [127, 128]. The other two systems are those which have either half or double the Young's modulus of pristine graphene. By keeping the projectile size constant, we observe from the simulations that the reflected cone

wave always returns to the surface of the projectile at the time when the projectile reaches zero velocity for all the three systems. The analytical relationship derived here is thus generally applicable to membranes if cone wave and IPZ exist.

In addition, we note that although the derived theory for the reflected wave speed and projectile halting time is general, membranes with circular shape have the most reflected wave effect since the reflected wave returns to the center at the same time and causes the greatest strain concentration when encountering the projectile surface. An experimentally relevant question that arises from this analysis is what the free-standing membrane geometry should be to reduce the cone wave reflection effects on the ballistic performance, and *vice versa*, in which kind of boundary condition we could observe the most obvious wave reflection effect. For this purpose, we have also tested triangular and square shapes for the suspended free-standing area. Specifically, in the same square sheet with edge length of 105 nm, we define circular shape with diameter equal to 100 nm (Fig. 5-7 (a-b)), square (Fig. 5-7 (c-d)) and triangular shape (Fig. 5-7 (e-f)) with length of edge equal to 100 nm. We also show the cone wave reflection process in the Fig. 5-7 by coloring the beads per their out-of-plane positions, with red corresponding to lower position (further from the reader) and blue corresponding to higher position (closer to the reader). For circular shape, after the cone wave reflects from the fixed boundary simultaneously, the wave keeps the circular shape (Fig. 5-7(a)) and gets back to the center at the same time, which results in large strain concentration and failure of the membrane (Fig. 5-7(b)). However, the square shape membrane has much less cone wave reflection effect because the reflected cone waves from four edges interfere with each other (Fig. 5-7(c)) during traveling back and only part of it returns to the center (Fig. 5-7(d)). For triangular shape membrane, we see a moderate cone wave reflection effect. The shorter distance to the edges (Fig. 5-7(e)) and less time being required for the reflected wave to travel back give rise to a stronger

effect. However, only part of the reflected wave returns to the midpoint at a given instance, which limits the wave reflection induced strains compared to a circular membrane setting. In summary, we conclude that the clamped circular membrane setting is the boundary condition that maximizes the reflected cone wave effects among the shapes studied here.

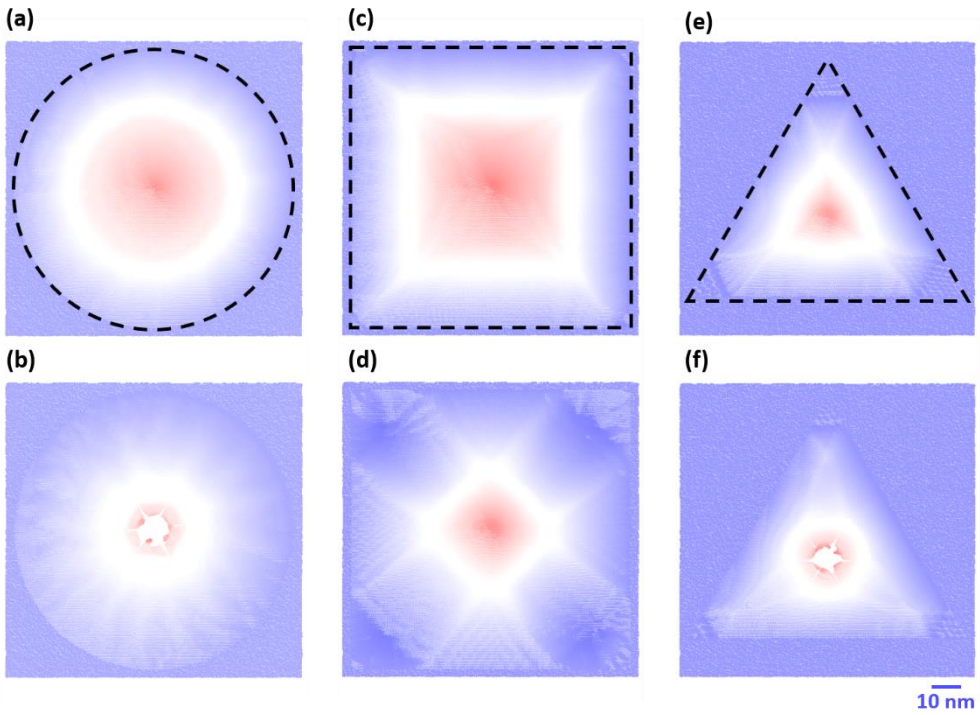

Figure 5-7. Cone wave reflection for free-standing membrane with different shapes. (a-b) circular shape, (c-d) square shape and (e-f) triangular shape. The beads outside of the freestanding region are fixed during the simulation. The beads are colored per their out-of-plane position, with red corresponding to lower (further from the reader) and blue corresponding to upper (closer to the reader).

5.2 Effect of geometrical factors on membrane ballistic penetration energy

In the previous section, we have shown that there exists a critical membrane size below which the cone wave returns to the projectile and induces immediate perforation, thus deteriorating the impact resistance of graphene membrane. However, we note that the deterioration happens even for a membrane larger than the critical size, but smaller than the size of the largest IPZ, as the size of IPZ indicates the actual deformed volume that contributes to the total impact energy absorbed. To illustrate this, we have conducted simulations with different membrane span size and measured the ballistic penetration energy (E_p) over a large impact velocity (V_i) range beyond V_{50}. The results are shown in Fig. 5-8.

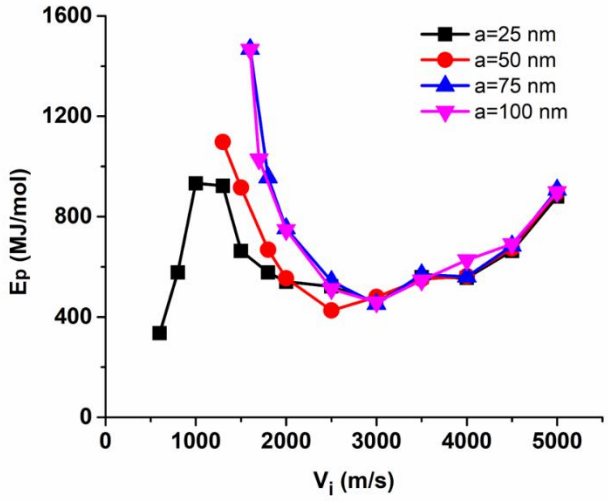

Figure 5-8. Ballistic penetration energy vs. impact velocity profile for different membrane span sizes.

For the membrane radius $a = 50\ nm$ case, even though the cone wave does not return back to the projectile in time, there is still a decrease in the energy absorption capability in low V_i regime. To estimate the size of actual deformed volume or the size of IPZ, we use the same theoretical

framework presented earlier. Before any penetration occurs, the reactive force profile can be expressed as:

$$F = 2\pi\rho_m h_m V(t) v_{c0}^2 t \tag{5-9}$$

We note that Eq. 5-9 is similar to Eq. 5-4 presented earlier, but without considering the wave reflection phase. The reactive force first increases to a maximum value and then decreases to zero, as also shown in our simulation result of a monolayer graphene, Fig. 5. The force decreasing to zero happens at the time when $V(t)$ becomes zero. The maximum force happens at a time during the deceleration process, and the value of maximum force increases with V_i, until reaching the critical force that results in film penetration, at which the projectile velocity is V_{50}.

Again, using momentum transfer theorem, we consider the projectile momentum change:

$$F = -m_p d(V(t))/dt \tag{5-10}$$

From Eq. 5-9 and Eq. 5-10, we can derive the explicit velocity and force expression:

$$V(t) = V_i \exp(-\frac{\pi\rho_m h_m v_{c0}^2}{m_p} t^2) \tag{5-11}$$

$$F = 2\pi\rho_m h_m v_{c0}^2 V_i \exp(-\frac{\pi\rho_m h_m v_{c0}^2}{m_p} t^2)\, t \tag{5-12}$$

From the force expression, we can also derive the critical time to reach the maximum force:

$$t_r = \sqrt{\frac{m_p}{2\pi\rho_m h_m v_{c0}^2}} \tag{5-13}$$

We have compared the theoretical estimations on velocity (Eq. 5-11) and force (Eq. 5-12) and the actual projectile velocity and reactive force from simulation in Fig. 5-9. The theoretical velocity matches very well with the actual velocity, and there is only a minor discrepancy between the forces. Also, the derived critical time for maximum force agrees perfectly with actual critical time. We would like to note that when the force reaches maximum value, $V(t)$ has not decreased to zero. As a result, there is always a residual velocity for the projectile after penetration. This is a

distinctive characteristic for projectile impact on thin membranes. However, when projectiles impact on thicker plates, where the friction between projectile and plates during penetration process is non-negligible [173], the residual velocity can be close to zero.

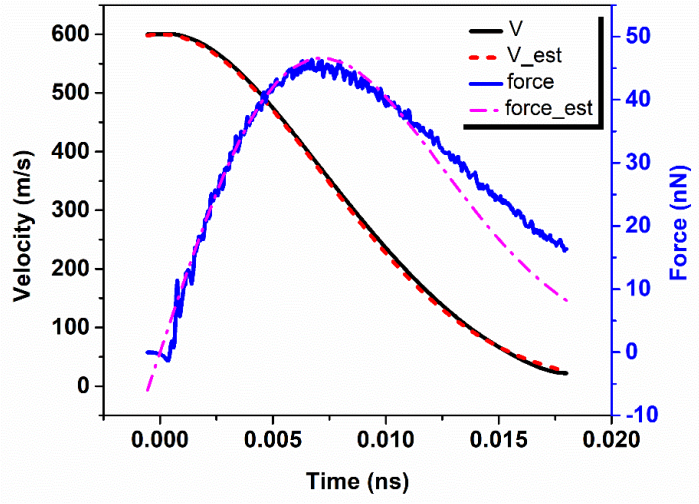

Figure 5-9. Projectile velocity and reactive force profile from simulation and theoretical estimation. The simulation settings are $h_m = 0.34\ nm$, $R = 4\ nm$, and $V_i = 600\ m/s$.

We can also see from Eq. 5-13 that t_r decreases with increasing V_i, as the cone wave speed v_{c0} positively relates to V_i. Interestingly, the travelled distance by the cone wave, which is $v_{c0}t_r = \sqrt{\frac{m_p}{2\pi\rho_m h_m}}$ is a constant independent of V_i. As a result, when V_i is equal or lower than V_{50}, the size of IPZ or the actual deformed volume is a constant, while the strain distribution inside the IPZ positively depends on V_i. However, when V_i is higher than V_{50}, the film will rupture earlier than t_r. Thus, the size of the IPZ would decrease with increasing V_i beyond V_{50}.

We can then estimate the actual deformed volume near V_{50}, which is the traveled volume by the cone wave in t_r. By plugging in $m_p = \frac{4}{3}\rho_p \pi R^3$ (ρ_p is the projectile density and R is projectile radius), the radius of IPZ can be estimated as:

$$r_a = R + v_c t_r = R + 0.8R\sqrt{\frac{\rho_p}{\rho_m}\frac{R}{h}} \quad (5\text{-}14)$$

The ratio between the actual deformed volume and projected volume by the projectile is:

$$k = (r_a/R)^2 = (1 + 0.8\sqrt{\frac{\rho_p}{\rho_m}\frac{R}{h}})^2 \quad (5\text{-}15)$$

Eq. 5-15 provides an estimation of the maximum actual deformed volume at V_{50}. We can see that the ratio k depends on a specific geometrical factor, R/h (the ratio between projectile radius and film thickness). As a result, after being scaled by the projected volume, penetration energy still strongly depends on R and h. We use the symbol E_p^* to represent the scaled E_p values, and $E_p^* = E_p/(\rho_m h_m \pi R^2)$. Interestingly as well, Eq. 5-15 also illustrates the effect of membrane density (ρ_m) on the scale of IPZ: lower ρ_m leads to larger IPZ, or higher delocalization capability. This finding is significant in the sense that when designing armor films, a lighter-weight material with similar stiffness would be a better candidate for low velocity impact applications, as it can absorb more energy by more efficient energy delocalization. In this sense, graphene foams with high modulus and low density could find potential applications in protective structures [174-176].

To further illustrate the effect of geometrical factors on the MLG membrane as proposed in Eq. 5-15, we change the R and h separately and compare E_p^* for each system. In Fig. 5-10 (a) and (b), we see that for either monolayer graphene or tri-layer graphene, with larger R, E_p^* is higher near V_{50}. Similar effect can be seen by decreasing the h in Fig. 5-10(c). These results are consistent with the theoretical analysis that with larger R/h, the energy absorption capability of MLG film in the low V_i regime becomes better. It also shows that for very thin films relative to the size of the project, they can absorb more energy in the low velocity regime than in the high velocity regime. With increasing V_i, E_p^* first decrease, then increase. The decreasing trend is due to the shrink of actual deformed volume. When projectile velocity becomes much higher than V_{50}, when MLG

films exhibit local comminution failure mechanism, the penetration energy is governed by the comminution process and the fragments' size [177-179]. We note that this high velocity regime failure response is difficult to realize in an experimental setting, but it is important for applications such as the space exploration [165].

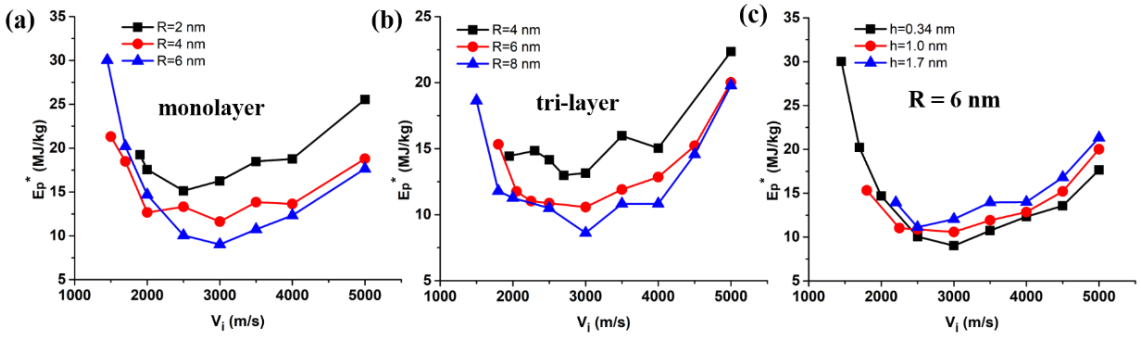

Figure 5-10. Effect of geometrical factors on the ballistic penetration energy of MLG membrane. (a) E_p^* of monolayer graphene using different sizes of projectiles. (b) E_p^* of trilayer graphene using different sizes of projectiles. (c) E_p^* of mono-, tri-, and five-layer graphene using 6 nm radius projectile.

5.3 Compressive wave effect on the ballistic resistance of multilayer graphene plate

Ballistic impact responses of ultra-thin graphene membrane have been investigated in the previous sections. Two open questions that remain unanswered are, how graphitic plates behave when they can no longer be treated as a thin membrane, and how the projectile shape influences the perforation resistance of plates of varying thickness. Macroscopically, it is already known that the penetration process and failure mechanisms become more complicated when the barriers become thicker [180, 181]. Also, the penetration process and failure mechanisms have shown to depend on the shapes and sizes of projectiles [182-186]. At smaller scales, however, there have

been far fewer studies, and the recent microscopic experiments also suggest that high-speed impact of microparticles is not simply a scaled-down version of macroscopic ballistic impact [61, 168].

In this section, we will show that beyond a critical plate thickness, a cylindrical projectile penetrates the MLG plate at a lower velocity than a spherical one. This counterintuitive phenomenon is explained by spalling-like failure for thicker plates, where the graphene layers at the bottom section undergo a wave-superposition induced failure in the cylindrical case. The spalling failure is usually observed in the dynamic failure of quasi-brittle materials such as concrete [187, 188]. Later in this section, a simple mechanics relationship for impact resistant pressure is proposed, which is originally used to describe the impact mechanics relationship for macroscopic laminates [189]. The relationship is validated for the MLG plate system studied here, and it is helpful to understand the dependence of spalling-like failure and ballistic resistance on different physical parameters.

5.3.1 Simulation setup

We generate square MLG plates composed of 3-25 layers, with the thickness ranging from 1 nm to 8.5 nm. The in-plane dimension size of the MLG plates is around 110 nm. Consistent Bernal stacking order is used for all the MLG systems [147]. In addition to spherical projectiles, we also general cylindrical projectile with a flat nose as a direct comparison and to also investigate the effect of projectile shapes on the ballistic resistance of MLG plates. Both the spherical and cylindrical projectiles studied herein compose diamond cubic lattice beads with a lattice constant of 0.72 nm. The default projectile bead mass is 192 g/mol, which gives a density of 6.8 g/cm^3. During the comparison of the two shapes of projectiles, the masses and radii of the projectiles are kept the same. In the simulations, the projectile is treated as a rigid body and the reactive forces act on the projectile as a single entity. The interactions between the projectile and graphene are

kept the same as in the previous sections. Similarly, a circular region in the center of the plate is modeled as suspended around the impact location, where the free span of the region is 100 nm in diameter. To resemble the experimental boundary condition that only the top and bottom surface is clamped, the beads outside of the circular region in the top and bottom layer are fixed, and the other beads are with without any constraints.

We also carry out finite element method (FEM) analysis to illustrate the wave propagation and stress concentration mechanisms during the impact process. Commercial software ABAQUS is used to conduct the simulations. Axisymmetric model is used to represent the axisymmetric nature of the problem as well as to save computational costs. The properties of the MLG plate is transversely isotropic. The in-plane direction is linear elastic with Young's modulus $E = 0.9\,TPa$, and the thickness direction is linear elastic with Young's modulus $E = 60\,GPa$, which are consistent with the average elastic moduli measured in CG MD simulation. The failure criteria are neglected since we aim to only show the stress wave propagation instead of capturing the failure in FEM analysis. The densities of the graphene plate and projectile are 2.2 g/cm^3 and 6.8 g/cm^3, also consistent with MD systems. The interaction between the projectile and plate is assumed to have exponential contact force varied with the gap. We set contact pressure to be zero between the projectile and the substrate when the gap is larger than 0.05 *nm*, and the repulsive force increase exponentially as they come closer, which becomes 50 *GPa* when they are in perfect contact. Our calculations have also shown that these parameters describing exponential contact force behavior have negligible influence on stress wave propagation. The impactor is initially set to be 0.1 nm above the substrate with an initial velocity of 500 m/s. Both the impactor and the multilayer graphene are represented by 4-node bilinear quadrilateral axisymmetric (CAX4R) elements in ABAQUS.

5.3.2 Dependence of impact response on projectile shape

We first consider the effects of the projectile shape on the failure mechanisms occurring in the ballistic impact of MLG plates. Snapshots of the penetration process from two CG MD simulations are shown for a spherical projectile in Fig. 5-11 (a-c) vs. a cylindrical projectile in Fig. 5-11 (d-f). Both systems comprise of a 10-layer graphene plate. The projectiles have the same total mass and the same radius of 4 nm. By visualizing the penetration process of both systems with velocities slightly above V_{50}, we show that there are mixed failure modes for both systems. Since the stresses generated in top layers are very large due to high-velocity impact, localized failure is observed in the top layers. Specifically, local fragmentation (comminution) happens in the top layers impacted by the spherical projectile (Fig. 5-11 (b)), and local plugging develops under cylindrical projectile, where pieces of circular graphene flakes under the projectile are chopped off due to large shear stresses produced around the rim of the flat-nose (Fig. 5-11 (d)). During the penetration of the remaining layers, the projectile velocity and the reactive force decrease dramatically. When the projectile reaches the bottom section of the plate, it no longer has adequate kinetic energy to induce localized failure. At this point, an IPZ develops for the bottom layers and more global deformation with petal failure is found in both cases (Fig. 5-11 (c) and (f)). This transition in the deformation mode also results in some delamination between the bottom and upper layers during failure, which further increases the dissipated energy through creating new surfaces. As a result, the orientation and surface chemistry dependent interlayer shear interactions in graphitic layers might also play a role in the ballistic performance of graphitic based barriers [126, 128, 129, 146, 190]. The different failure modes, *i.e.*, fragmentation, plugging and petal failure, have been correspondingly observed in macroscopic ballistic penetration process [181].

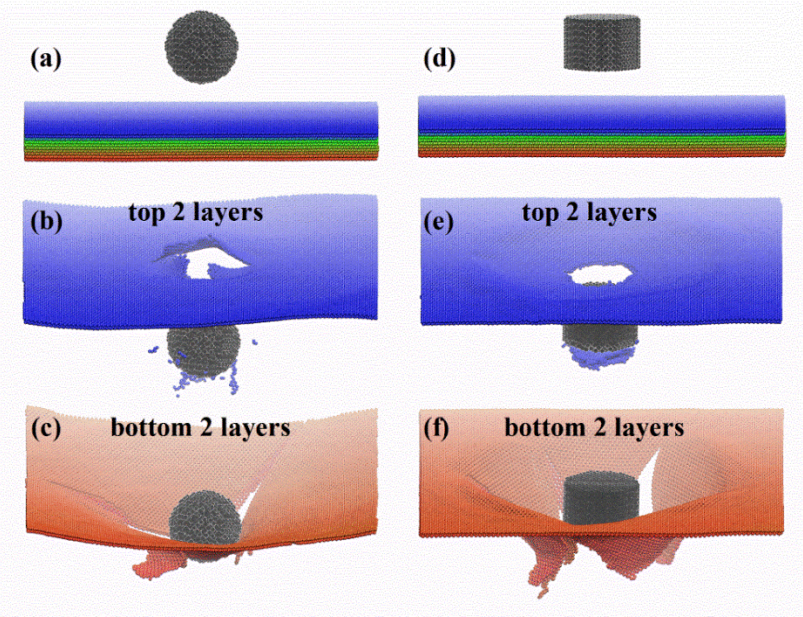

Figure 5-11. Simulation snapshots comparing the impact response of 10-layer graphene plate by a spherical vs. cylindrical projectile. For clarity, only zoomed-in square region with a length of 40 nm is shown here. The initial velocities are 3000 m/s and 4500 m/s for either case. (a) Side view of the spherical system. (b) The local fragmentation of the top two layers. (c) The petal rupture failure of the bottom two layers. (d) Side view of the cylindrical system. (e) The local plugging failure of the top two layers. (f) The local petal rupture failure of the bottom two layers.

Next, we discuss the dependence of V_{50} on the projectile shapes. We first generate graphene plates with different number of layers, and then we find out their V_{50} values by using spherical or cylindrical projectiles. To make our results more convincible, we have also used two different sizes of the projectiles, with radii to be 4 nm and 5 nm, respectively. The V_{50} results are plotted in Fig. 5-12. In general, higher velocities are required to penetrate thicker plates for the same projectile, and the V_{50} values decrease with increasing sizes of projectiles, for both spherical and cylindrical ones. The thinnest system we have tested is a 3-layer graphene plate, which is approximately 1 nm thick. Comparing to the size of the projectile, the membrane theory is still applicable to the thinnest

system since the thickness is less than 1/8 of the projectile diameter, where a previous study indicates that 0.2 is a critical ratio between plate thickness and projectile diameter, larger than which the barrier no longer behaves like a membrane [191]. For this thinnest system, the V_{50} required by a cylindrical projectile is about 50% higher than that by a spherical one. This is because a greater stress concentration is expected at the impact zone for a spherical projectile with a sharp and small contact area, which results in easier penetration. V_{50} values of varying plate thickness for the spherical case follow a linear trend. In contrast, the V_{50} values for the cylindrical case show a sigmoidal shape, and the downturn happens at the 10-layer for the 4 nm radius projectile and at the 15-layer for the 5 nm radius projectile. Beyond the downturn at the critical plate thickness, the V_{50} for cylindrical projectile becomes lower than that for spherical projectile. This crossover in V_{50} indicates that a new mechanism emerges during the ballistic impact process of the cylindrical projectile for MLG plates beyond a critical plate thickness, which significantly reduces the ballistic impact resistance of the MLG plates.

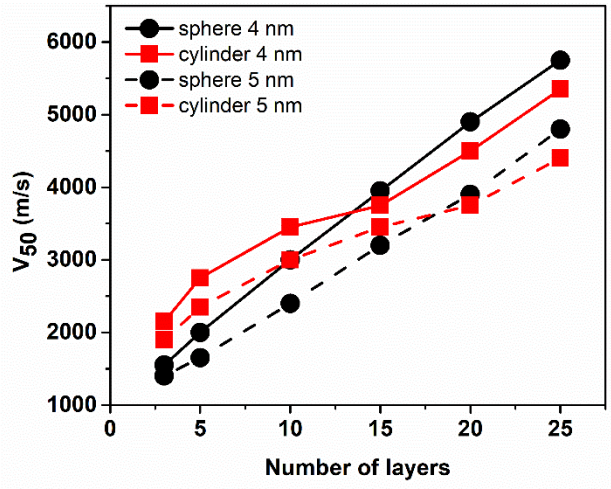

Figure 5-12. V_{50} vs. plate thickness for spherical and cylindrical projectiles with radii of 4 nm and 5nm.

To explain the change in plate ballistic resistance with respect to projectile shapes, we visualize the impact processes of the 4 nm cylindrical projectile on 15-layer graphene system. We observe an early onset of failure at the bottom section of the plate impacted by cylindrical projectile even with initial velocity V_0 below V_{50}. Fig. 5-13 shows the snapshots of the impact process with V_0 = 3600 m/s, which is lower than the V_{50} of the system (3800 m/s). After contact between the flat nose of the cylindrical projectile and the top section of the plate, the compressive wave propagates downward at a speed that is faster than the projectile velocity, as shown in Fig. 5-13 (a)(b). A rough estimation of the speed of the compressive wave is 5.2 km/s, given the elastic modulus of 60 *GPa* in the thickness direction and graphene density of 2.2 g/cm^3. The actual speed could be even higher since there exists obvious strain hardening behavior for the MLG compressive deformation in our model. When the compressive wave reaches the bottom-most layer, part of the wave gets reflected. The reflected stress wave front interacts with the remaining portion of the incident pulse in such a manner that results in failure of several layers from the bottom, as shown in Fig. 5-13 (c)-(d). Specifically, the bottom-most layer keeps intact as it is the free boundary, while several layers above it show radial cracks. Fig. 5-13 (e) shows a zoomed-in view of the cracks formed in the bottom three layers. This wave-induced dynamic fracture resembles the spalling that occurs in various materials. Spalling is a particularly well-known phenomenon for concrete, where the far-end of the structure fails by the impact of a flying object, blast, or thermal radiation such as those induced by lasers [188, 192]. This specific failure mechanism existing in the cylindrical projectile impact case facilitates the perforation of the whole plate. It explains the plate ballistic resistance change that cylindrical projectile needs lower V_{50} than a spherical one beyond a plate thickness.

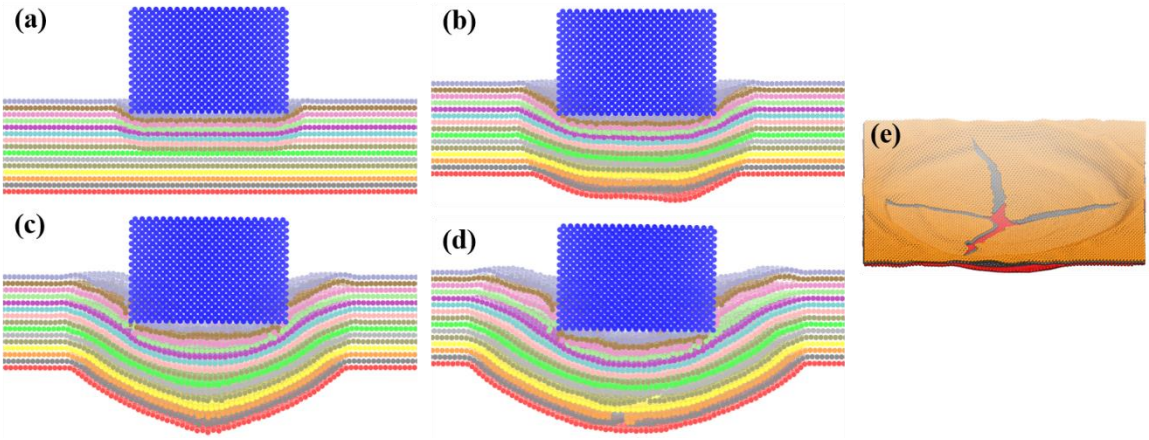

Figure 5-13. Spalling-like failure process of a 4 nm cylindrical projectile impacting on 15-layer graphene plates. Only zoomed-in center strip region with length 20 nm and width 4 nm is shown here. (a) Initiation of the compressive wave in the thickness direction. (b) The compressive wave reaches the bottom-most layer. (c) Wave reflects from the bottom-most layer. (d) Cracks develop in the bottom section of the plates. (e) Zoomed-in view of the cracks in the bottom section.

To further understand how the stress wave induces the in-plane cracks in the bottom section of the plate under cylindrical projectile impact, we carry out FEM simulations for the 15-layer MLG plate to visualize the stress wave propagation. The thickness of the plate in FEM is 5.25 nm, equaling to the MD case. However, the initial velocity of the projectile is set at 500 m/s, a lower value to ensure that failure is avoided in FEM, considering that there are no failure criteria set in the FEM. FEM simulations enable our observations on wave propagation and stress concentration in this case. From Fig. 5-14 (b) and (c), we can clearly observe the propagation of the compressive wave as represented by the stress evolution of S_{22} (normal stress in the thickness direction), where the wave front shows a planar shape. In addition, the compressive wave intensity does not show significant attenuation during propagation. At the same time, there is in-plane normal stress S_{11} developed along with S_{22} due to the Poisson effect. After the reflection of the compressive wave

at the bottom, we observe a sharp increase in S_{11} concentrated at the center of the bottom section of the plate due to stress wave superpositions, as shown in Fig. 5-14 (d). This concentration and sudden increase of S_{11} well explains the spalling failure observed in MD simulations.

On the other hand, the wave-superposition induced failure does not occur in the spherical projectile case. This is because the contact area between a spherical projectile and plate is comparatively small, and even with low V_0, the top layers would fail by fragmentation after contact with the projectile. Therefore, the intensity of the remaining compressive wave is much lower. In addition, the wave front of the compressive wave has the shape of spherical surface, which leads to faster attenuation of the compressive wave intensity by r^{-2} [193], where r is the travelling distance, as also shown in Fig. 5-14 (f) and (g). The stress level at the wave front are compared between the cylindrical and the spherical case in Fig. 5-14 (c) and (g), and the stress in the wave front is much lower in the spherical case than that in the cylindrical case. Fig. 5-14 (h) further shows that for the spherical case, the in-plane stress S_{11} only concentrates in the local area immediately below the projectile. The values for S_{11} are very small in the bottom section of the plate. This observation explains the sequential failure mechanism starting from the top and proceeding to the bottom as seen in the CG MD simulations. However, we note that the wave superposition induced failure could potentially be observed for microscale spherical projectiles, especially when the projectile is deformable, and the local curvature of the projectile nose becomes small so that the compressive waves become more concentrated with a relatively flat wave front.

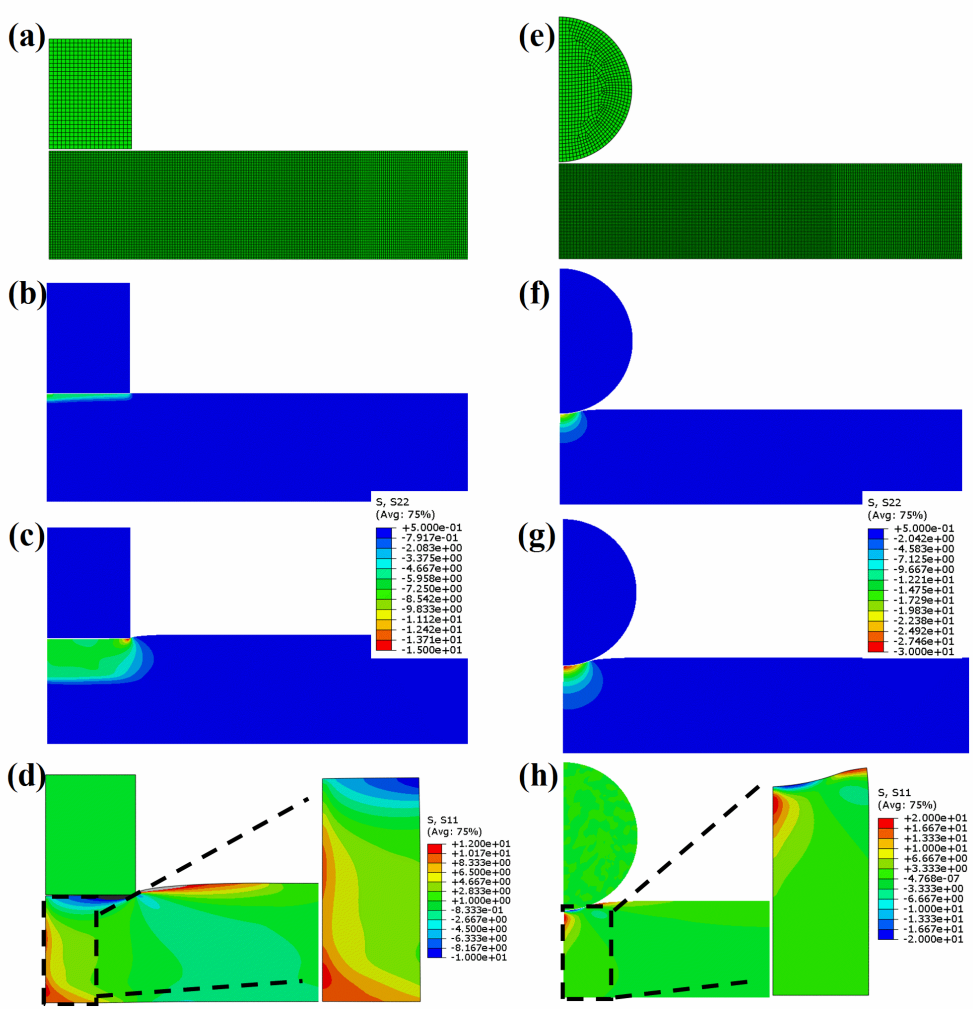

Figure 5-14. FEM simulation illustrating the wave propagation and stress concentration in both cylindrical and spherical cases. (a) Illustration of configuration and mesh of the cylindrical system. (b) Normal stress in the thickness direction (S_{22}) at the initial contact instance. (c) S_{22} and wave front. (d) In-plane normal stress (S_{11}) at the time when S_{22} wave front reflects from the bottom boundary. (e) Illustration of configuration and mesh of the spherical system. (f) S_{22} at the initial contact instance. (g) S_{22} and wave front. (h) S_{11} at the time when S_{22} wave front reflects from the bottom boundary.

5.3.3 Mechanics relationship of plate resistant pressure

To identify the physical factors that affect the spalling-like failure, we investigate the plate resistant pressure upon impact and the reactive force profile during the impact event. We know that the intensity of the compressive stress wave is the direct cause for the spalling failure observed above, and the wave intensity is positively related to the initial impact stress or reactive force on the projectile [193].

First, the reactive force profile for both shapes of projectiles and the peak reactive forces are recorded for different V_0. A common feature among the reactive force curves is a sharp initial force pulse, where reactive force first increases to its maximum value and then drops. For the spherical projectile, initially the reactive force has a gentler increase compared to the cylindrical case, and the width of the force pulse is greater. On the other hand, for the cylindrical projectile, the reactive force reaches its maximum at the instance of contact between projectile and plate. After the force pulse, the spherical case shows a more gradual decrease in the reactive force. For cylindrical case, the plate confined under the cylindrical projectile vibrates after the force pulse, and this gives rise to the subsequent force peaks for the cylindrical case, Fig. 5-15 (b). When V_0 becomes much higher than V_{50}, as in the 4000 m/s case for example, then the force pulse becomes the largest portion of force evolution. The initial peak force values are also plotted in Fig. 5-15 (c). Both spherical and cylindrical projectiles show a clear linear relationship. Also, the peak force values of the cylindrical projectile are approximately double that of the spherical projectile at the same V_0. This double relationship, arising from the effect of projectile shape, has been explained in the analysis of the mechanics of projectile perforation in metallic plates based on the different inertial forces acting normally on the projectile's nose surface [180].

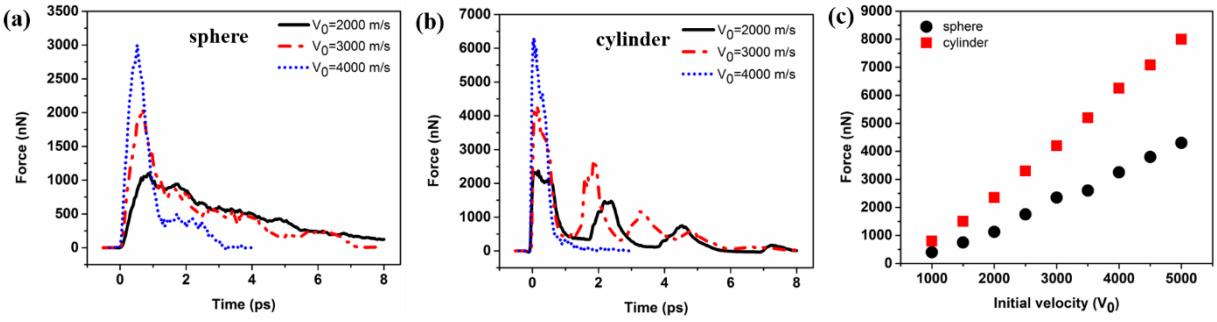

Figure 5-15. Reactive force profiles and peak forces for spherical and cylindrical projectiles at different V_0.

The linear relationship between the peak force and V_0 observed is well explained by an empirical expression developed for the resistance pressure of the fiber reinforced plastic laminate plates during ballistic impact process [189, 191, 194]:

$$\sigma = \sigma_e + \beta\sqrt{\rho_t \sigma_e} V_0 \tag{5-16}$$

where σ_e is directly related to the elastic compressive modulus of the laminates, ρ_t is the laminate density, and β is an empirical constant, and for cylindrical projectile $\beta = 2$ [191].

Eq. 5-16 indicates that the initial resistance pressure during ballistic impact depends on the plate density ρ_t, while it is independent of the projectile density ρ_p. To check whether this macroscopic relationship is valid for our small-scale system, we have changed the projectile density in the CG MD simulations by choosing different bead masses for the projectile while keeping the projectile radius (4 nm) and initial velocity (1000 m/s) constant. The results in Fig. 5-16 (a) show that the initial peak force is indeed independent of ρ_p, although the general shapes of the force pulses change accordingly with ρ_p. Next, we alter ρ_t by changing the bead mass of the CG graphene beads and alter σ_e by changing the interlayer LJ potential parameter ε_{LJ}. In our CG model, ρ_t linearly scales with graphene bead mass. Thus, we select different bead masses that give

rise to a density range of 1.1 g/cm^3 to 4.4 g/cm^3 for the plate. Fig. 6 (b) shows that the peak force varies substantially for different ρ_t. In Fig. 6 (c), the corresponding peak force is well described by the relationship $F = c_1 + c_2\sqrt{\rho_t}$, where $c_1 = \sigma_e A$, $c_2 = \beta\sqrt{\sigma_e}V_0 A$, and A is contact area, according to Eq. 5-16. Using least-square fitting method, it yields $\sigma_e = 8.75\ GPa$ and $\beta = 2.3$. σ_e agrees well with the elastic limit stress of MLG system and the β parameter is consistent with the macroscopic systems [191]. Although the quantitative relationship between σ_e and ε_{LJ} is complicated, ε_{LJ} positively alters the elastic compressive modulus of the MLG plates. We do observe a positive relationship between the peak force and ε_{LJ} in Fig. 5-16 (d), which is also consistent with Eq. 5-16.

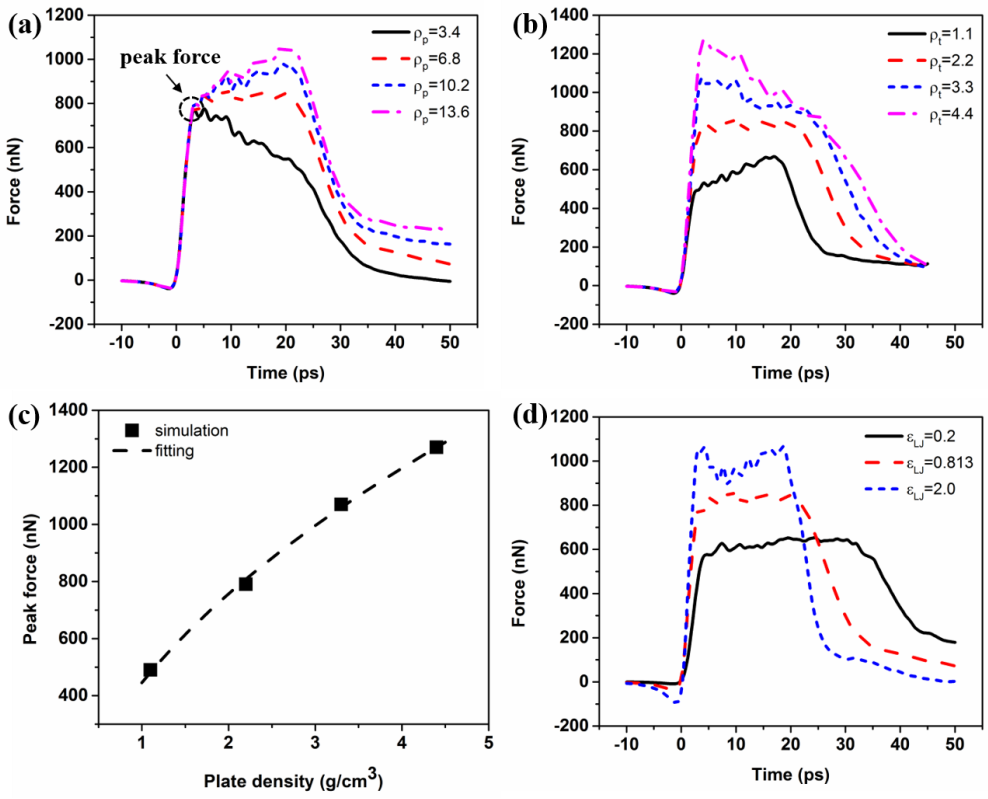

Figure 5-16. Validating the mechanics relationship using simulation results. (a) Reactive force vs. time profiles for cylindrical projectiles with different projectile densities (ρ_p). (b) Reactive force

vs. time profiles for the same cylindrical projectile with different plate densities (ρ_t). (c) Peak force vs. ρ_t results and theoretical fitting using $F = c_1 + c_2\sqrt{\rho_t}$. (d) Reactive force vs. time profiles for different interlayer interaction ε_{LJ}. All the data are from CG MD simulations with projectile initial velocity 1000 m/s. Density unit is g/cm^3, and ε_{LJ} unit is kcal/mol.

We conclude that the empirical expression Eq. 5-16 developed for macroscopic laminates is also valid for our nanoscale system when used as a simple scaling law. As a result, the intensity of stress wave linearly scales with projectile velocity, and it depends on the plate density and compressive modulus. More importantly, the relationships are independent of the system sizes across different size scales. Eq. 5-16 also provides guidelines for designing better ballistic resistant barriers as the initial resist pressure of the plate is also an index of the barriers' projectile proof capability. Higher resist pressure often indicates a better projectile proof performance. As a result, a strategy for designing better ballistic barriers is to increase the quasi-static compressive performance σ_e by enhancing the cohesive energy density, which is the interlayer interaction in the MLG case studied herein. And, increasing the barrier density ρ_t is also beneficial. Moreover, for nanocomposites-based plate, the cohesive energy at the interfaces between different components might play an even bigger role, since the energy dissipation at these interfaces is a major source for energy dissipation that influences the shock wave propagation. Introducing other energy dissipation mechanisms, such as reversible crosslinking bonds, interlayer friction and collision might also be beneficial for ballistic barriers.

In this section, we show that when the barrier no longer behaves as a membrane, a combination of failure modes emerges during the impact process, which includes plugging, petal failure, and fragmentation. In addition, the cylindrical projectile is capable of penetrating MLG plates with lower initial velocity than the spherical projectile beyond a critical plate thickness. This is because

when the plate is relatively thick, the wave superposition induced failure in the bottom section facilitates the perforation of the whole plate. This specific failure mode resembles the spalling failure usually observed in the concrete blunt-nose impact. Then, an empirical relationship for the impact pressure developed for fiber reinforced laminates is applied to the MLG plates and shows good agreement as a scaling law. Both the relationship and our simulation results indicate that stress wave intensity depends on the initial velocity, the density and compressive modulus of the plates, which are also the key factors that govern the ballistic performance of plate barrier.

5.4 Conclusion

In conclusion for this chapter, the applicability and potential of the CG model of MLG in studying the dynamic response of MLG sheets under high-speed projectile impact are demonstrated. Using the CG MD simulations, distinctive failure mechanisms are observed and the role of stress waves in the ballistic resistance of MLG sheets is analyzed. Specifically, the cone wave reflection could induce early perforation, and this phenomenon is generally applicable for finite size membranes with clamped boundary condition. Also, the clamped boundary condition would result in a deterioration in the energy absorption capability of MLG membranes when the membrane span size is smaller than the ideal size of IPZ. In addition, when MLG possess finite thickness and considerable bending stiffness, under flat-nose projectile impact, spalling-like failure could happen, which is due to the superposition of the stress waves in the thickness direction. More importantly, analytical frameworks have been developed in this chapter, which could describe the impact mechanics process of both membranes and plates. For MLG membranes, analytical models are able to describe the propagation of cone wave, the critical size relationship between membrane size and projectile size for cone wave reflection, and the maximum size of IPZ. For MLG plates, analytical relationship is developed for the resistant pressure, which depends on

the projectile velocity, the density and compressive modulus of the plates. These analytical frameworks would provide guidelines in designing the materials, geometries of ballistic barriers as well as comparing simulation and experimental results.

In this chapter, I also focused on presenting the combined computational/theoretical approach that I have used consistently during my Ph. D. study. In this context, these studies hopefully provide a way to combine both computational and theoretical methods by using MD simulations as a computational "microscope" and generalizing observations seen in this "microscope" to larger scales or different systems using theoretical analyses.

Chapter 6: Atomistic Modeling of Epoxy Resin

There are already several commercial applications implementing graphene materials for the production of high quality, multifunctional composites [6, 7, 17, 195]. Graphene and GO sheets have been incorporated into a wide range of polymer matrices, including epoxy [68, 196-202], polystyrene (PS) [203], nylon [204], and poly (methyl methacrylate) (PMMA) [205]. Among all the matrix candidates, epoxy resins are often used due to their high Young's moduli and strengths and excellent temperature resistance [59, 60]. In addition, epoxy resins are also widely applied as structural adhesives and matrix materials in fiber-reinforced composites.

The excellent thermomechanical properties of epoxy resins arise from the highly crosslinked network the resins could form. However, this crosslinked network also causes the resin to fail in a brittle manner compared to typical thermoplastics and elastomers. This performance issue has been shown to be possibly improved by dispersing micro- and nanoscale reinforcements, such as graphene and GO sheets [206-209]. Nevertheless, to further improve the mechanical performance of epoxy resin-based composites and take advantage of the synergic effect between reinforcements and matrices, a deeper understanding of the intrinsic thermomechanical properties of the epoxy resin and the influence of the crosslinked network on its fracture toughness is needed.

In this chapter, I will present the efforts in understanding the thermomechanical properties in typical types of epoxy resins and their dependence on the chemical structures. More importantly, the atomistic MD simulations are linked to the macroscopic fracture properties based on a continuum fracture mechanics model. By using this approach, this work sheds light on the molecular mechanisms that govern the fracture characteristics of epoxy resins, which is the first step to design better fracture-tolerant epoxy resin-based composites. Portions of the text and

figures within this chapter are reprinted or adapted with permission from Meng et al. Macromolecules 2016 [78].

6.1 Model development for crosslinked epoxy resin

Atomistic MD simulations have been successfully applied to predict various material properties of epoxy resins, including the glass transition temperature (T_g) [210], effects of strain rate, temperature, and crosslink degree on Young's modulus and yielding behavior [95, 211-213]. Several computational algorithms have been developed to generate reasonable crosslinked structures for investigations of their physical properties [214-217]. In this study, we choose two representative types of epoxy resins as our model system: (a) an epoxy resin commercially known as Epon 825, consisting of diglycidyl ether of bisphenol A (DGEBA) with curing agent 3,3-diaminodiphenyl sulfone (33DDS); (b) an epoxy system commercially denominated as 3501-6, mainly composed of tetraglycidyl methylenedianiline (TGMDA) with curing agent 4,4-diaminodiphenyl sulfone (44DDS). The chemical details of the two systems are shown in Fig. 6-2. The two systems are representative given that DGEBA is a bifunctional epoxy resin, while the TGDMA is a tetrafunctional epoxy resin, and the recent commercialized epoxy resins usually use them as basic resins.

For the crosslinking process, each amine group can react with two epoxide sites. the Polymatic Algorithm developed by Abbott et al. [218] is integrated with the LAMMPS package to simulate the dynamic change of the network structure. Basically, at each step, every root-mean-square (RMS) between eligible nitrogen and carbon atoms is computed, and a covalent crosslinked bond is created for the shortest distance pair if it is within the cutoff distance of bonding criteria (6 Å). After the new structure is generated, it is optimized by an energy minimization process in an MD simulation. For every 16 crosslinked bonds formed, there is also a dynamic equilibration run under

the isothermal-isobaric (NPT) ensemble for 10 ps. This equilibration is used to remove the residual stresses generated during the structure change, and 16 is chosen to optimize both computational efficiency and the necessity to equilibrate the structure. The crosslinking process proceeds until the desired crosslink degree is achieved or no more eligible nitrogen and carbon atoms fall within the cutoff distance during 10 consecutive dynamics runs under NPT ensemble, each for 10 ps. The crosslink degree is defined as the ratio between the number of crosslinked bonds created and the maximum possible number of bonds between eligible nitrogen and carbon atoms. The detailed crosslinking procedure is listed in Fig. 6-3.

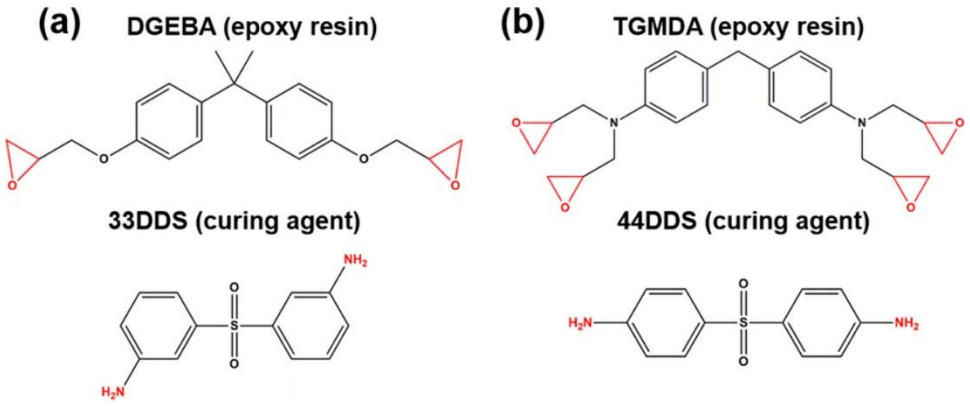

Figure 6-1. Molecular structure of the two epoxy model systems. (a) Epon 825: DGEBA/33DDS; (b) 3501-6: TGDMA/44DDS. The reaction sites of each monomer forming the crosslinked bonds are highlighted in red.

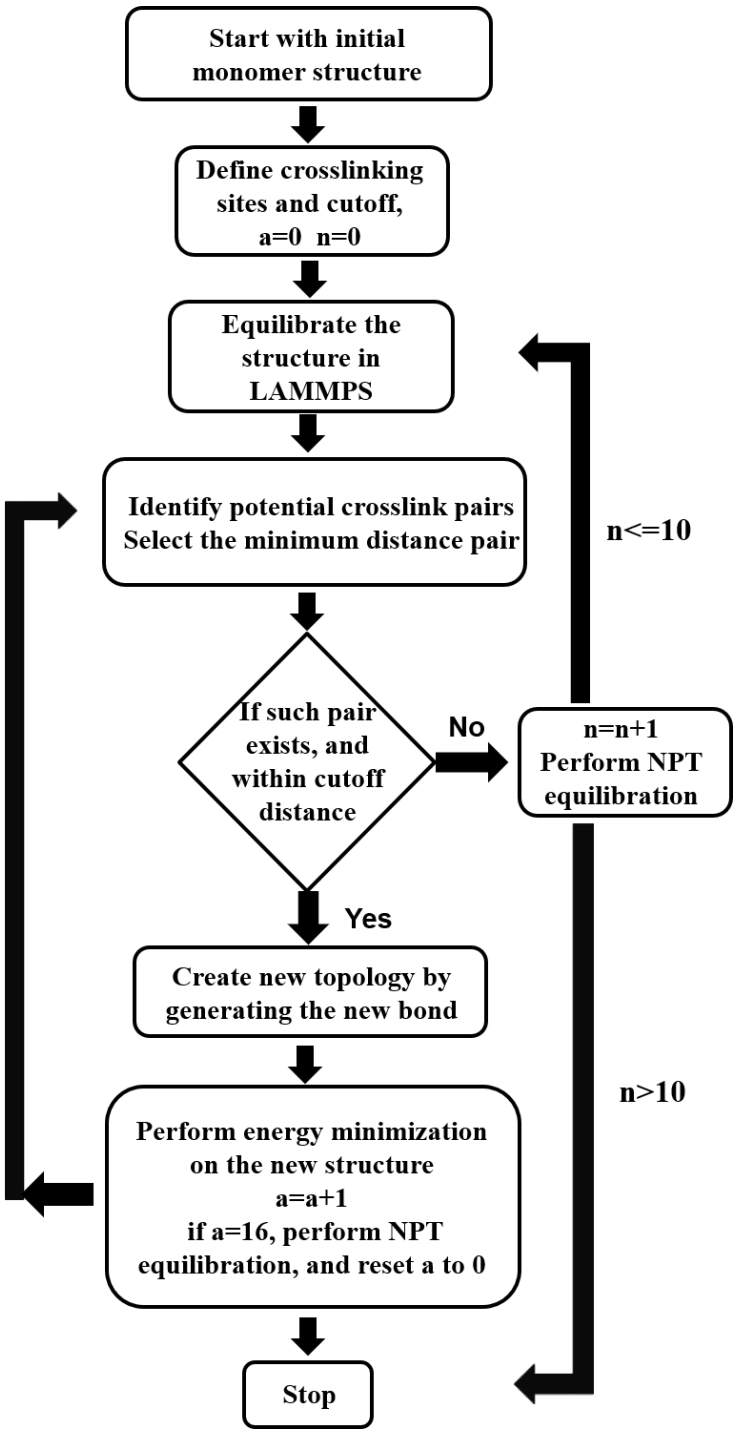

Figure 6-2. Flowchart of the simulation procedure for crosslinking process. The topology change is achieved by Polymatic [218] and the minimization and equilibration process is done in LAMMPS.

To formulate the model system for MD simulations, we first generate the monomers of epoxy resins and curing agents in Accelrys Materials Studio in their activated form (i.e. the epoxide ring is broken and the oxygen atoms form alcohol groups, leaving the carbon atoms unsaturated). Then, monomers of epoxy resins and curing agents are packed in a periodic box according to their specific ratio using the Amorphous Cell module in Materials studio with an initial density of 1 g/cm^3, slightly smaller than their targeted density. A typical Epon 825 system consists of 1024 monomers of DGEBA and 512 monomers of 33DDS (i.e. stoichiometric mixing ratio of DGEBA:33DDS=2:1) resulting in a cubic primitive cell with length ~ 9 nm, while typical 3501-6 system has 512 monomers of TGMDA and 512 monomers of curing agent 44DDS (i.e. stoichiometric mixing ratio of TGMDA:44DDS=1:1) resulting in a cubic primitive cell with length ~ 8 nm. Then, the systems with PBC are introduced into the crosslinking process as illustrated in Fig. 6-3.

By varying the curing agent/resin ratios (also referred herein as amine/epoxide ratio), we can obtain systems with different component ratios. Also, by choosing the specific structure file during the crosslinking process, we can obtain different crosslink degree structures. Taking 3501-6 as an example, we have generated systems with different crosslink degrees ranging from 65% to 95% and four different amine/epoxide ratios. Since the stoichiometric ratio of 3501-6 is 1:1, the ratio of 0.8:1 indicates an excess in epoxide groups, while the ratios of 1.5:1 and 2:1 indicate an excess of the amine groups. The different ratios are obtained by keeping the number of monomers of the epoxy (TGMDA) constant, while varying the number of amine monomers (44DDS).

6.2 Effect of resin types, crosslink degrees and component ratios on glass transition temperature

The glass transition temperature (T_g) is a key characteristic that governs the thermomechanical properties of polymeric systems. From MD simulations, the T_g of a specific polymer system can be determined from the density change as the system is cooled down [219]. However, inevitably high cooling rate is usually adopted in MD simulations. Typical cooling rate is in the order of 1 K/ps in MD simulations, about 10 orders of magnitude higher than the rates in experimental measurements. The cooling rate effects can be estimated using the Williams-Landel-Ferry (WLF) relations [220], which suggest that there is an increase of about 3K in T_g per order of magnitude increase in the cooling rate. As a result, we can still relate the T_g calibrated in MD to the actual T_g measure in experiments by subtracting 30 K. However, this is likely an upper bound to the difference as it is unclear whether the relation holds over such orders of magnitude for the cooling rate.

In this study, we first investigate the T_g of the two representative epoxy resins and then the dependence on crosslink degree and component ratio. During the T_g investigation as well as the crosslinking process, the general purpose DREIDING force field is employed [79]. A cooling rate of 0.5 K/ps is used in this study. Specifically, the system is cooled down from 600 to 250 K with a temperature step of 25 K. At each temperature step, an equilibration of 10 ps is also performed using NPT ensemble at atmospheric pressure (1 atm), and then the density of the system is calculated. After obtaining all the density values, they are plotted against their corresponding temperature. Two linear lines are fitted for both the high temperature and low temperature regime, and the interception of the two lines marks the T_g.

I will first illustrate the determination of T_g of the two representative epoxy resins at maximum crosslink degree and stoichiometric ratio. In Fig. 6-4 (a), the density vs. temperature profile is plotted for the two systems, and characteristic slope change can be clearly observed in either system. For Epon 825, T_g is predicted to be approximately 480 K, while for epoxy 3501-6, it is about 515 K. Taking into account the cooling rate effect, the MD results are in reasonable agreement with experimental results listed in the literature, reporting T_g of Epon 825 to be around 450 K [212], and 466-483 K for epoxy 3501-6 [221]. In both experiments and MD simulation, tetrafunctional epoxy resin 3501-6 achieves greater crosslink density and consequently a higher T_g compared to bifunctional epoxy resin Epon 825, corroborating the importance of resin functionality on the thermomechanical properties [222].

Next, we investigate the T_g of epoxy resins with varying crosslink degrees and component ratios. We note that increasing the crosslink degree for the same amine/epoxide ratio would always result in an increase in the crosslink density, whereas changing from the stoichiometric ratio to a different amine/epoxide ratio will lead to a lower crosslink density at similar crosslink degree. To define the crosslink density rigorously, we use the inverse of average molecular weight between crosslink sites: $D_c = n/M_t$, where D_c and M_t denote the crosslink density and the total molecular weight, respectively, and n is the number of crosslink bonds. Fig. 6-4 (b) shows the crosslink degree has a positive effect on T_g, and the positive effect becomes more pronounces as the crosslinking process proceeds. Previous studies indicate that the effect of crosslink degree on T_g can be well captured by the DiBenedetto equation [223, 224]:

$$T_g(\alpha) = \frac{\varphi\alpha}{1-(1-\varphi)\alpha}(T_{g\infty} - T_{g0}) + T_{g0} \tag{6-1}$$

where φ is an adjustable parameter between 0 and 1 and is related to the chain rigidity and functionality [225], α is the crosslink degree, and T_{g0} and $T_{g\infty}$ denote the T_g for crosslink degree

of 0% and 100%, respectively. As shown in Fig. 6-4 (b), the DiBenedetto equation fits well with both sets of data for the two representative epoxy resins, and the fitting parameter φ is obtained as 0.16 for epoxy 3501-6 and 0.31 for Epon 825. Interestingly, $\varphi = 0.31$ for Epon 825 lies in the range of values (0.22-0.38) reported in the literature [225]. In addition, the lower value for 3501-6 is consistent with experimental studies that indicate φ is inversely related to the chain rigidity and functionality [225], as tetrafunctional epoxy resin 3501-6 possess higher chain rigidity and functionality than Epon 825.

As for the amine/epoxide component ratio, our results show that the T_g is the highest at the stoichiometric ratio, which corroborate again the close relationship between the crosslink density and T_g.

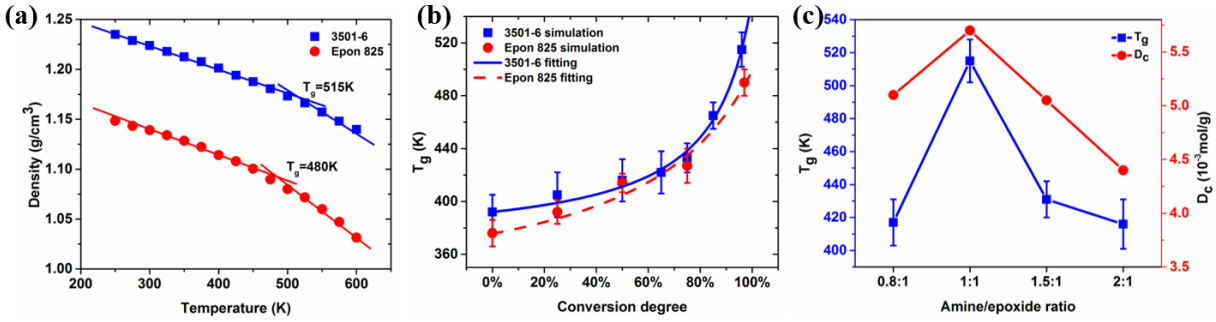

Figure 6-3. Glass transition temperature for epoxy resins with different resin types, crosslink degree (conversion degree), and component ratio (amine/epoxide ratio).

6.3 Predicting the macroscopic fracture energy from atomistic tensile simulations

6.3.1 Tensile simulation details

First, we aim to simulate the plane strain uniaxial deformation behavior and characterize the failure response of epoxy resins at the atomistic level. During large deformation, there are inevitable bond breaking events happening in the network structure of epoxy resins. To capture

the realistic bond breaking phenomenon, we adopt reactive force field (ReaxFF). After comparing different parameter sets of ReaxFF, we choose the set of ReaxFF_Mattsson [226], which has been shown to preserve the elastic and plastic responses of the epoxy resins studied here consistently with these using DREIDING force field. Specifically, Young's modulus, yield stress, and T_g results differ less than 10% between DREIDING and ReaxFF_Mattsson force fields.

During the tensile simulations, the 3D periodic epoxy structures are first relaxed using NPT at 300 K with 1 atm pressure in three dimensions. Then, the structure is uniaxially stretched up to complete failure (stress drops to 0) while the other two dimensions are held fixed to resemble the plane strain deformation state. During the tensile deformation, the temperature is controlled at 300 K by using NVT ensemble. A constant engineering strain rate of $5 \times 10^8\ s^{-1}$ is applied, and the tensile stress of the entire system of atoms in the stretching direction is computed using the virial theorem.

The stress-strain curves as well as the potential energy evolution for the two representative resins at maximum crosslink degree and stoichiometric ratio are shown in Fig. 6-5. A typical "elastic - yielding – hardening - failure" stress-strain behavior is observed for both systems, similar to the observations in other MD studies [77, 227-229]. However, higher maximum stress S_{max}, which is defined as the ultimate largest stress before final failure of the structure, and yield stress S, which is defined as the plateau stress after the curve softens or at the obvious "knee" in the stress-strain curve if the stress keeps increasing with the strain, are observed for epoxy 3501-6. In contrast, Epon 825 can be stretched more substantially before total failure, and the voids in deformed Epon 825 are more obvious than those in deformed 3501-6.

By relating the potential energy to the stress-strain curves, we find that the energy from non-bonded interactions, including both van der Waals and Coulombic interactions, increases with

strain more obviously in the small deformation regime, while the bond energy stays almost constant before the strain hardening stage, which indicates that bond stretching contributions are not significant in small global deformation. After yielding, the angle energy starts to increase due to chain alignment and reorientation with the constraints of crosslinks. During the strain hardening stage, chain extension becomes more substantial, and the potential energy from the bond and angle contributions becomes dominant compared to the non-bonded interactions, indicating more violent bond stretching events. In the final maximum stress and failure stage where stress oscillates dramatically, the bond and angle energies undergo large oscillations, indicating that covalent bonds are breaking due to chain scissions. It should be noted the non-bonded energy in the 3501-6 case starts to decrease after reaching the failure stage, which can be explained by the local relaxation after chain breaking. By comparing the potential energy evolutions of both cases, we see that Epon 825 show a later bond energy increase, as there are more room for chain arrangements during plastic deformation due to lower crosslink density.

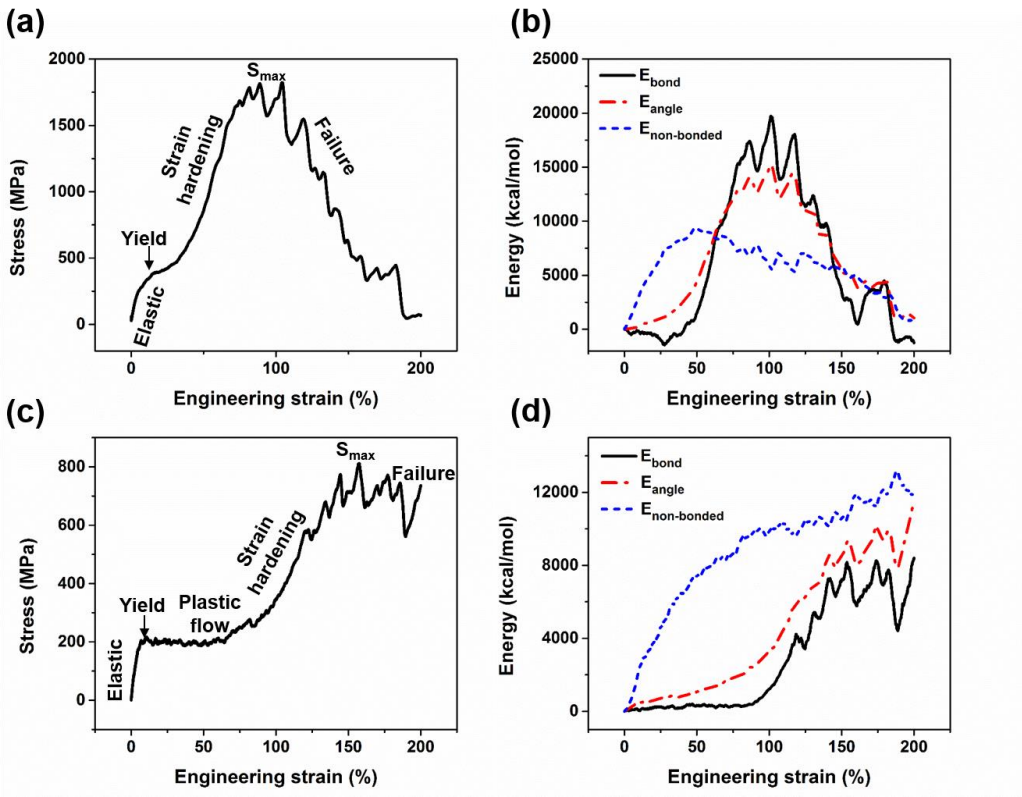

Figure 6-4. Tensile stress-strain curves and potential energy evolution during deformation. (a) Stress-strain curve for epoxy 3501-6. (b) Potential energy evolution during deformation for epoxy 3501-6. (c) Stress-strain curve for epoxy Epon 825. (d) Potential energy evolution during deformation for epoxy Epon 825.

In addition, stress-strain curves of 3501-6 epoxy systems with different crosslink degrees and component ratios are also plotted in Fig. 6-6. Consistent “elastic - yielding – hardening - failure” behavior is observed for all the cases. With increasing crosslink degree, both yield and maximum stresses increase, which is associated with decreasing failure strain or deformability. Varying the component ratio has a subtler change in the stress-strain curves, but the stoichiometric one has the highest yield stress and maximum stress while the lowest deformability.

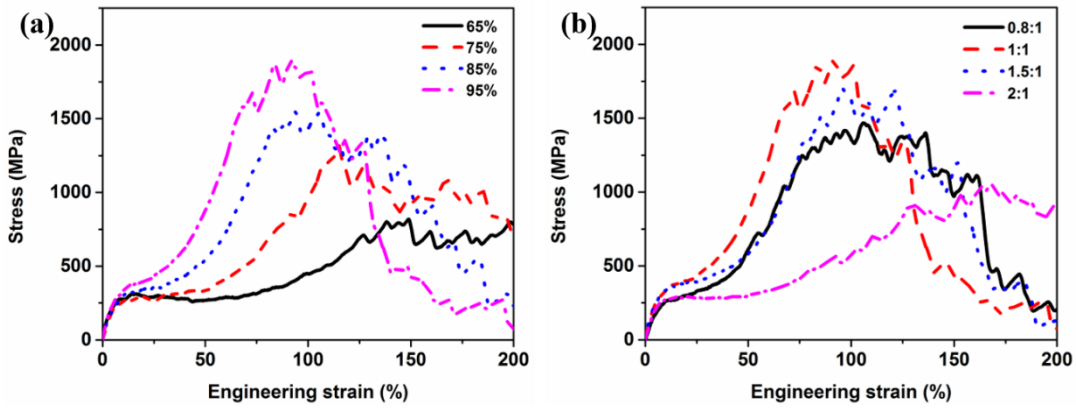

Figure 6-5. Effect of crosslink degree and component ratio on the stress-strain behavior by using epoxy 3501-6 as a model system.

To further quantify the structural changes during uniaxial tensile deformation, we use end-to-end length distribution of monomers in the crosslinked structure to describe the extension of the molecular segments. For the reorientation process, we calculate the angle between segment orientation and loading direction, and then use Herman's order parameter $f = \frac{1}{2} < 3cos^2\theta - 1 >$, with higher values indicating more monomers orienting orderly towards loading direction [230], and <> is the average sign.

Fig. 6-7 uses 3501-6 as a model system to illustrate both chain stretching and reorientation process. The results show that the segments are not effectively stretched with strain lower than 30%, similar to Fig. 6-5 (b) where bond energy does not increase. At a strain of 80%, the segments start to exhibit significant elongation as shown in Fig. 6-7 (b), corresponding to a substantial increase in bond potential energy. Fig. 6-7 (c) shows the reorientation process of segments along deformation. There is already observable reorientation happening in the system at 30% strain, indicated by the steady increase of the order parameter. The reorientation process corresponds to the increase of angle potential energy before the strain hardening regime. Finally, at a strain of

80%, segments reach the reorientation limit brought by the crosslinks and the order parameter no longer increases.

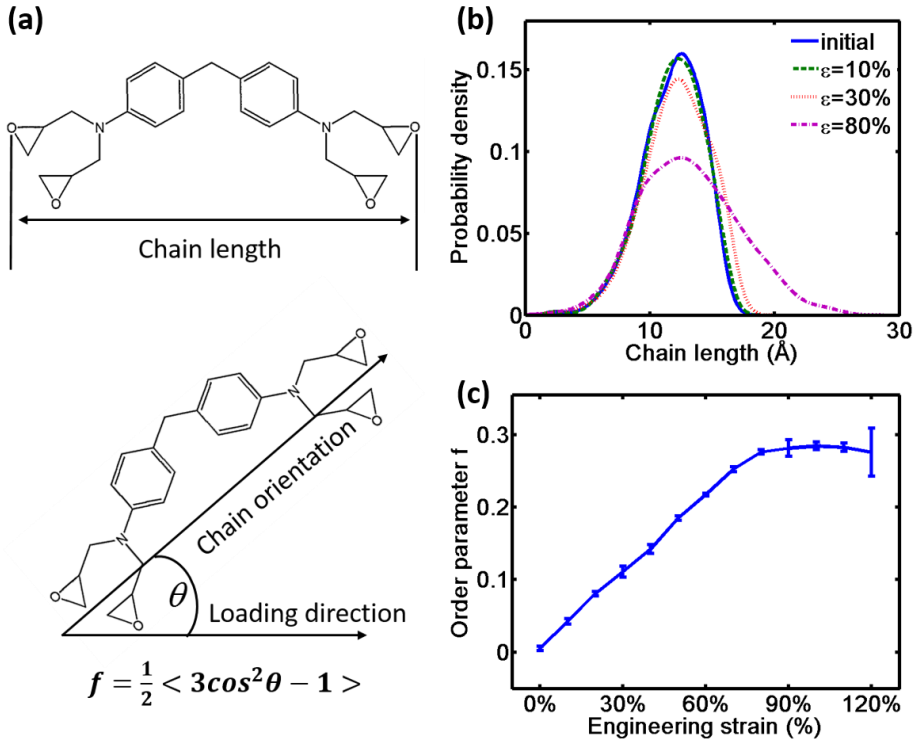

Figure 6-6. Illustration for chain stretching and reorientation during deformation. (a) Definitions of the end-to-end chain length and angle between segment orientation and loading direction for segments of monomer TGMDA in epoxy resin 3501-6. (b) End-to-end chain length distribution of monomer TGMDA at different deformation states. (c) Herman's order parameter evolution of monomer TGMDA along deformation.

At large deformation when bond and angle energies undergo large oscillations, covalent bonds start to break which leads to chain scissions. ReaxFF uses distance-dependent bond-order functions to represent the states of chemical bonds. The minimum bond-order value used in ReaxFF_Mattsson to identify chemical bonds between pairs of atoms is 0.1, lower than which the bond is treated as broken. Thus, we can obtain the number of bonds evolution during deformation.

Fig. 6-8 shows the total number of bonds vs. strain for the 3501-6 system at the maximum crosslink degree and stoichiometric ratio. We observe that the total number of bonds does not decrease till reaching strain of 75%, which corresponds to the end of the strain hardening regime. This observation also indicates that the scissions of the chains happen in large scale when the stress approaches its maximum level. In the final failure stage, the total number of bonds saturates to a stable level. In a similar way, we calculate the evolution of the number of bonds for epoxy resins with different crosslink degrees as shown in Fig. 6-6(a). The results show that with increasing crosslink degree, the bonds start to break at lower strain, which is consistent with the stress-strain curves that shown stress maxima at lower strains for greater crosslink degrees. In addition, the total number of bonds broken after total failure increases with greater crosslink degree, Fig. 6-8(b). This can be explained by the larger number of crosslink bonds of higher crosslink degree structures.

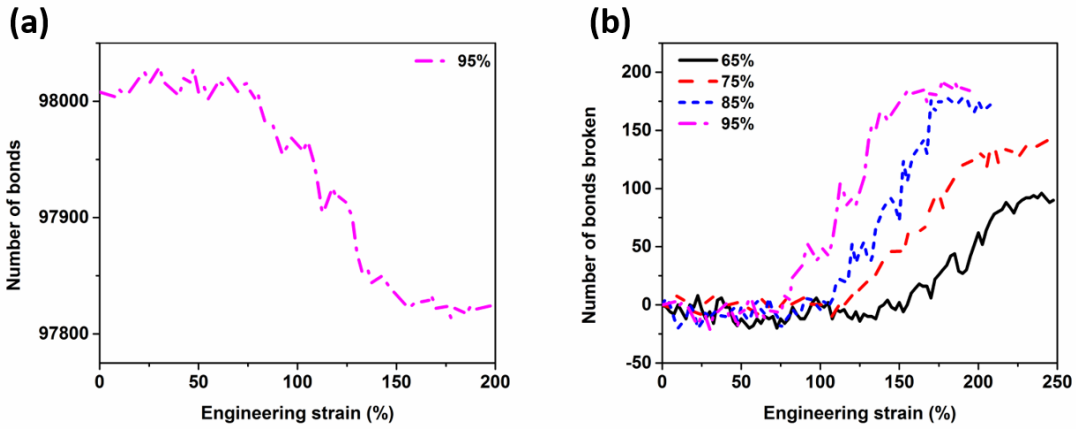

Figure 6-7. Evolution of number of bonds in the network structure during tensile deformation. (a) Epoxy 3501-6 with maximum crosslink degree and stoichiometric ratio. (b) Number of bonds broken during deformation for 3501-6 system with different crosslink degrees.

Along with chain reorientation and the subsequent bond breaking events, there are obvious voids developing during the plane strain uniaxial deformation, as shown in Fig. 6-9(a) for the two

representative epoxy resins at maximum crosslink degree and stoichiometric ratio. This void formation process resembles the fibril formation process typically observed in the crazing zone of thermoplastics [231-235]. The only difference is that the crosslink sites constraint the shape and size of the voids and prevent them from forming large parallel fibrils. To quantify the void size, we use Zeo++ software that is available online (http://www.maciejharanczyk.info/Zeopp/), which is based on Voronoi cell decomposition. Specifically, for a given spherical probe, Zeo++ can analyze the void space accessible to this probe and the void distribution using Monte Carlo sampling approach. Using this software, we calculate the void distribution across the entire stress-strain response and find the void sizes increase along the deformation and reach a plateau near the maximum stress regime. This trend is consistent with a recent study that indicates a steady increase of void size in the strain hardening regime and saturation towards the maximum stress regime [228]. So, we use the void distribution in the maximum stress regime to calibrate the average void size, and we use the mean void diameter (MVD) to represent the average size. The void distribution is provided in histogram form, as shown in Fig. 6-9(b). MVD is calculated by performing numerical integration on the distribution histogram.

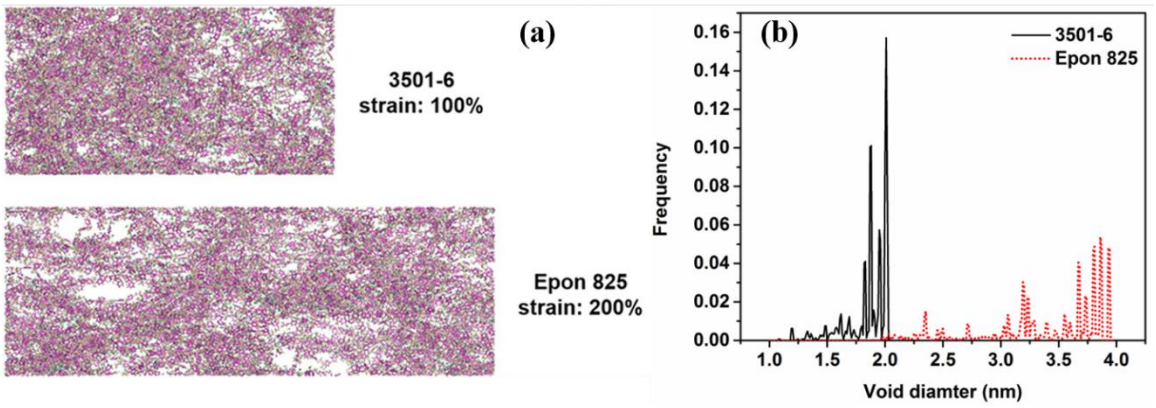

Figure 6-8. Void formation process of the two representative epoxy resins at large deformation and the corresponding void distribution histogram.

In summary, this sub-section lists all the details for the uniaxial deformation of epoxy resins. However, we still need a scale bridging method to link the nanoscale level deformation to the macroscopic fracture energy of epoxy resin in order to guide intelligent design of new materials. In next section, I will show that a continuum fracture mechanics model developed for glassy polymers could serve as a bridging method as well as shed light on the molecular level mechanisms and factors that influence the macroscopic fracture properties.

6.3.2 Fracture energy prediction using a continuum mechanics model

Varies fracture mechanics models have been proposed for the crazing zone that is commonly observed in glassy polymers [231-235]. These models share several basic simplified assumptions. First, the fracture energy is mainly contributed by the plastic deformation energy dissipated in the process zone (i.e. crazing zone) ahead of the major crack tip. Second, the plastic deformation energy can be estimated as the work done by the yield stress to propagate a strip-shape process zone. Third, the size of the process zone is related to the fibril formation state ahead of the crack tip. Schematics illustrating these assumptions are shown in Fig. 6-10.

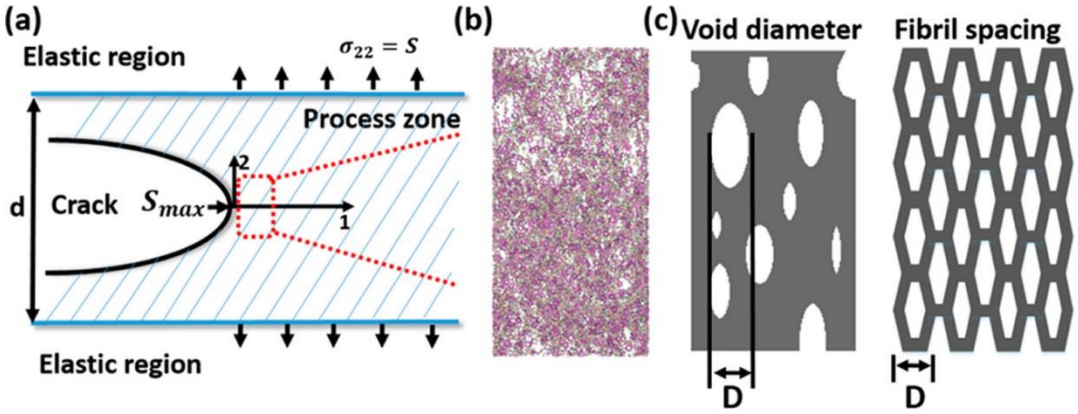

Figure 6-9. Schematic showing the assumptions made in the continuum fracture mechanics models. (a) Schematic diagram showing the strip-shape process zone. (b) An epoxy system in a typical MD simulation at the maximum stress state, showing void formation, which represents the deformation

state of epoxy near the crack tip. (c) Schematic illustrating the void diameter in the epoxy system compared to the fibril spacing in linear chain polymer systems.

Specifically, the mechanics model proposed by Brown based on the generic fibril/cross-tie microstructure shows that the fracture energy can be predicted as [232]:

$$G_c = 2\pi D \frac{S_{max}^2}{S}\left(1 - \frac{1}{\lambda}\right)\sqrt{\frac{C_{22}}{C_{66}}} \tag{6-2}$$

where C_{22} is the average elastic tensile modulus in the X2 direction (*i.e.* stretching direction in Fig. 6-10(a)), C_{66} is the average in-plane shear modulus of the process zone. S and S_{max} represent the yield stress and maximum stress of the defect-free material, respectively. λ is the average stretch ratio of the process zone, and D denotes the fibril spacing, *i.e.* the distance between adjacent fibrils.

We note that Eq. 6-2 is a simplified expression of the original form, which is adopted by all the versions of mechanics models. The simplification is done based on the assumption that the elastic constant in the stretching direction is much larger than those in other directions. We have verified that this assumption holds for the epoxy resin structure studied here as in the deformed state after chain reorientation, the structure is highly anisotropy.

Rottler and coworkers have previously shown that the key parameters in Eq. 6-2 can be determined in sequence in one typical MD run [77]. Specifically, S and S_{max} can be determined from the stress-strain curve obtained from MD uniaxial tensile simulation. As C_{22}, C_{66}, and λ represent the average property of the process zone, and the stress state in the process zone ranges from yielding (process zone boundary) to maximum stress state at the crack tip, they are measured in the strain hardening state, which is the middle stage between yielding and maximum stress. D denotes the stable fibril spacing, and it is measured at the maximum stress state, when D saturates.

Previous experimental investigations have shown that microscopically, a process zone exits even in the most tightly crosslinked epoxies [236]. The process zones at the crack tip of polymer glasses and epoxy resins both extend transversely to the loading direction and share the same strip shape [237]. In addition, at the atomistic level, the tensile deformation mechanisms of epoxy resemble those of polymer glasses to a much extent, which both include elastic, yield, plastic flow, strain hardening and void formation followed by failure, as shown in recent studies [77, 227]. As a result, the three basic assumptions for the continuum mechanics model still hold for the epoxy resin case. For instance, the fracture energy is mainly dissipated in the plastic deformation in the process zone, and the process zone can be approximated as a strip-shape zone [238-240]. Therefore, we can apply Eq. 6-2 to estimate the macroscopic fracture energy of epoxy resins from the parameters obtained from atomistic tensile simulations.

We calculate the MVD at strain levels in the maximum stress regime and determine the average value as the parameter D. We choose the stretch ratio λ at the strain level where the stress is equal to $(S + S_{max})/2$. The elastic constants (C_{22} and C_{66}) are calculated at different strain levels inside the strain hardening stage. We find that C_{22} and C_{66} gradually increase with strain in the hardening stage. However, the parameter $\sqrt{C_{22}/C_{66}}$ is independent of the strain in this stage and the standard deviation is only within 10% for the epoxy systems studied herein. Although the choice of stretch ratio λ is empirical in this study, the consistent definition for all cases enables this parameter λ to represent the deformability consistently for different epoxy systems. The parameter D originally quantifies the average fibril spacing in the maximally deformed linear chain polymer glasses. Since the crosslinks prevent the elliptical voids from becoming interpenetrated [241], we take the MVD measured perpendicularly to the stretching direction as a more representative measure. Moreover, the MVD is similar to the fibril spacing as they both

characterize the deformed conditions of the maximum stress state near the crack tip, as shown in Fig. 6-10(c).

By carrying out sensitivity analysis, our results suggest that the parameter $\sqrt{C_{22}/C_{66}}$ exhibits a variation that is less than 20% for different epoxy chemistries, indicating that it plays a minor role in Eq. 6-2. Consequently, we can conclude that the key parameters governing the fracture toughness for epoxy resins are D, average stretch ratio λ, and $\frac{S_{max}^2}{S}$. We further find that D and λ mainly represent the post-yield deformability, as larger D and λ indicate that the crosslinked structure can be stretched more, and the cavitation process is more pronounced before total failure. Dispersing nano- and micro- elastomeric particles will also give rise to stronger cavitation processes that lead to greater energy dissipation near the crack tip [242, 243]. On the other hand, $\frac{S_{max}^2}{S}$ quantifies the structural rigidity given that a more rigid structure results in higher value of $\frac{S_{max}^2}{S}$. We find that epoxy resins with lower crosslink densities possess larger D and λ, as with lower constraint of the crosslinks, the deformability and cavitation process is greater. However, they have lower values of $\frac{S_{max}^2}{S}$, because the crosslinks positively contribute to the maximum stress, or the structural rigidity. As a result, we would anticipate a competing relationship between the post-yield deformability and structural rigidity as the crosslink density increases.

After justifying the applicability of the model and the calibration of the parameters, we first compare the fracture energies of the two representative epoxy resins at maximum crosslink degree and stoichiometric ratio. The parameters determined from their corresponding tensile simulations are listed in Table 6-1. Using Eq. 6-2, we predict the fracture energy for Epon 825 to be approximately $139 \pm 10\ \mathrm{J}/m^2$, which is within the range of experimental values for similar DGEBA based neat resins [244, 245]. The prediction for 3501-6 is $109 \pm 8\ \mathrm{J}/m^2$, which is also

in reasonable agreement with the manufacturer reported value of $128\ \mathrm{J}/m^2$ (~12% difference). In addition, the overall trend that the fracture energies decrease with increasing resin functionality is consistent with the experimental observations [245].

Table 6-1. Parameters Obtained from MD Simulations to Calculate Fracture Energy for Both Epon 825 and 3501-6.

	EPON 825	**3501-6**
$\boldsymbol{S}$	$205 \pm 10\ MPa$	$360 \pm 10\ MPa$
$\boldsymbol{S_{max}}$	$890 \pm 22\ MPa$	$1880 \pm 30\ MPa$
$\boldsymbol{\lambda}$	2.1 ± 0.02	1.55 ± 0.02
$\boldsymbol{D}$	$3.37 \pm 0.12\ nm$	$1.84 \pm 0.08\ nm$
$\sqrt{\boldsymbol{C_{22}/C_{66}}}$	3.22 ± 0.1	2.68 ± 0.06

Varying crosslink degree directly changes the crosslink density, and it would have a more complex influence on the predicted fracture energy. Previous sections have shown that T_g always increases with increasing crosslink degree, since the crosslinks contract the structure and decrease the segment mobility. However, the investigations by Marks et al. suggest that the fracture toughness of amine-cured epoxy resin exhibits a maximum fracture energy at crosslink degree between 65% and 95%, depending on the type of curing agent [225]. Following the same procedure, we predict the fracture energies of epoxy 3501-6 at different crosslink degree. As shown in Fig. 6-6(a), increasing the crosslink degree is associated with an increase in both yield and maximum stress, but a decrease in the post-yield deformability, indicated by the decrease in D and λ. As a result, the competing factors give rise to a maximum fracture energy at moderate conversion degree (75% for 3501-6 studied here), as shown in Fig. 6-11(a). This observation also implies that

although higher crosslink degree can enhance many thermomechanical properties, such as T_g and modulus, it may not necessarily increase the fracture toughness. The hallmark tradeoff between strength and toughness is thus a characteristic of epoxy systems [225].

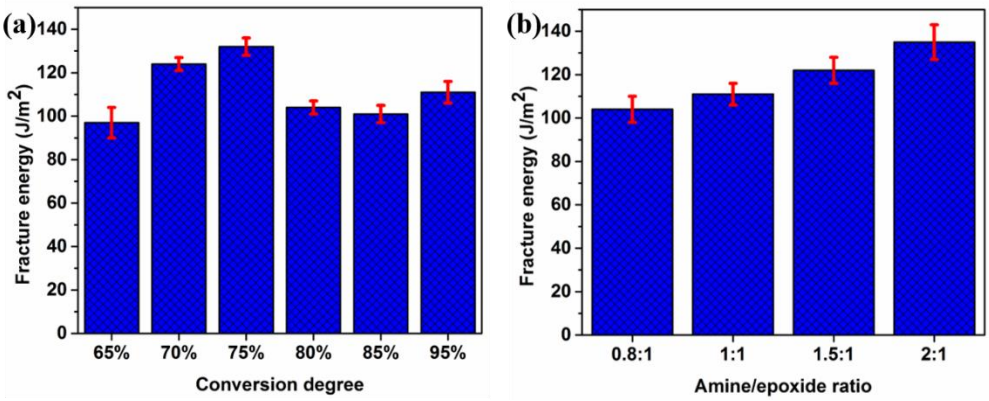

Figure 6-10. Predicted fracture energy for resin 3501-6 with different crosslink degrees and component ratios.

Next, we investigate the effect of component ratio on the fracture energy, and the results reveal that the fracture energy of the epoxy increase with increasing ratio of curing agent. This is consistent with the trend observed in experiments, in which the fracture energy of a tetrafunctional epoxy resin similar to 3501-6 increases with increasing amount of amine curing agent [246]. Although T_g maximizes for the stoichiometric ratio case, both our prediction and experiments show that the fracture toughness of typical epoxy system can be enhanced by increasing the initial curing agent ratio beyond stoichiometric ratio. The agreement between our prediction and experiments further show the capability of this scale bridging method with atomistic simulations to guide future molecular-level design of epoxy resins with optimized fracture and thermomechanical properties.

6.4 Conclusion

In conclusion for this chapter, a computational method to generate the crosslinked structure of epoxy resins is developed. It is very flexible given that resin types, crosslink degrees, and the component ratios between initial resin and curing agent molecules can all be changed. Then, this work shows that DREIDING force field adequately captures the T_g differences resulting from epoxy types, crosslink degrees and component ratios, as also verified by analytical DiBenedetto equation and experimental results for the two epoxy systems considered herein. In addition, an existing parameter set of ReaxFF not only agrees with DREIDING force field in small deformation but also yields reasonable failure behavior of epoxies at molecular level. The plastic deformation and cavitation process observed and characterized from reactive MD simulations provide further evidence for the plastic deformations at the crack tip region that contribute to the fracture toughness during crack propagation events.

Furthermore, I present here a multiscale framework to link the deformations observed at the molecular scale with the macroscopic fracture properties by adopting a continuum mechanics model. With this framework, the fracture energy of epoxy resins is shown to be closely related to their molecular architectures and two competing factors, the structural rigidity and post-yield deformability, which influence the process zone ahead of the crack tip simultaneously. Specifically, fracture energy is predicted to decrease with increasing functionality of the epoxy resins. For the tetrafunctional epoxy resins studied here, the fracture energy reaches peak value at moderate crosslink degree, and it can be enhanced by adding more curing agents. The proposed framework show promise in accelerating the material-by-design process for thermosets by incorporating data from atomistic simulations.

Chapter 7: Failure Mechanisms of Nanocomposites and Composites

In this chapter, my graduate work culminates in utilizing the CG models and analytical scale-bridging methods to investigate the failure mechanisms of nanocomposites and composites. Specifically, in the first section, I will present a CG MD study of the interfacial failure mechanisms of nacre-inspired nanocomposites with MLG domains embedded in a PMMA matrix. I collaborated with my colleagues Wenjie Xia, Jake Song, and Chen Shao on this work. The simulations reveal two distinct deformation and failure mechanisms that greatly influence the energy dissipation of the system: pull-out failure and yielding failure, with the latter one dissipating significantly more energy during deformation. The continuum fiber pull-out model is applied to analyze the mechanics problem. This model reveals that there exists a critical number of layers, beyond which the failure mode changes from yielding to pull-out. This combined computational and analytical framework provides effective strategies to design graphene/polymer layered nanocomposites with optimal toughness. In the second section, I will present our effort to bridge the thermomechanical properties of epoxy resins characterized in MD simulations to the interphase properties between carbon fiber and resin matrix with an analytical gradient model. By collaborating with engineers at Ford (Qingping Sun, Guowei Zhou, Dr. Xuming Su etc.), we further integrate the interphase property with representative volume element (RVE) modeling to investigate the failure mechanisms and behaviors of carbon fiber reinforced epoxy resin composites. The nanoscale interphase region is shown to significantly influence the composite non-linear and failure response. In the third section, this multiscale computational model is utilized to characterize the failure mechanisms of the composites, which are also validated with the experimental analysis. Portions of the text and figures within this chapter are reprinted or adapted

with permission from Xia et al. Molecular Systems Design & Engineering 2016 [39] and Sun et al. Composite Structures 2018 [247].

7.1 Two failure mechanisms in nacre-inspired nanocomposite

As discussed in Chapter 1, nacre-inspired nanocomposites with layered nanostructure are advantageous in many ways, such as transfer of shear stresses [248], confinement of cracks upon reaching the polymer matrix [249], resistance to shear from frictional asperities [250], and pull-out mechanism of the crystalline platelets. These combined effects preserve the strength of the stiff crystalline plates, while having toughness that is orders of magnitude higher than its constituents. Taking advantage of the developed CG model of MLG [127] and PMMA [94] in our group, we design a nacre-inspired layered architecture of MLG-PMMA nanocomposites and investigate the interfacial mechanics between staggered graphene layers and polymer layers. Using CG MD simulations, we first characterize the interfacial behaviors of the designed systems as well as identify critical sizes of MLG that govern deformational behaviors. We then discuss the simulation results in the context of the fiber pull-out continuum mechanics model and generalize the results to effective optimization strategies to design mechanically robust nacre-inspired nanocomposite systems.

7.1.1 Computational model

The nacre-inspired nanocomposite consists of a layered nanostructure of CG PMMA and MLG phases, as shown in Fig. 7-1. In the CG model of PMMA, two-bead mapping scheme for each monomer is adopted, with one bead representing the backbone group and the second bead representing the sidechain methyl group. The bonded interactions, including bond, angle and dihedral potentials, are parametrized using the inverse Boltzmann method (IBM) [105] to match the probability distributions. The non-bonded interactions take the form of a 12-6 LJ potential, and

are parametrized to capture the bulk density, T_g, and elastic modulus. Details procedures for developing the CG modeling can be found in Hsu et al. [94, 119]. The simulated system consists of one PMMA layer and one MLG layer, which constitute an RVE in the microscopic layered nanocomposites, as illustrated in Fig. 7-1(a). The PMMA layer has a thickness of approximately 20 nm, which consists of a block of polymer chains with a chain length of 100 monomers per chain. The MLG layer consists of varying number of layers N with two sheets per layer in a staggered architecture, with an overlap ratio of 50% and an overlap length $L_o \approx 12.5\, nm$. The total length L of the system is about 50 nm in the y direction. The width of the system is about 10 nm in the x direction. Periodic boundary conditions (PBC) are applied in the x and z directions and non-PBC are applied in the y direction. We adopt 12-6 LJ potential to represent the non-bonded interaction between graphene and polymer with $\varepsilon_{gp} = 0.8\, kcal/mol$ and $\sigma_{gp} = 4.5$ Å, which results in an interfacial energy of $\sim 0.15\, \mathrm{J}m^{-2}$, similar to experimentally reported values. We note that changing the value of ε_{gp} would effectively change the interfacial interaction as well as the interfacial shear mechanics.

The system is first equilibrated in NVT ensemble at 300 K for 2 ns. Then, we use steered molecular dynamics (SMD) simulation to perform MLG pulling out deformation. Specifically, one edge of the MLG layer is pulled by applying a force generated by a stiff harmonic spring, and we use pulling velocity of $0.1\, \text{Å}/\text{ps}$. All SMD simulations are carried out at a temperature of 300 K, and therefore the PMMA layer is below its T_g, which is around 380 K as measured from simulations. During the MLG pull-out deformation, the deformation of PMMA layer in y direction is prevented by a repulsive wall in the x-z plane. This action is reasonable given that the force contribution from the deformation of the polymer layer is negligible compared to the contribution of graphene-polymer interface. However, when the graphene-polymer interfacial interaction is

very strong or when the temperature is close to or above the T_g, this assumption needs to be revisited accordingly.

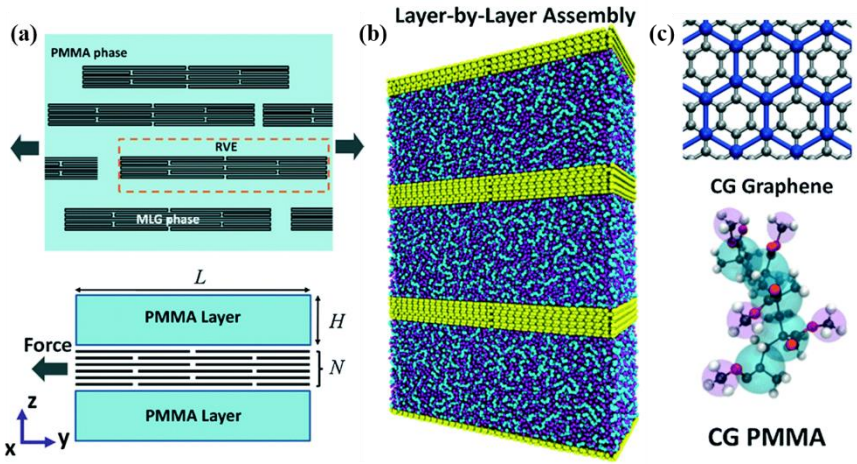

Figure 7-1. Computational design of the nacre-inspired nanocomposites with MLG and PMMA. (a) Illustration of the microscopic picture of the nanocomposite system under loading. (b) Layer-by-Layer assembly of MLG and PMMA nanocomposites. Note that our simulated system only consists one layer of MLG and PMMA. (c) All-atomistic to coarse-grained mapping schemes for graphene and PMMA.

7.1.2 Two failure mechanisms and continuum fiber pull-out model

Our simulations reveal two different modes of failure: a clean pull-out mode which corresponds to MLG-PMMA interfacial failure in the case of thicker MLG assemblies, and a yielding model which occurs within the MLG through the internal sliding of staggered graphene sheets, as shown in Fig. 7-2. Furthermore, we observe that for a given interfacial interaction strength ε_{gp} and embedded length L, the failure mode of MLG changes from yielding to pull-out as the number of layers N increases to a critical value N_{cr}. The yielding failure mode involves the sliding of graphene surfaces due to the staggered architecture of the MLG, and it can dissipate tremendous amount of energy upon deformation. The transition in failure resembles micro- or

macroscopic fiber pull-out test as either the fiber breaks during pull-out or the fiber is completed pulled out [251]. Next, we aim to predict the failure mode transition as a function of N and other physical parameters using continuum theory.

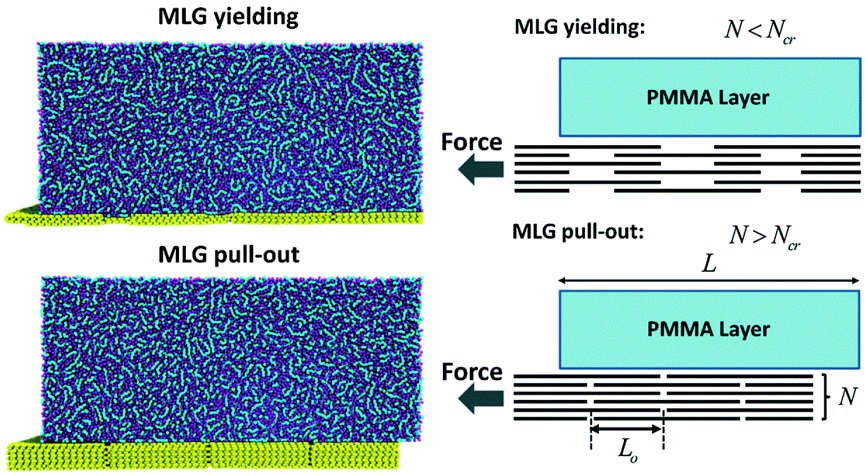

Figure 7-2. Snapshots of the SMD pulling simulations for the two failure mechanisms and corresponding schematics.

The continuum fiber pull-out model can be written as [252]:

$$F = F_{\infty}\tanh(\alpha L) \tag{7-1}$$

where $\alpha = \sqrt{K/E_m h}$ is a length scale parameter governing the shear stress transfer along the MLG-PMMA interface, E_m and h are the modulus and thickness of MLG, respectively, K is the interfacial shear stiffness among MLG-PMMA interface, $F_{\infty} = \tau_s/\alpha$ is the maximum pull-out force per unit width at infinitely long MLG sheets, and τ_s is the interfacial shear strength.

By knowing the Young's modulus E_m and tensile strength σ_m of staggered MLG [74] and K and τ_s by performing interlayer shear test between a continuum graphene sheet on top of polymer layer [39], the critical condition for differentiating failure mode can be determined by solving the force balance equation:

$$2F_{\infty}\tanh(\alpha L) = \sigma_m h \quad (7\text{-}2)$$

where factor 2 is needed to account for the upper and lower interfaces given the periodic structure.

Numerically solving the above equation yields the critical number of layers N_{cr} of graphene that governs the mode of failure. For the specific system studied here ($\varepsilon_{gp} = 0.8\ kcal/mol$ and $L = 50\ nm$), the theoretical value of N_{cr} is 4. This prediction is in excellent agreement with our simulations results, where $N = 4$ is still MLG yielding failure and $N = 5$ gives rise to MLG pull-out. Eq. 7-2 also implies that in addition to N, τ_s and L are also key parameters that govern the modes of the failure.

Next, we use the continuum model Eq. 7-2 to extend our analysis to arbitrary values of τ_s (which is directly related to ε_{gp}) and L to understand how N_{cr} depends on these parameters. With the results we have on the dependence of K and τ_s on ε_{gp}, we can predict the specific N_{cr} values for different L and ε_{gp}, and the results are shown in Fig. 7-3. The value of N_{cr} increases initially with the length L, and then saturates at very large $L{\sim}400\ nm$. This saturation effect at large L is due to the non-uniform shear stress distribution along the MLG-PMMA interface as predicted by the continuum model. Increasing ε_{gp} will increase N_{cr} for a given value of L. However, the length scale where N_{cr} saturates is almost invariant with ε_{gp}. As a result, Eq. 7-2 along with Fig. 7-3 provide guidelines to tune key parameters to design both the geometrical factors and interfacial interactions of the nanocomposite system.

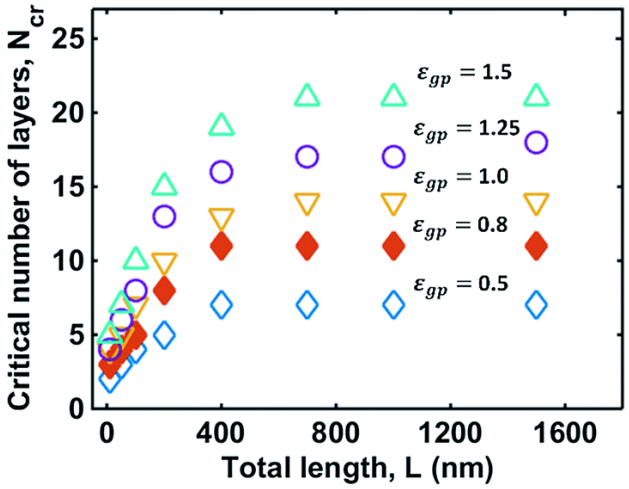

Figure 7-3. Theoretical prediction of the critical number of layers of graphene as a function of total MLG length for different interfacial interaction strength. The solid diamond data highlights the specific interfacial interaction strength that is studied in our simulations.

In summary, we have investigated interfacial mechanical behaviors of nacre-inspired MLG-PMMA layered nanocomposites systems by performing pull-out simulations using CG MD approach. Our simulation results illustrate two different deformation and failure mechanisms, which influence the toughness and energy dissipation capability of the system: pull-out failure, which occurs along the MLG-PMMA interface, and yielding failure, which occur along MLG-PMMA interface. We then apply a continuum mechanics model developed for fiber pull-out problem to the systems studied here. The predictions from the continuum model agree very well with the simulation results. The analytical relationship also indicates that increasing the system length and the interfacial interaction strength will increase the critical number of layers of graphene that induces failure mode change. Our prediction of failure modes provides ideal design strategies for MLG and polymer-based nanocomposites.

7.2 Effect of interphase on the mechanical properties of carbon fiber reinforced epoxy resin composites

Carbon fiber reinforced polymer (CFRP) composites have numerous applications in lightweight structures in the aerospace and automotive industry due to their excellent strength and stiffness while low density. The fast-expanding demand for these composites requires efficient material characterization techniques to predict the mechanical properties of them, most notably their failure behaviors under various conditions. However, the complicated structures of CFRP composites lead to complex mechanical behaviors and a wide variety of failure modes. Experimental analyses usually fall short in precisely controlling the geometries and boundary conditions of the specimen, and such analyses alone are insufficient to investigate the failure initiation process and the subsequent failure mechanisms. On the other hand, computational studies are advantageous in the systematic characterization of the effects of fiber and matrix properties as well as microstructures on the composites' mechanical responses [253-255]. As a result, in the project "Integrated Computational Materials Engineering Development of Carbon Fiber Composites for Lightweight Vehicles", led by Department of Energy and Ford Motor Company, researchers from different institutions aim to develop integrated computational models across multiple length scales and tackle the mechanical properties and failure behaviors of CFRP composites with epoxy resin matrix, of which the target application is the frame materials of next-generation lightweight vehicles.

In this section, first, a microscale RVE model is developed by adopting validated constitutive models for both matrix and fiber phase in the composite. But this two-phase model fails to capture the stress-strain behavior compared to experimental data. We propose that the reason is due to that the two-phase model does not consider the stiffened interphase region between carbon fiber and

matrix. By using MD simulations and an analytical gradient model, we find that the interphase region has higher modulus and strength in average compared to the bulk matrix. Then, we add this stiffened interphase region in RVE modeling and propose a modified three-phase model. We show that the accuracy of the computational model improves significantly [247]. Thus, our findings explicitly elucidate the effect of the nanoscale interphase region on the mechanical properties of the composites.

7.2.1 Traditional two-phase model fails to predict the realistic stress-strain curve

First, accurate constitutive laws for both fiber and epoxy matrix have been adopted. Since fibers are very brittle, a transversely isotropic linear elastic law is adopted. The material constants such as Young's moduli in different directions, shear moduli, and Poisson ratio are obtained from factory material sheets. The epoxy matrix is modeled as an elasto-plastic solid, and the yield criterion and damage law follow a recent work by Vu-Bac et al. [95]. The basic parameters such as Young's modulus and Poisson's ratio are obtained from experimental characterization. Then, the entire matrix constitutive model is validated by experimental results under tension, compression, and torsion [247]. After the validation process, the matrix and fiber models are integrated into the two-phase RVE model to predict the failure behavior of unidirectional (UD) CFRP composites. A portion of the model is shown in Fig. 7-4(a). A zero-thickness interface layer is also highlighted at which cohesive elements are inserted. Typical RVE size is shown in Fig. 7-4(b) and (c) for transverse compression and tension, respectively, and previous studies have shown that this size is sufficient to capture the essential microscale features with minimal computational costs [256]. An orphan mesh technique with predominantly first-order hexahedral elements under reduced integration (C3D8R) and tetrahedral elements (C3D6) are adopted, while first-order cohesive elements (COH3D8) are used to represent the interface.

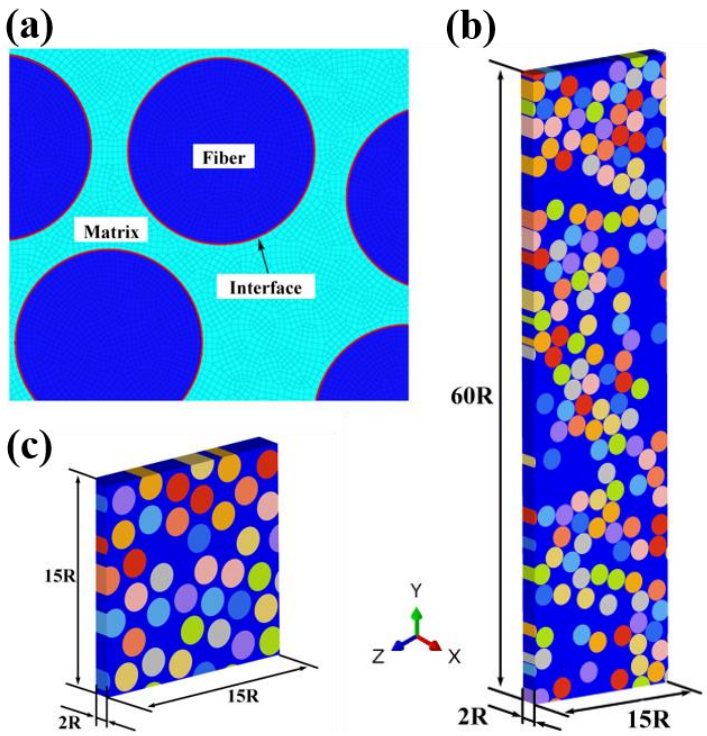

Figure 7-4. Two-phase RVE model. (a) Schematic highlighting the two phases and the interface between them. (b) RVE model for composites failure analysis under transverse compression. (c) RVE model for composites failure analysis under transverse tension and shear loading.

Comparing experimental results with the two-phase RVE model in Fig. 7-5, we find that the stress-strain curves of transverse tension obtained from the two-phase model show earlier non-linearity and the engineering stress is lower than the ones from experimental data in the same condition, indicating lower Young's modulus as well. By changing the cohesive element parameters, it only changes the maximum stress values. It indicates that the traditional two-phase model that only consists of matrix and fiber cannot capture the realistic behavior of composite, especially in the nonlinear stage. Our computational analysis further shows that the region surrounding the fiber is the stress concentration locus. As a result, this region usually yields earlier, and it is the crack initiation site.

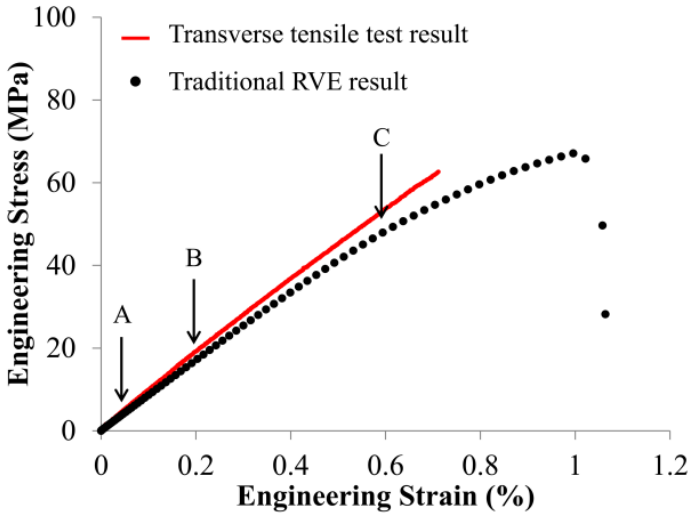

Figure 7-5. The comparison between two-phase model and experimental result of transverse tension.

7.2.2 Interphase property characterization

Due to the roughness of carbon fiber surface, nanoconfinement effect on the matrix resins and the treatments applied during fiber manufacturing process, there exists a submicron-thick interphase region around carbon fibers. For similar CFRP composites with epoxy matrix, the thickness of the interphase region has been evaluated to be about 200 nm with an analysis from transmission electron microscopy (TEM) [257]. Here, the interphase region is further simplified as a cylindrical shell adjacent to the fiber with inner radius r_f being the same as the fiber radius and outer radius $r_i = r_f + 200\ nm$, as shown in Fig. 7-6(a). In the following text, sub-indices f, i and m denote fiber, interphase region and matrix, respectively. Although there has not been a quantitative characterization of the interphase region in situ, we know some basic information of the property variation of the interphase region. First, at the inner and outer boundaries, both physical and chemical properties of the interphase are required to comply with the adjacent phases [258]. Second, there exist a sharp gradient from fiber property to the matrix property within the

interphase region. Third, due to the incompatibility between the sizing on the fiber surface and the resin in the bulk matrix, we anticipate part of the regions within the interphase achieve lower crosslink degree. Previous studies also suggest that the crosslink degree difference might be larger than 30% [258-260]. The experimental observation that the failure initiate inside the interphase region provides further evidence [261]. In the Chapter 6, we have characterized the effect of crosslink degree on the elastic modulus and strength of typical epoxy resins. The results show that the difference of the Young's moduli between insufficiently crosslinked epoxy (~70% crosslink degree) and fully crosslinked epoxy (95% crosslink degree) is around 20%, and the difference in the strength between them is up to 50%. We use E_{ms} and σ_{ms} to represent the lower bound values for the Young's modulus and strength inside the interphase region.

To characterize the average properties of the interphase region, we adopt an analytical gradient model to represent the modulus and strength profile inside the interphase by also integrating the MD simulation results on the insufficient crosslinked resins. The gradient model proposed here include two parts. In the first part, Young's modulus and strength decrease from the fiber values to the lowest values, i.e. E_{ms} and σ_{ms}. In the second part, the values gradually increase from the lowest to the values of bulk matrix. The decreasing trend in the first part is due to the attenuation of the fiber confinement effect, and the increasing trend in the second part is because of the intrinsic epoxy resin stiffening through sufficient crosslinking. To formulate the boundary conditions of the interphase region, the Young's modulus on the left boundary (fiber end) is taken as the average moduli of the fiber in three dimensions $E_i(r = r_f) = 95\ GPa$. The Young's modulus on the right boundary (matrix end) is also taken as the modulus of the isotropic matrix $E_i(r = r_i) = 3.8\ GPa$. For strength values, we use tensile strength values as the composites usually fail by tension even during compressive deformation. Specifically, the left bound strength value of the interphase

region is the tensile strength of the carbon fibers, which is $\sigma_i(r = r_f) = 3\ GPa$. The right bound strength value is the tensile strength of the matrix, which is $\sigma_i(r = r_i) = 68\ MPa$. The position of the lowest values (r_{is}) is assumed to be at three quarters (0.75) of the interphase away from the fiber surface. The position is chosen near the matrix side, since the incompatibility between sizing and bulk matrix resin mainly induces the insufficient crosslinking.

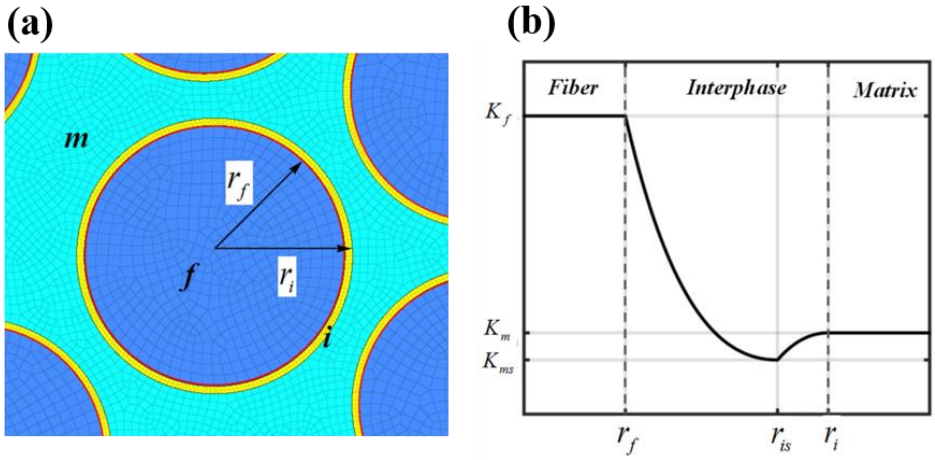

Figure 7-6. Interphase property characterization. (a) Schematic of cross-section including the interphase region (yellow). (b) Variation of Young's modulus or strength inside the interphase region.

The variations of the properties of the interphase region are assumed to follow the exponential functional as follows:

$$K_i = \begin{cases} K_{ms} + (K_f - K_{ms})R(r) & r_f < r < r_{is} \\ K_m + (K_{ms} - K_m)Q(r) & r_{is} < r < r_i \end{cases} \quad (7\text{-}3)$$

where K can be either E (Young's modulus) or σ (strength), and the functions $R(r)$ and $Q(r)$ are constructed to match the boundary conditions:

$$R(r) = \frac{1-(r/r_{is})\exp(1-r/r_{is})}{1-(r_f/r_{is})\exp(1-r_f/r_{is})} \tag{7-4}$$

$$Q(r) = \frac{1-(r/r_i)\exp(1-r/r_i)}{1-(r_{is}/r_i)\exp(1-r_{is}/r_i)} \tag{7-5}$$

The average Young's modulus and strength of the interphase can be obtained as:

$$\overline{K_i} = \int_{r_f}^{r_i} K_i(r)dr\,/(r_i - r_f) \tag{7-6}$$

Substituting the parameters of both Young's modulus and strength values into above equation, we finally have $\bar{E}_i = 22.5\ GPa$, and $\bar{\sigma}_i = 670\ MPa$.

We have also conducted sensitivity analysis to quantify how the choice of r_{is} influences the results. Varying r_{is} between the middle point and further near the matrix phase leads to differences that are smaller than 20% of the predicted average values. As a result, the assumed position of the insufficient crosslink region has low influence on the average properties of the interphase region.

Comparing with matrix modulus ($E_m = 3.8\ GPa$) and tensile strength (($\sigma_m = 68\ MPa$), the average Young's modulus and strength of the interphase region are increased by around 5 and 9 times, respectively. The interphase region shows an obviously stiffened response compared to the bulk matrix, although a portion of the interphase region is weaker due to insufficient crosslinking. Thus, the key material parameters of the interphase region have been obtained. The constitutive behavior and damage model of the interphase are assumed to be similar to those of the bulk matrix.

7.2.3 Newly proposed three-phase model

A modified RVE model incorporating the stiffened interphase region is then proposed to investigate the mechanical response of composites. Fig. 7-7 shows the comparison of stress-strain curves based on the modified and traditional RVE model for the transverse tension and

compression. We see a better agreement for the modified RVE model compared to the experimental tests before failure. It is remarkable that by adding a 200 nm thick interphase region, with stiffened properties compared to the bulk matrix, the model performance becomes much better. This result also corroborates the fact that the existence of finite thickness interphase around carbon fiber increases the loading bearing capability of the composites.

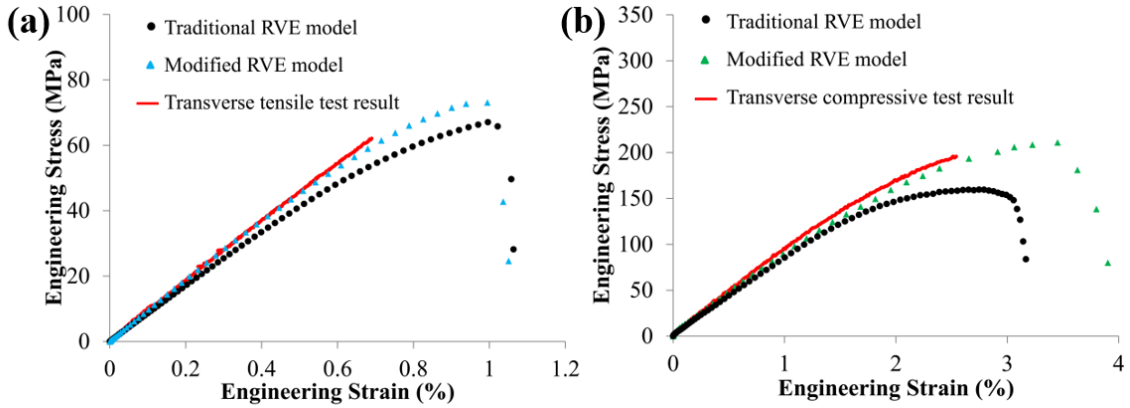

Figure 7-7. Comparison between the modified RVE model including the interphase region and the traditional RVE model. (a) Transverse tension. (b) Transverse compression.

We see that the strength or maximum stress values from the computational model is still a little off compared to experimental results. However, the differences can be corrected by considering interfacial debonding with cohesive elements at the interface between fiber and the interphase region. The specific parameters for the inserted cohesive elements are obtained through reverse engineering method based on the experimental results. Details can be found in our previously published work [247].

7.3 Failure mechanisms characterized by the computational model

With great enhancement of the model performance, we then use the three-phase computational model to characterize the failure mechanisms of UD CFRP composites in accordance with

experimental tests. Compared to experimental tests, the computational model has the advantage to clearly reveal the damage initiation and evolution process.

First, we conduct transverse tension loading in both experiments and computational modeling. From computational results, we find that interfacial debonding first occurs at the poles of the closely packed fibers where the stress concentration is high. Subsequently, initiation of interfacial cracks adjacent to fiber surfaces can be found perpendicular to the loading direction. The matrix and interphase region near to the cracks undergo severe plastic deformation, which further results in the coalescence of the adjacent cracks, as shown in Fig. 7-8(a). Finally, a major crack spreads out the entire RVE model, causing the ultimate fracture perpendicular to the loading axis, as illustrated in Fig. 7-8(b). We also show a post-mortem specimen after brittle matrix fracture in Fig. 7-8(c). We can see that the failure mechanism and crack direction are consistent between the computational modeling and experiments.

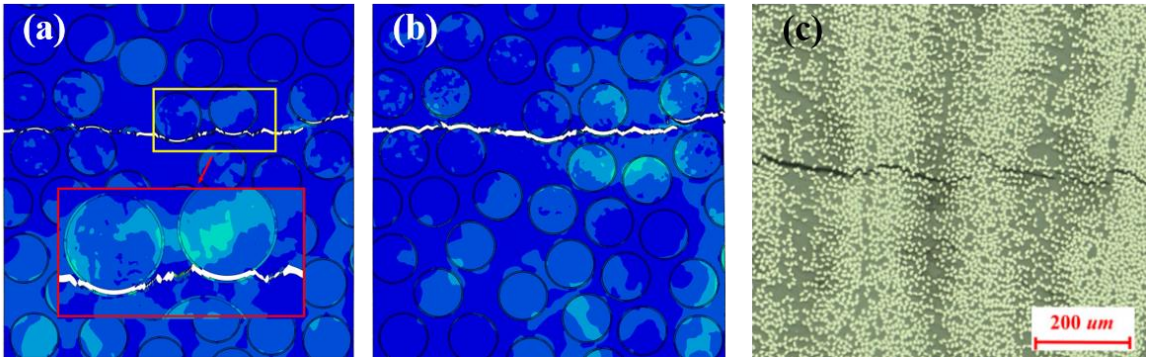

Figure 7-8. Comparison of failure mechanism and crack direction between computational model and experiments under transverse tension.

During transverse compression, we observe that plastic deformation first occurs in the interphase region, which later results in interfacial debonding at specific sites. Again, this phenomenon demonstrates that the failure always initiates in the region near fiber surface, where

stress concentrates more compared to the matrix far away from fiber surface, as shown in Fig. 7-9(a). Afterwards, small cracks from interfacial debonding connect to form a main crack, which can also be treated as a plastic shear band. Finally, a fracture surface forms by the main crack, which inclines at 57.12° with respect to the plane perpendicular to the loading axis, as shown in Fig. 7-9(b). The angle of fracture surface measured in experiments is about 56.15°. Again, we see very good agreement between the computational and experimental results.

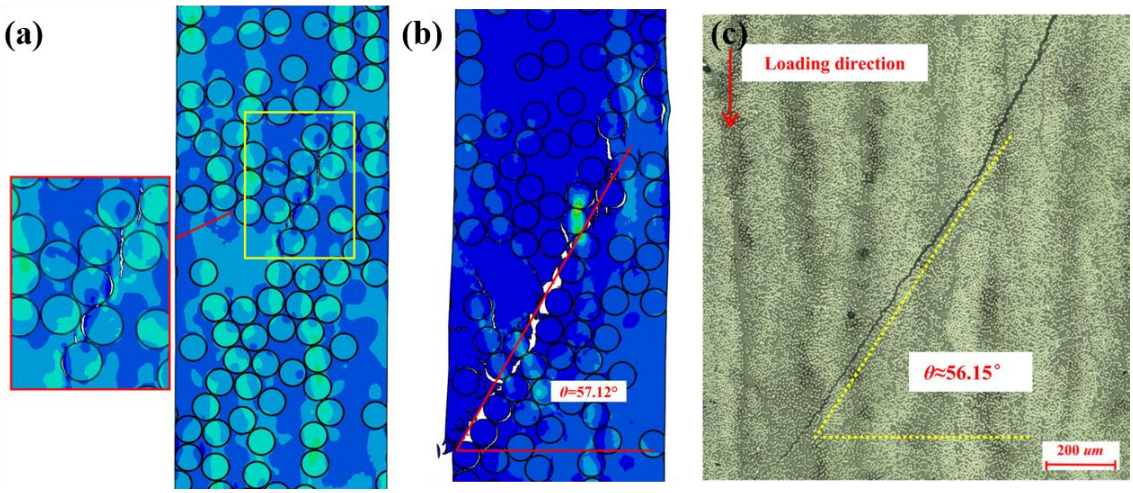

Figure 7-9. Comparison of failure mechanism and crack direction between computational model and experiments under transverse compression.

7.4 Conclusion

In conclusion for this chapter, computational and analytical models are developed to investigate the mechanical properties and failure mechanisms of typical composite systems. Specifically, the CG model of MLG and the CG model of PMMA are used to build a nacre-inspired layered nanocomposite system. The simulation results show that there are two possible failure mechanisms that could occur during MLG phase pull-out from the matrix. One is clean pull-out that results in interfacial failure, and the other one is MLG yielding, indicating failure inside the

MLG phase. To further explain the transition between the two failure mechanisms, a continuum mechanics model is applied to predict the critical number of layers in MLG that results in a transition of failure mechanisms. This analytical model also enables the investigations on the effect of other physical parameters such as total length of the system, and interfacial interaction between MLG and PMMA on the failure mechanisms.

During the investigation of carbon fiber reinforced epoxy resin composites, the traditional two-phase model usually fails to capture the realistic mechanical response of the composites despite that the constitutive law and parameters of the matrix and fiber phases are well calibrated and validated according to experimental tests. This work shows that the nanoscale interphase region between fiber and bulk matrix is essential to capture the confinement effect of fiber surface on the resin matrix. By adopting previous MD simulation results on typical epoxy resin and an analytical gradient model, the average Young's modulus and strength of the interphase region is calibrated, which show stiffened properties compared to the bulk matrix. By integrating the interphase region in a modified RVE model, the performance of the model significantly improves. Afterwards, this multiscale computational model is utilized to study the failure behaviors of the composites under transverse tension and compression, which show excellent agreement with experimental analysis. In this work, a successful effort to integrate MD simulation results with microscale RVE model to investigate the failure response of composites has been demonstrated. This work also demonstrates the importance of characterizing nanoscale features in assessing the overall mechanical properties of the materials.

Chapter 8: Summary

In the previous chapters, investigations on multiscale modeling and mechanics of graphene-based nanomaterials and carbon fiber reinforced epoxy resin composites have been presented. In this chapter, the main contributions of our study and provide an outlook for future research are summarized.

8.1 Contributions

Developing advanced nanocomposites and composites would benefit many application areas. However, understanding and predicting the mechanical responses, especially the large deformation and failure behaviors of such systems and their constituents are still challenging due to limitations of current characterization methods.

The work presented in this dissertation aims to advance the understanding and prediction of the physical mechanisms and failure behaviors of two representative material systems, graphene-based nanomaterials and carbon fiber reinforced epoxy resin composites, by using combined computational, experimental, and analytical characterization methods, with MD simulation as a basic computation technique.

First, in Chapter 3, coarse-grained (CG) models of graphene and graphene oxide (GO) were introduced and developed. They are well designed and calibrated to reproduce the essential mechanical properties of MLG and GO sheets. These models significantly increase the computational efficiency of MD simulations compared to all-atomistic ones. In the following chapters, they served as important predictive computational tools for investigating the physical mechanisms and failure behaviors of mesoscale MLG and GO systems, as well as graphene-based nanocomposites.

In Chapter 4, these new computational models were utilized to investigate multilayer graphene (MLG) sheets and GO sheets under nanoindentation and fracture toughness measurements. By collaborating with experimentalists, an atomic-level recoverable interlayer slippage process in MLG was discovered for the first time, which leads to repeatable energy dissipation of MLG sheets under nanoindentation cycling tests. Also, the experimentally measured, thickness-dependent strength of MLG sheets was successfully elucidated, which had previously remained unexplained. Later, this work inspired other experimental efforts in investigating the interlayer shear properties of similar 2D materials [153, 190]. By using the CG model of GO, the dependence of failure modes during nanoindentation on the chemistry of contact area were illustrated, corroborating the observations of recent nanoindentation experiments. In addition, these models enabled the quantification of the fracture toughness of graphene or GO sheets with excellent accuracy and efficiency.

In Chapter 5, CG models were further utilized to investigate the ballistic impact behavior of MLG sheets, inspired by the recent microballistic tests and the excellent behaviors of MLG under these conditions. Using CG MD simulations, the distinctive failure mechanisms induced by stress waves were shown to deteriorate the ballistic resistance of MLG sheets. Specifically, the cone wave formed upon impact – which travels in-plane at very high speed in thin graphene membranes – can reflect at clamped boundaries and induce early perforation or decrease the energy absorption capability. The compressive wave in the thickness direction can also result in spalling failure, a phenomenon usually observed in the impact on the macroscopic concrete specimen. Later, to relate these failure mechanisms to microballistic experiments, analytical relationships based on continuum mechanics theories were developed to generalize these findings and bridge different size scales.

Chapter 6 focused on the atomistic modeling of a typical matrix material used in both graphene-based nanocomposites and carbon fiber reinforced composites - epoxy resins. The effect of resin functionality, crosslink degree, and component ratio on the resin thermomechanical properties were characterized. More importantly, using a polymer fracture mechanics model, the atomistic tensile simulations of the resin were linked with its macroscopic fracture energy, providing physical insights into the molecular mechanisms that govern the fracture characteristics of epoxy resins. This work could provide guidance for future epoxy resin computational-based design.

In Chapter 7, building upon the previously developed computational tools, the mechanical properties and failure behaviors of nacre-inspired nanocomposites with layered MLG and PMMA matrix and carbon fiber reinforce epoxy resin composites were investigated. First, with CG model of both MLG and PMMA, the failure mechanisms of MLG/PMMA nanocomposites during MLG phase pull-out were studied. A continuum mechanics model was applied to illustrate the transition in failure mechanisms. Then, by collaborating with Ford engineers, a multiscale computational model was developed by combining MD simulations and finite element analysis. It has shown that the nanoscale interphase region between the carbon fibers and resin matrix significantly influences the composite non-linear and failure response. The framework of integrating multiscale analysis and experimental characterizations is one of the key contributions of the multi-institutional collaborative project - Integrated Computational Materials Engineering Development of Carbon Fiber Composites for Lightweight Vehicles.

8.2 Outlook into future

Having summarized our key findings and their significance, in this section I will briefly discuss future potential research directions that build upon this dissertation.

The computational tools and combined computational/theoretical/experimental approach developed here can be further extended to a systematic exploration of the impact resistance and energy absorption mechanisms of biological materials. Developing impact-resistant protective materials or structures has always been crucial. Recently, there is great interest in impact assessment in the field of stretchable and wearable electronics because these devices may undergo accidental shocks during their service life [262]. The need for protective structures in much smaller devices calls for timely investigations focusing on nanoscale characterization and properties that emerge from nanostructures. Biological materials widely found across species, including the exoskeletons of beetles [263], the dactyl club of stomatopods [264], and conch shells [265], have shown remarkable impact resistance and energy absorption capability when undergoing high-speed impact. The exceptional properties of these biological materials are closely related to their intricate, self-assembled, and hierarchical structures. Although the structure-property relationships of biological materials have been investigated under quasi-static loading conditions, and we have witnessed the bio-inspired design of nanocomposites that have high specific toughness and low weight, the relationships are rarely explored under high strain rate conditions. There are still many unexploited solutions offered by biological materials that could be applied to future protective systems.

Therefore, future research can be conducted to explore the impact resistance and energy absorption mechanisms utilized by biological materials, and to apply these principles to design synthetic nanocomposite materials with impact-resistant and protective capabilities. This research direction can build upon the CG model development and the work on the failure mechanisms of nanocomposite systems. Specifically, we can utilize the wide varieties of CG models developed herein to construct both shell-inspired and dactyl-inspired systems. For the shell-inspired system,

one intriguing question would be how the nanoscale dimensions, i.e. nanoconfinement effect and the distinct material properties in the lamellar structures influence the stress wave filtering and damping performance. For the dactyl-inspired system, it is interesting to investigate the specific role of amorphous minerals in energy dissipation or absorption.

In addition, future research can also focus on unraveling how multilevel hierarchical structures optimize the ability to withstand extreme mechanical forces. I think the key is whether there are hybridized failure mechanisms emerging in hierarchical structures, and if so, what their roles are in enhancing impact-resistant performance. During conducting this research, multiscale modeling and combined theoretical/computational approaches would be highly valuable in investigating the structure-property relationships. In addition, these studies will be helpful to generalize the lessons learned from biological materials into mathematical principles, that can be integrated into bottom-up, hierarchical materials design.

References

[1] K.S. Novoselov, A.K. Geim, S.V. Morozov, D. Jiang, Y. Zhang, S.V. Dubonos*, et al.*, Electric field effect in atomically thin carbon films, science 306(5696) (2004) 666-669.
[2] A.A. Balandin, S. Ghosh, W. Bao, I. Calizo, D. Teweldebrhan, F. Miao*, et al.*, Superior thermal conductivity of single-layer graphene, Nano letters 8(3) (2008) 902-907.
[3] K.S. Novoselov, A.K. Geim, S. Morozov, D. Jiang, M. Katsnelson, I. Grigorieva*, et al.*, Two-dimensional gas of massless Dirac fermions in graphene, nature 438(7065) (2005) 197.
[4] C. Lee, X. Wei, J.W. Kysar, J. Hone, Measurement of the elastic properties and intrinsic strength of monolayer graphene, science 321(5887) (2008) 385-388.
[5] S. Stankovich, D.A. Dikin, G.H. Dommett, K.M. Kohlhaas, E.J. Zimney, E.A. Stach*, et al.*, Graphene-based composite materials, nature 442(7100) (2006) 282-286.
[6] J.R. Potts, D.R. Dreyer, C.W. Bielawski, R.S. Ruoff, Graphene-based polymer nanocomposites, Polymer 52(1) (2011) 5-25.
[7] R.J. Young, I.A. Kinloch, L. Gong, K.S. Novoselov, The mechanics of graphene nanocomposites: a review, Composites Science and Technology 72(12) (2012) 1459-1476.
[8] G. Eda, M. Chhowalla, Chemically derived graphene oxide: towards large‐area thin‐film electronics and optoelectronics, Advanced materials 22(22) (2010) 2392-2415.
[9] S.-H. Bae, Y. Lee, B.K. Sharma, H.-J. Lee, J.-H. Kim, J.-H. Ahn, Graphene-based transparent strain sensor, Carbon 51 (2013) 236-242.
[10] A.P.A. Raju, A. Lewis, B. Derby, R.J. Young, I.A. Kinloch, R. Zan*, et al.*, Wide‐Area Strain Sensors based upon Graphene‐Polymer Composite Coatings Probed by Raman Spectroscopy, Advanced Functional Materials 24(19) (2014) 2865-2874.
[11] Y. Wang, L. Wang, T. Yang, X. Li, X. Zang, M. Zhu*, et al.*, Wearable and highly sensitive graphene strain sensors for human motion monitoring, Advanced Functional Materials 24(29) (2014) 4666-4670.
[12] S. Patchkovskii, S.T. John, S.N. Yurchenko, L. Zhechkov, T. Heine, G. Seifert, Graphene nanostructures as tunable storage media for molecular hydrogen, P Natl Acad Sci USA 102(30) (2005) 10439-10444.
[13] J.J. Yoo, K. Balakrishnan, J. Huang, V. Meunier, B.G. Sumpter, A. Srivastava*, et al.*, Ultrathin planar graphene supercapacitors, Nano letters 11(4) (2011) 1423-1427.
[14] D.A. Brownson, C.E. Banks, Fabricating graphene supercapacitors: highlighting the impact of surfactants and moieties, Chemical Communications 48(10) (2012) 1425-1427.
[15] X. Wang, L. Zhi, K. Müllen, Transparent, conductive graphene electrodes for dye-sensitized solar cells, Nano letters 8(1) (2008) 323-327.
[16] X. Miao, S. Tongay, M.K. Petterson, K. Berke, A.G. Rinzler, B.R. Appleton*, et al.*, High efficiency graphene solar cells by chemical doping, Nano letters 12(6) (2012) 2745-2750.
[17] D.G. Papageorgiou, I.A. Kinloch, R.J. Young, Mechanical properties of graphene and graphene-based nanocomposites, Progress in Materials Science 90 (2017) 75-127.
[18] O.V. Yazyev, S.G. Louie, Topological defects in graphene: Dislocations and grain boundaries, Physical Review B 81(19) (2010) 195420.
[19] H. Li, H. Zhang, X. Cheng, The effect of temperature, defect and strain rate on the mechanical property of multi-layer graphene: Coarse-grained molecular dynamics study, Physica E: Low-dimensional Systems and Nanostructures 85 (2017) 97-102.
[20] T. Zhang, X. Li, S. Kadkhodaei, H. Gao, Flaw insensitive fracture in nanocrystalline graphene, Nano letters 12(9) (2012) 4605-4610.
[21] X. Li, W. Cai, J. An, S. Kim, J. Nah, D. Yang*, et al.*, Large-area synthesis of high-quality and uniform graphene films on copper foils, Science 324(5932) (2009) 1312-1314.

[22] P.Y. Huang, C.S. Ruiz-Vargas, A.M. van der Zande, W.S. Whitney, S. Garg, J.S. Alden*, et al.*, Imaging grains and grain boundaries in single-layer graphene: An atomic patchwork quilt, arXiv preprint arXiv:1009.4714 (2010).
[23] P.Y. Huang, C.S. Ruiz-Vargas, A.M. van der Zande, W.S. Whitney, M.P. Levendorf, J.W. Kevek*, et al.*, Grains and grain boundaries in single-layer graphene atomic patchwork quilts, Nature 469(7330) (2011) 389.
[24] C.S. Ruiz-Vargas, H.L. Zhuang, P.Y. Huang, A.M. Van Der Zande, S. Garg, P.L. McEuen*, et al.*, Softened elastic response and unzipping in chemical vapor deposition graphene membranes, Nano letters 11(6) (2011) 2259-2263.
[25] G. Jung, Z. Qin, M.J. Buehler, Molecular mechanics of polycrystalline graphene with enhanced fracture toughness, Extreme Mechanics Letters 2 (2015) 52-59.
[26] P. Zhang, L. Ma, F. Fan, Z. Zeng, C. Peng, P.E. Loya*, et al.*, Fracture toughness of graphene, Nature communications 5 (2014).
[27] Y. Wei, J. Wu, H. Yin, X. Shi, R. Yang, M. Dresselhaus, The nature of strength enhancement and weakening by pentagon–heptagon defects in graphene, Nature materials 11(9) (2012) 759-763.
[28] J. Wu, Y. Wei, Grain misorientation and grain-boundary rotation dependent mechanical properties in polycrystalline graphene, Journal of the Mechanics and Physics of Solids 61(6) (2013) 1421-1432.
[29] G. Titelman, V. Gelman, S. Bron, R. Khalfin, Y. Cohen, H. Bianco-Peled, Characteristics and microstructure of aqueous colloidal dispersions of graphite oxide, Carbon 43(3) (2005) 641-649.
[30] S. Stankovich, R.D. Piner, X. Chen, N. Wu, S.T. Nguyen, R.S. Ruoff, Stable aqueous dispersions of graphitic nanoplatelets via the reduction of exfoliated graphite oxide in the presence of poly (sodium 4-styrenesulfonate), Journal of Materials Chemistry 16(2) (2006) 155-158.
[31] S. Stankovich, D.A. Dikin, R.D. Piner, K.A. Kohlhaas, A. Kleinhammes, Y. Jia*, et al.*, Synthesis of graphene-based nanosheets via chemical reduction of exfoliated graphite oxide, Carbon 45(7) (2007) 1558-1565.
[32] N.V. Medhekar, A. Ramasubramaniam, R.S. Ruoff, V.B. Shenoy, Hydrogen bond networks in graphene oxide composite paper: structure and mechanical properties, Acs Nano 4(4) (2010) 2300-2306.
[33] Y. Gao, L.-Q. Liu, S.-Z. Zu, K. Peng, D. Zhou, B.-H. Han*, et al.*, The effect of interlayer adhesion on the mechanical behaviors of macroscopic graphene oxide papers, ACS nano 5(3) (2011) 2134-2141.
[34] O.C. Compton, S.T. Nguyen, Graphene Oxide, Highly Reduced Graphene Oxide, and Graphene: Versatile Building Blocks for Carbon‐Based Materials, Small 6(6) (2010) 711-723.
[35] O.C. Compton, S.W. Cranford, K.W. Putz, Z. An, L.C. Brinson, M.J. Buehler*, et al.*, Tuning the mechanical properties of graphene oxide paper and its associated polymer nanocomposites by controlling cooperative intersheet hydrogen bonding, ACS nano 6(3) (2012) 2008-2019.
[36] Y. Xu, W. Hong, H. Bai, C. Li, G. Shi, Strong and ductile poly (vinyl alcohol)/graphene oxide composite films with a layered structure, Carbon 47(15) (2009) 3538-3543.
[37] T. Ramanathan, A. Abdala, S. Stankovich, D. Dikin, M. Herrera-Alonso, R. Piner*, et al.*, Functionalized graphene sheets for polymer nanocomposites, Nature nanotechnology 3(6) (2008) 327-331.
[38] C. Shao, S. Keten, Stiffness Enhancement in Nacre-Inspired Nanocomposites due to Nanoconfinement, Sci. Rep. 5 (2015) 16452.
[39] W. Xia, J. Song, Z. Meng, C. Shao, S. Keten, Designing multi-layer graphene-based assemblies for enhanced toughness in nacre-inspired nanocomposites, Molecular Systems Design & Engineering 1(1) (2016) 40-47.
[40] Y. Matsuo, K. Tahara, Y. Sugie, Structure and thermal properties of poly (ethylene oxide)-intercalated graphite oxide, Carbon 35(1) (1997) 113-120.
[41] W. Kai, Y. Hirota, L. Hua, Y. Inoue, Thermal and mechanical properties of a poly (ϵ‐caprolactone)/graphite oxide composite, Journal of Applied Polymer Science 107(3) (2008) 1395-1400.

[42] U.G. Wegst, H. Bai, E. Saiz, A.P. Tomsia, R.O. Ritchie, Bioinspired structural materials, Nature materials 14(1) (2015) 23.
[43] H.-B. Yao, H.-Y. Fang, X.-H. Wang, S.-H. Yu, Hierarchical assembly of micro-/nano-building blocks: bio-inspired rigid structural functional materials, Chemical Society Reviews 40(7) (2011) 3764-3785.
[44] H.B. Yao, J. Ge, L.B. Mao, Y.X. Yan, S.H. Yu, 25th anniversary article: artificial carbonate nanocrystals and layered structural nanocomposites inspired by nacre: synthesis, fabrication and applications, Advanced Materials 26(1) (2014) 163-188.
[45] C. Huang, Q. Cheng, Learning from nacre: Constructing polymer nanocomposites, Composites Science and Technology (2017).
[46] Y. Zhang, S. Gong, Q. Zhang, P. Ming, S. Wan, J. Peng*, et al.*, Graphene-based artificial nacre nanocomposites, Chemical Society Reviews 45(9) (2016) 2378-2395.
[47] S. Gong, H. Ni, L. Jiang, Q. Cheng, Learning from nature: constructing high performance graphene-based nanocomposites, Materials Today 20(4) (2017) 210-219.
[48] J. Peng, Q. Cheng, High‐Performance Nanocomposites Inspired by Nature, Advanced Materials 29(45) (2017).
[49] F.-X. Xiao, M. Pagliaro, Y.-J. Xu, B. Liu, Layer-by-layer assembly of versatile nanoarchitectures with diverse dimensionality: a new perspective for rational construction of multilayer assemblies, Chemical Society Reviews 45(11) (2016) 3088-3121.
[50] X. Zhao, Q. Zhang, Y. Hao, Y. Li, Y. Fang, D. Chen, Alternate multilayer films of poly (vinyl alcohol) and exfoliated graphene oxide fabricated via a facial layer-by-layer assembly, Macromolecules 43(22) (2010) 9411-9416.
[51] S. Wan, H. Hu, J. Peng, Y. Li, Y. Fan, L. Jiang*, et al.*, Nacre-inspired integrated strong and tough reduced graphene oxide–poly (acrylic acid) nanocomposites, Nanoscale 8(10) (2016) 5649-5656.
[52] Y. Yang, W. Zhan, R. Peng, C. He, X. Pang, D. Shi*, et al.*, Graphene‐enabled superior and tunable photomechanical actuation in liquid crystalline elastomer nanocomposites, Advanced Materials 27(41) (2015) 6376-6381.
[53] M.F. El-Kady, V. Strong, S. Dubin, R.B. Kaner, Laser scribing of high-performance and flexible graphene-based electrochemical capacitors, Science 335(6074) (2012) 1326-1330.
[54] X. Yang, C. Cheng, Y. Wang, L. Qiu, D. Li, Liquid-mediated dense integration of graphene materials for compact capacitive energy storage, science 341(6145) (2013) 534-537.
[55] R.J. Young, P.A. Lovell, Introduction to polymers, CRC press2011.
[56] J.K. Abraham, B. Philip, A. Witchurch, V.K. Varadan, C.C. Reddy, A compact wireless gas sensor using a carbon nanotube/PMMA thin film chemiresistor, Smart Materials and Structures 13(5) (2004) 1045.
[57] B.J. Ash, R.W. Siegel, L.S. Schadler, Glass‐transition temperature behavior of alumina/PMMA nanocomposites, Journal of Polymer Science Part B: Polymer Physics 42(23) (2004) 4371-4383.
[58] M. Avella, M.E. Errico, E. Martuscelli, Novel PMMA/CaCO3 nanocomposites abrasion resistant prepared by an in situ polymerization process, Nano letters 1(4) (2001) 213-217.
[59] C. May, Epoxy resins: chemistry and technology, CRC press1987.
[60] J.-P. Pascault, H. Sautereau, J. Verdu, R.J. Williams, Thermosetting polymers, CRC Press2002.
[61] J.-H. Lee, D. Veysset, J.P. Singer, M. Retsch, G. Saini, T. Pezeril*, et al.*, High strain rate deformation of layered nanocomposites, Nature communications 3 (2012) 1164.
[62] L. Gong, I.A. Kinloch, R.J. Young, I. Riaz, R. Jalil, K.S. Novoselov, Interfacial stress transfer in a graphene monolayer nanocomposite, Advanced Materials 22(24) (2010) 2694-2697.
[63] J. Affdl, J. Kardos, The Halpin‐Tsai equations: a review, Polymer Engineering & Science 16(5) (1976) 344-352.
[64] T. Mori, K. Tanaka, Average stress in matrix and average elastic energy of materials with misfitting inclusions, Acta metallurgica 21(5) (1973) 571-574.

[65] G. Tandon, G. Weng, The effect of aspect ratio of inclusions on the elastic properties of unidirectionally aligned composites, Polymer composites 5(4) (1984) 327-333.
[66] G. Marom, H.D. Wagner, Should polymer nanocomposites be regarded as molecular composites?, Journal of materials science 52(14) (2017) 8357-8361.
[67] C. Vallés, F. Beckert, L. Burk, R. Mülhaupt, R.J. Young, I.A. Kinloch, Effect of the C/O ratio in graphene oxide materials on the reinforcement of epoxy-based nanocomposites, Journal of Polymer Science Part B: Polymer Physics 54(2) (2016) 281-291.
[68] J.A. King, D.R. Klimek, I. Miskioglu, G.M. Odegard, Mechanical properties of graphene nanoplatelet/epoxy composites, Journal of Applied Polymer Science 128(6) (2013) 4217-4223.
[69] H. Cox, The elasticity and strength of paper and other fibrous materials, British journal of applied physics 3(3) (1952) 72.
[70] A. Kelly, N.H. Macmillan, Strong Solids, Oxford University Press, Walton Street, Oxford OX 2 6 DP, UK, 1986. (1986).
[71] T. Jiang, R. Huang, Y. Zhu, Interfacial sliding and buckling of monolayer graphene on a stretchable substrate, Advanced Functional Materials 24(3) (2014) 396-402.
[72] X. Li, J. Warzywoda, G.B. McKenna, Mechanical responses of a polymer graphene-sheet nano-sandwich, Polymer 55(19) (2014) 4976-4982.
[73] G. Wang, Z. Dai, L. Liu, H. Hu, Q. Dai, Z. Zhang, Tuning the interfacial mechanical behaviors of monolayer graphene/PMMA nanocomposites, ACS applied materials & interfaces 8(34) (2016) 22554-22562.
[74] W. Xia, L. Ruiz, N.M. Pugno, S. Keten, Critical length scales and strain localization govern the mechanical performance of multi-layer graphene assemblies, Nanoscale 8(12) (2016) 6456-6462.
[75] X. Wei, M. Naraghi, H.D. Espinosa, Optimal length scales emerging from shear load transfer in natural materials: application to carbon-based nanocomposite design, ACS nano 6(3) (2012) 2333-2344.
[76] X. Wei, T. Filleter, H.D. Espinosa, Statistical shear lag model–Unraveling the size effect in hierarchical composites, Acta biomaterialia 18 (2015) 206-212.
[77] J. Rottler, S. Barsky, M.O. Robbins, Cracks and crazes: on calculating the macroscopic fracture energy of glassy polymers from molecular simulations, Phys. Rev. Lett. 89(14) (2002) 148304.
[78] Z. Meng, M.A. Bessa, W. Xia, W. Kam Liu, S. Keten, Predicting the Macroscopic Fracture Energy of Epoxy Resins from Atomistic Molecular Simulations, Macromolecules 49(24) (2016) 9474-9483.
[79] S.L. Mayo, B.D. Olafson, W.A. Goddard, DREIDING: a generic force field for molecular simulations, Journal of Physical chemistry 94(26) (1990) 8897-8909.
[80] M. Tuckerman, B.J. Berne, G.J. Martyna, Reversible multiple time scale molecular dynamics, The Journal of chemical physics 97(3) (1992) 1990-2001.
[81] S. Plimpton, Fast parallel algorithms for short-range molecular dynamics, Journal of computational physics 117(1) (1995) 1-19.
[82] J.C. Phillips, R. Braun, W. Wang, J. Gumbart, E. Tajkhorshid, E. Villa*, et al.*, Scalable molecular dynamics with NAMD, Journal of computational chemistry 26(16) (2005) 1781-1802.
[83] H.J. Berendsen, D. van der Spoel, R. van Drunen, GROMACS: a message-passing parallel molecular dynamics implementation, Computer Physics Communications 91(1-3) (1995) 43-56.
[84] J.W. Gibbs, Elementary principles in statistical mechanics, Courier Corporation2014.
[85] W.L. Jorgensen, D.S. Maxwell, J. Tirado-Rives, Development and testing of the OPLS all-atom force field on conformational energetics and properties of organic liquids, Journal of the American Chemical Society 118(45) (1996) 11225-11236.
[86] D.A. Pearlman, D.A. Case, J.W. Caldwell, W.S. Ross, T.E. Cheatham III, S. DeBolt*, et al.*, AMBER, a package of computer programs for applying molecular mechanics, normal mode analysis, molecular dynamics and free energy calculations to simulate the structural and energetic properties of molecules, Computer Physics Communications 91(1-3) (1995) 1-41.

[87] B.R. Brooks, R.E. Bruccoleri, B.D. Olafson, D.J. States, S. Swaminathan, M. Karplus, CHARMM: a program for macromolecular energy, minimization, and dynamics calculations, Journal of computational chemistry 4(2) (1983) 187-217.
[88] C. Oostenbrink, A. Villa, A.E. Mark, W.F. Van Gunsteren, A biomolecular force field based on the free enthalpy of hydration and solvation: the GROMOS force‐field parameter sets 53A5 and 53A6, Journal of computational chemistry 25(13) (2004) 1656-1676.
[89] R. Sinko, S. Mishra, L. Ruiz, N. Brandis, S. Keten, Dimensions of biological cellulose nanocrystals maximize fracture strength, ACS Macro Letters 3(1) (2013) 64-69.
[90] R. Sinko, S. Keten, Effect of moisture on the traction-separation behavior of cellulose nanocrystal interfaces, Applied Physics Letters 105(24) (2014) 243702.
[91] R. Sinko, S. Keten, Traction–separation laws and stick–slip shear phenomenon of interfaces between cellulose nanocrystals, Journal of the Mechanics and Physics of Solids 78 (2015) 526-539.
[92] E. Hamed, T. Xu, S. Keten, Poly (ethylene glycol) conjugation stabilizes the secondary structure of α-helices by reducing peptide solvent accessible surface area, Biomacromolecules 14(11) (2013) 4053-4060.
[93] E.P. DeBenedictis, E. Hamed, S. Keten, Mechanical Reinforcement of Proteins with Polymer Conjugation, ACS nano 10(2) (2015) 2259-2267.
[94] D.D. Hsu, W. Xia, S.G. Arturo, S. Keten, Systematic method for thermomechanically consistent coarse-graining: a universal model for methacrylate-based polymers, Journal of chemical theory and computation 10(6) (2014) 2514-2527.
[95] N. Vu-Bac, M. Bessa, T. Rabczuk, W.K. Liu, A Multiscale Model for the Quasi-Static Thermo-Plastic Behavior of Highly Cross-Linked Glassy Polymers, Macromolecules 48(18) (2015) 6713-6723.
[96] M.S. Daw, M.I. Baskes, Embedded-atom method: Derivation and application to impurities, surfaces, and other defects in metals, Physical Review B 29(12) (1984) 6443.
[97] A.C. Van Duin, S. Dasgupta, F. Lorant, W.A. Goddard, ReaxFF: a reactive force field for hydrocarbons, J. Phys. Chem. A 105(41) (2001) 9396-9409.
[98] S.J. Stuart, A.B. Tutein, J.A. Harrison, A reactive potential for hydrocarbons with intermolecular interactions, The Journal of chemical physics 112(14) (2000) 6472-6486.
[99] H. Zhao, K. Min, N. Aluru, Size and chirality dependent elastic properties of graphene nanoribbons under uniaxial tension, Nano letters 9(8) (2009) 3012-3015.
[100] H. Zhao, N. Aluru, Temperature and strain-rate dependent fracture strength of graphene, Journal of Applied Physics 108(6) (2010) 064321.
[101] K. Min, N. Aluru, Mechanical properties of graphene under shear deformation, Applied Physics Letters 98(1) (2011) 013113.
[102] M. Neek-Amal, F. Peeters, Nanoindentation of a circular sheet of bilayer graphene, Physical Review B 81(23) (2010) 235421.
[103] B.Z.G. Haque, S.C. Chowdhury, J.W. Gillespie, Molecular simulations of stress wave propagation and perforation of graphene sheets under transverse impact, Carbon 102 (2016) 126-140.
[104] K. Xia, H. Zhan, D.a. Hu, Y. Gu, Failure mechanism of monolayer graphene under hypervelocity impact of spherical projectile, Scientific Reports 6 (2016).
[105] F. Müller‐Plathe, Coarse‐graining in polymer simulation: from the atomistic to the mesoscopic scale and back, ChemPhysChem 3(9) (2002) 754-769.
[106] S.J. Marrink, H.J. Risselada, S. Yefimov, D.P. Tieleman, A.H. De Vries, The MARTINI force field: coarse grained model for biomolecular simulations, The journal of physical chemistry B 111(27) (2007) 7812-7824.
[107] S. Cranford, D. Sen, M.J. Buehler, Meso-origami: folding multilayer graphene sheets, Applied physics letters 95(12) (2009) 123121.
[108] S.J. Marrink, A.H. De Vries, A.E. Mark, Coarse grained model for semiquantitative lipid simulations, The Journal of Physical Chemistry B 108(2) (2004) 750-760.

[109] M. Seo, S. Rauscher, R.g. Pomès, D.P. Tieleman, Improving internal peptide dynamics in the coarse-grained MARTINI model: toward large-scale simulations of amyloid-and elastin-like peptides, Journal of chemical theory and computation 8(5) (2012) 1774-1785.
[110] Y. Li, B.C. Abberton, M. Kröger, W.K. Liu, Challenges in multiscale modeling of polymer dynamics, Polymers 5(2) (2013) 751-832.
[111] R. Bird, P. Dotson, N. Johnson, Polymer solution rheology based on a finitely extensible bead—spring chain model, Journal of Non-Newtonian Fluid Mechanics 7(2-3) (1980) 213-235.
[112] G.S. Grest, K. Kremer, Molecular dynamics simulation for polymers in the presence of a heat bath, Physical Review A 33(5) (1986) 3628.
[113] K. Kremer, G.S. Grest, Dynamics of entangled linear polymer melts: A molecular‐dynamics simulation, The Journal of Chemical Physics 92(8) (1990) 5057-5086.
[114] M. Kröger, S. Hess, Rheological evidence for a dynamical crossover in polymer melts via nonequilibrium molecular dynamics, Physical review letters 85(5) (2000) 1128.
[115] J.G.H. Cifre, S. Hess, M. Kröger, Linear Viscoelastic Behavior of Unentangled Polymer Melts via Non‐Equilibrium Molecular Dynamics, Macromolecular theory and simulations 13(9) (2004) 748-753.
[116] P.E. Rouse Jr, A theory of the linear viscoelastic properties of dilute solutions of coiling polymers, The Journal of Chemical Physics 21(7) (1953) 1272-1280.
[117] M. Doi, S.F. Edwards, The theory of polymer dynamics, oxford university press1988.
[118] V. Harmandaris, V. Mavrantzas, D. Theodorou, M. Kröger, J. Ramirez, H. Öttinger*, et al.*, Crossover from the rouse to the entangled polymer melt regime: signals from long, detailed atomistic molecular dynamics simulations, supported by rheological experiments, Macromolecules 36(4) (2003) 1376-1387.
[119] D.D. Hsu, W. Xia, S.G. Arturo, S. Keten, Thermomechanically consistent and temperature transferable coarse-graining of atactic polystyrene, Macromolecules 48(9) (2015) 3057-3068.
[120] W. Xia, J. Song, C. Jeong, D.D. Hsu, F.R. Phelan Jr, J.F. Douglas*, et al.*, Energy-Renormalization for Achieving Temperature Transferable Coarse-Graining of Polymer Dynamics, Macromolecules 50(21) (2017) 8787-8796.
[121] W. Xia, J. Song, N.K. Hansoge, F.R. Phelan Jr, S. Keten, J.F. Douglas, Energy Renormalization for Coarse-Graining the Dynamics of a Model Glass-Forming Liquid, The Journal of Physical Chemistry B 122(6) (2018) 2040-2045.
[122] W. Xia, D.D. Hsu, S. Keten, Dependence of polymer thin film adhesion energy on cohesive interactions between chains, Macromolecules 47(15) (2014) 5286-5294.
[123] W. Xia, D.D. Hsu, S. Keten, Molecular weight effects on the glass transition and confinement behavior of polymer thin films, Macromolecular rapid communications 36(15) (2015) 1422-1427.
[124] W. Xia, J. Song, D.D. Hsu, S. Keten, Understanding the Interfacial Mechanical Response of Nanoscale Polymer Thin Films via Nanoindentation, Macromolecules (2016).
[125] X. Qin, W. Xia, R. Sinko, S. Keten, Tuning glass transition in polymer nanocomposites with functionalized cellulose nanocrystals through nanoconfinement, Nano letters 15(10) (2015) 6738-6744.
[126] M. Dienwiebel, G.S. Verhoeven, N. Pradeep, J.W. Frenken, J.A. Heimberg, H.W. Zandbergen, Superlubricity of graphite, Physical Review Letters 92(12) (2004) 126101.
[127] L. Ruiz, W. Xia, Z. Meng, S. Keten, A coarse-grained model for the mechanical behavior of multi-layer graphene, Carbon 82 (2015) 103-115.
[128] Z. Meng, R.A. Soler-Crespo, W. Xia, W. Gao, L. Ruiz, H.D. Espinosa*, et al.*, A coarse-grained model for the mechanical behavior of graphene oxide, Carbon 117 (2017) 476-487.
[129] Z. Xu, X. Li, B.I. Yakobson, F. Ding, Interaction between graphene layers and the mechanisms of graphite's superlubricity and self-retraction, Nanoscale 5(15) (2013) 6736-6741.
[130] X. Feng, S. Kwon, J.Y. Park, M. Salmeron, Superlubric sliding of graphene nanoflakes on graphene, ACS nano 7(2) (2013) 1718-1724.

[131] J.-W. Jiang, J.-S. Wang, B. Li, Young's modulus of graphene: a molecular dynamics study, Physical Review B 80(11) (2009) 113405.
[132] S. Cranford, M.J. Buehler, Twisted and coiled ultralong multilayer graphene ribbons, Modelling and Simulation in Materials Science and Engineering 19(5) (2011) 054003.
[133] Q. Lu, M. Arroyo, R. Huang, Elastic bending modulus of monolayer graphene, Journal of Physics D: Applied Physics 42(10) (2009) 102002.
[134] Q. Lu, R. Huang, Nonlinear mechanics of single-atomic-layer graphene sheets, International Journal of Applied Mechanics 1(03) (2009) 443-467.
[135] L. Girifalco, R. Lad, Energy of cohesion, compressibility, and the potential energy functions of the graphite system, The Journal of chemical physics 25(4) (1956) 693-697.
[136] L.X. Benedict, N.G. Chopra, M.L. Cohen, A. Zettl, S.G. Louie, V.H. Crespi, Microscopic determination of the interlayer binding energy in graphite, Chemical Physics Letters 286(5-6) (1998) 490-496.
[137] R. Zacharia, H. Ulbricht, T. Hertel, Interlayer cohesive energy of graphite from thermal desorption of polyaromatic hydrocarbons, Physical Review B 69(15) (2004) 155406.
[138] P.P. Gillis, Calculating the elastic constants of graphite, Carbon 22(4-5) (1984) 387-391.
[139] W. Xia, J. Song, Z. Meng, C. Shao, S. Keten, Designing multi-layer graphene-based assemblies for enhanced toughness in nacre-inspired nanocomposites, Mol. Syst. Des. Eng. 1(1) (2016) 40--47.
[140] C. Cao, M. Daly, B. Chen, J.Y. Howe, C.V. Singh, T. Filleter*, et al.*, Strengthening in graphene oxide nanosheets: bridging the gap between interplanar and intraplanar fracture, Nano letters 15(10) (2015) 6528-6534.
[141] Q. Zheng, Y. Geng, S. Wang, Z. Li, J.-K. Kim, Effects of functional groups on the mechanical and wrinkling properties of graphene sheets, Carbon 48(15) (2010) 4315-4322.
[142] L. Liu, J. Zhang, J. Zhao, F. Liu, Mechanical properties of graphene oxides, Nanoscale 4(19) (2012) 5910-5916.
[143] R.A. Soler-Crespo, W. Gao, P. Xiao, X. Wei, J.T. Paci, G. Henkelman*, et al.*, Engineering the Mechanical Properties of Monolayer Graphene Oxide at the Atomic Level, The Journal of Physical Chemistry Letters (2016).
[144] J.T. Paci, T. Belytschko, G.C. Schatz, Computational studies of the structure, behavior upon heating, and mechanical properties of graphite oxide, The Journal of Physical Chemistry C 111(49) (2007) 18099-18111.
[145] X. Wei, L. Mao, R.A. Soler-Crespo, J.T. Paci, J. Huang, S.T. Nguyen*, et al.*, Plasticity and ductility in graphene oxide through a mechanochemically induced damage tolerance mechanism, Nature communications 6 (2015).
[146] X. Wei, Z. Meng, L. Ruiz, W. Xia, C. Lee, J.W. Kysar*, et al.*, Recoverable Slippage Mechanism in Multilayer Graphene Leads to Repeatable Energy Dissipation, ACS nano 10(2) (2016) 1820-1828.
[147] J. Bernal, The structure of graphite, Proceedings of the Royal Society of London. Series A, Containing Papers of a Mathematical and Physical Character 106(740) (1924) 749-773.
[148] A.M. Popov, I.V. Lebedeva, A.A. Knizhnik, Y.E. Lozovik, B.V. Potapkin, Commensurate-incommensurate phase transition in bilayer graphene, Phys Rev B 84(4) (2011) 045404.
[149] J.C. Ren, R.Q. Zhang, Z. Ding, M.A. Van Hove, Strong slip-induced anomalous enhancement and red-shifts in wide-range optical absorption of graphite under uniaxial pressure, Nanoscale 6(15) (2014) 8943-8948.
[150] R.A. Bernal, A. Aghaei, S. Lee, S. Ryu, K. Sohn, J. Huang*, et al.*, Intrinsic Bauschinger effect and recoverable plasticity in pentatwinned silver nanowires tested in tension, Nano Lett. 15(1) (2015) 139-146.
[151] R.A. Bernal, T. Filleter, J.G. Connell, K. Sohn, J. Huang, L.J. Lauhon*, et al.*, In situ electron microscopy four-point electromechanical characterization of freestanding metallic and semiconducting nanowires, Small 10(4) (2014) 725-733.

[152] C. Lee, X. Wei, Q. Li, R. Carpick, J.W. Kysar, J. Hone, Elastic and frictional properties of graphene, physica status solidi (b) 246(11‐12) (2009) 2562-2567.
[153] A. Falin, Q. Cai, E.J. Santos, D. Scullion, D. Qian, R. Zhang*, et al.*, Mechanical properties of atomically thin boron nitride and the role of interlayer interactions, Nature communications 8 (2017) 15815.
[154] A.A. Griffith, M. Eng, VI. The phenomena of rupture and flow in solids, Phil. Trans. R. Soc. Lond. A 221(582-593) (1921) 163-198.
[155] R. Grantab, V.B. Shenoy, R.S. Ruoff, Anomalous strength characteristics of tilt grain boundaries in graphene, Science 330(6006) (2010) 946-948.
[156] S.S. Terdalkar, S. Huang, H. Yuan, J.J. Rencis, T. Zhu, S. Zhang, Nanoscale fracture in graphene, Chemical Physics Letters 494(4-6) (2010) 218-222.
[157] M.-Q. Le, R.C. Batra, Single-edge crack growth in graphene sheets under tension, Computational Materials Science 69 (2013) 381-388.
[158] A. Cao, J. Qu, Atomistic simulation study of brittle failure in nanocrystalline graphene under uniaxial tension, Applied Physics Letters 102(7) (2013) 071902.
[159] X. Wei, S. Xiao, F. Li, D.-M. Tang, Q. Chen, Y. Bando*, et al.*, Comparative fracture toughness of multilayer graphenes and boronitrenes, Nano letters 15(1) (2015) 689-694.
[160] C. Cao, S. Mukherjee, J.Y. Howe, D.D. Perovic, Y. Sun, C.V. Singh*, et al.*, Nonlinear fracture toughness measurement and crack propagation resistance of functionalized graphene multilayers, Science Advances 4(4) (2018) eaao7202.
[161] W.R. Sanhai, J.H. Sakamoto, R. Canady, M. Ferrari, Seven challenges for nanomedicine, Nature nanotechnology 3(5) (2008) 242-244.
[162] F. Soto, A. Martin, S. Ibsen, M. Vaidyanathan, V. Garcia-Gradilla, Y. Levin*, et al.*, Acoustic microcannons: Toward advanced microballistics, ACS nano 10(1) (2015) 1522-1528.
[163] Y. Li, Reversible wrinkles of monolayer graphene on a polymer substrate: toward stretchable and flexible electronics, Soft matter 12(13) (2016) 3202-3213.
[164] D.A. Shockey, J.W. Simons, D.R. Curran, The damage mechanism route to better armor materials, International Journal of Applied Ceramic Technology 7(5) (2010) 566-573.
[165] E. Grossman, I. Gouzman, R. Verker, Debris/micrometeoroid impacts and synergistic effects on spacecraft materials, MRS bulletin 35(01) (2010) 41-47.
[166] J.-H. Lee, P.E. Loya, J. Lou, E.L. Thomas, Dynamic mechanical behavior of multilayer graphene via supersonic projectile penetration, Science 346(6213) (2014) 1092-1096.
[167] W. Xie, S. Tadepalli, S.H. Park, A. Kazemi-Moridani, Q. Jiang, S. Singamaneni*, et al.*, Extreme Mechanical Behavior of Nacre-Mimetic Graphene-Oxide and Silk Nanocomposites, Nano letters (2018).
[168] D. Veysset, A.J. Hsieh, S. Kooi, A.A. Maznev, K.A. Masser, K.A. Nelson, Dynamics of supersonic microparticle impact on elastomers revealed by real–time multi–frame imaging, Scientific reports 6 (2016).
[169] K. Yoon, A. Ostadhossein, A.C. van Duin, Atomistic-scale simulations of the chemomechanical behavior of graphene under nanoprojectile impact, Carbon 99 (2016) 58-64.
[170] Z. Meng, A. Singh, X. Qin, S. Keten, Reduced ballistic limit velocity of graphene membranes due to cone wave reflection, Extreme Mechanics Letters 15 (2017) 70-77.
[171] Z. Meng, J. Han, X. Qin, Y. Zhang, O. Balogun, S. Keten, Spalling-Like Failure by Cylindrical Projectiles Deteriorates the Ballistic Performance of Multi-Layer Graphene Plates, Carbon 126 (2018) 611-619.
[172] S.L. Phoenix, P.K. Porwal, A new membrane model for the ballistic impact response and V 50 performance of multi-ply fibrous systems, International Journal of Solids and Structures 40(24) (2003) 6723-6765.
[173] L. Alonso, C. Navarro, S.K. García-Castillo, Analytical models for the perforation of thick and thin thickness woven-laminates subjected to high-velocity impact, Composites Part B: Engineering (2018).
[174] J. Sha, Y. Li, R. Villegas Salvatierra, T. Wang, P. Dong, Y. Ji*, et al.*, Three-dimensional printed graphene foams, ACS nano 11(7) (2017) 6860-6867.

[175] Z. Shen, H. Ye, C. Zhou, M. Kroeger, Y. Li, Size of Graphene Sheets Determines The Structural and Mechanical Properties of 3D Graphene Foams, Nanotechnology (2018).
[176] C. Wang, D. Pan, S. Chen, Energy dissipative mechanism of graphene foam materials, Carbon (2018).
[177] Z.P. Bažant, F.C. Caner, Comminution of solids caused by kinetic energy of high shear strain rate, with implications for impact, shock, and shale fracturing, Proceedings of the National Academy of Sciences 110(48) (2013) 19291-19294.
[178] Z.P. Bažant, F.C. Caner, Impact comminution of solids due to local kinetic energy of high shear strain rate: I. Continuum theory and turbulence analogy, Journal of the Mechanics and Physics of Solids 64 (2014) 223-235.
[179] F.C. Caner, Z.P. Bažant, Impact comminution of solids due to local kinetic energy of high shear strain rate: II–Microplane model and verification, Journal of the Mechanics and Physics of Solids 64 (2014) 236-248.
[180] J. Awerbuch, S. Bodner, Analysis of the mechanics of perforation of projectiles in metallic plates, International Journal of Solids and Structures 10(6) (1974) 671-684.
[181] M.E. Backman, W. Goldsmith, The mechanics of penetration of projectiles into targets, International Journal of Engineering Science 16(1) (1978) 1-99.
[182] H. Wen, Predicting the penetration and perforation of FRP laminates struck normally by projectiles with different nose shapes, Composite structures 49(3) (2000) 321-329.
[183] I. Mohagheghian, G. McShane, W. Stronge, Impact perforation of polymer–metal laminates: Projectile nose shape sensitivity, International Journal of solids and structures 88 (2016) 337-353.
[184] K. Kpenyigba, T. Jankowiak, A. Rusinek, R. Pesci, Influence of projectile shape on dynamic behavior of steel sheet subjected to impact and perforation, Thin-Walled Structures 65 (2013) 93-104.
[185] K. Kpenyigba, T. Jankowiak, A. Rusinek, R. Pesci, B. Wang, Effect of projectile nose shape on ballistic resistance of interstitial-free steel sheets, International Journal of Impact Engineering 79 (2015) 83-94.
[186] K. Senthil, M. Iqbal, Effect of projectile diameter on ballistic resistance and failure mechanism of single and layered aluminum plates, Theoretical and Applied Fracture Mechanics 67 (2013) 53-64.
[187] D. Grady, The spall strength of condensed matter, Journal of the Mechanics and Physics of Solids 36(3) (1988) 353-384.
[188] M. Ohtsu, F.A. Uddin, W. Tong, K. Murakami, Dynamics of spall failure in fiber reinforced concrete due to blasting, Construction and Building Materials 21(3) (2007) 511-518.
[189] H. Wen, Penetration and perforation of thick FRP laminates, Composites Science and Technology 61(8) (2001) 1163-1172.
[190] G. Wang, Z. Dai, Y. Wang, P. Tan, L. Liu, Z. Xu*, et al.*, Measuring Interlayer Shear Stress in Bilayer Graphene, Physical Review Letters 119(3) (2017) 036101.
[191] Q. Wu, H. Wen, Y. Qin, S. Xin, Perforation of FRP laminates under impact by flat-nosed projectiles, Composites Part B: Engineering 43(2) (2012) 221-227.
[192] R.J. Connolly, The spalling of concrete in fires, Aston University, 1995.
[193] G. Miller, H. Pursey, On the partition of energy between elastic waves in a semi-infinite solid, Proceedings of the Royal Society of London a: mathematical, physical and engineering sciences, The Royal Society, 1955, pp. 55-69.
[194] T. He, H. Wen, Y. Qin, Penetration and perforation of FRP laminates struck transversely by conical-nosed projectiles, Composite structures 81(2) (2007) 243-252.
[195] T. Kuilla, S. Bhadra, D.H. Yao, N.H. Kim, S. Bose, J.H. Lee, Recent advances in graphene based polymer composites, Prog Polym Sci 35(11) (2010) 1350-1375.
[196] H. Chong, S. Hinder, A. Taylor, Graphene nanoplatelet-modified epoxy: effect of aspect ratio and surface functionality on mechanical properties and toughening mechanisms, Journal of materials science 51(19) (2016) 8764-8790.

[197] M. Prolongo, C. Salom, C. Arribas, M. Sánchez-Cabezudo, R. Masegosa, S. Prolongo, Influence of graphene nanoplatelets on curing and mechanical properties of graphene/epoxy nanocomposites, Journal of Thermal Analysis and Calorimetry 125(2) (2016) 629-636.
[198] S. Prolongo, R. Moriche, A. Jiménez-Suárez, M. Sánchez, A. Ureña, Advantages and disadvantages of the addition of graphene nanoplatelets to epoxy resins, European Polymer Journal 61 (2014) 206-214.
[199] X.-J. Shen, Y. Liu, H.-M. Xiao, Q.-P. Feng, Z.-Z. Yu, S.-Y. Fu, The reinforcing effect of graphene nanosheets on the cryogenic mechanical properties of epoxy resins, Composites Science and Technology 72(13) (2012) 1581-1587.
[200] Z. Li, R.J. Young, R. Wang, F. Yang, L. Hao, W. Jiao*, et al.*, The role of functional groups on graphene oxide in epoxy nanocomposites, Polymer 54(21) (2013) 5821-5829.
[201] F. Wang, L.T. Drzal, Y. Qin, Z. Huang, Mechanical properties and thermal conductivity of graphene nanoplatelet/epoxy composites, Journal of materials science 50(3) (2015) 1082-1093.
[202] C. Monteserín, M. Blanco, E. Aranzabe, A. Aranzabe, J.M. Laza, A. Larrañaga-Varga*, et al.*, Effects of Graphene Oxide and Chemically-Reduced Graphene Oxide on the Dynamic Mechanical Properties of Epoxy Amine Composites, Polymers 9(9) (2017) 449.
[203] H. Pang, C. Chen, Y.-C. Zhang, P.-G. Ren, D.-X. Yan, Z.-M. Li, The effect of electric field, annealing temperature and filler loading on the percolation threshold of polystyrene containing carbon nanotubes and graphene nanosheets, Carbon 49(6) (2011) 1980-1988.
[204] R. Rafiq, D. Cai, J. Jin, M. Song, Increasing the toughness of nylon 12 by the incorporation of functionalized graphene, Carbon 48(15) (2010) 4309-4314.
[205] H.-B. Zhang, W.-G. Zheng, Q. Yan, Z.-G. Jiang, Z.-Z. Yu, The effect of surface chemistry of graphene on rheological and electrical properties of polymethylmethacrylate composites, Carbon 50(14) (2012) 5117-5125.
[206] D.R. Bortz, E.G. Heras, I. Martin-Gullon, Impressive fatigue life and fracture toughness improvements in graphene oxide/epoxy composites, Macromolecules 45(1) (2011) 238-245.
[207] Y.-J. Wan, L.-X. Gong, L.-C. Tang, L.-B. Wu, J.-X. Jiang, Mechanical properties of epoxy composites filled with silane-functionalized graphene oxide, Composites Part A: Applied Science and Manufacturing 64 (2014) 79-89.
[208] Y.-J. Wan, L.-C. Tang, L.-X. Gong, D. Yan, Y.-B. Li, L.-B. Wu*, et al.*, Grafting of epoxy chains onto graphene oxide for epoxy composites with improved mechanical and thermal properties, Carbon 69 (2014) 467-480.
[209] Y. Zhang, Y. Wang, J. Yu, L. Chen, J. Zhu, Z. Hu, Tuning the interface of graphene platelets/epoxy composites by the covalent grafting of polybenzimidazole, Polymer 55(19) (2014) 4990-5000.
[210] C. Li, A. Strachan, Molecular dynamics predictions of thermal and mechanical properties of thermoset polymer EPON862/DETDA, Polymer 52(13) (2011) 2920-2928.
[211] C. Li, A. Strachan, Effect of thickness on the thermo-mechanical response of free-standing thermoset nanofilms from molecular dynamics, Macromolecules 44(23) (2011) 9448-9454.
[212] C. Li, G.A. Medvedev, E.-W. Lee, J. Kim, J.M. Caruthers, A. Strachan, Molecular dynamics simulations and experimental studies of the thermomechanical response of an epoxy thermoset polymer, Polymer 53(19) (2012) 4222-4230.
[213] C. Li, E. Jaramillo, A. Strachan, Molecular dynamics simulations on cyclic deformation of an epoxy thermoset, Polymer 54(2) (2013) 881-890.
[214] C. Li, A. Strachan, Molecular simulations of crosslinking process of thermosetting polymers, Polymer 51(25) (2010) 6058-6070.
[215] I. Yarovsky, E. Evans, Computer simulation of structure and properties of crosslinked polymers: application to epoxy resins, Polymer 43(3) (2002) 963-969.
[216] D.R. Heine, G.S. Grest, C.D. Lorenz, M. Tsige, M.J. Stevens, Atomistic simulations of end-linked poly (dimethylsiloxane) networks: structure and relaxation, Macromolecules 37(10) (2004) 3857-3864.

[217] H.B. Fan, M.M. Yuen, Material properties of the cross-linked epoxy resin compound predicted by molecular dynamics simulation, Polymer 48(7) (2007) 2174-2178.
[218] L.J. Abbott, K.E. Hart, C.M. Colina, Polymatic: a generalized simulated polymerization algorithm for amorphous polymers, Theoretical Chemistry Accounts 132(3) (2013) 1-19.
[219] K.S. Khare, F.R. Phelan Jr, Quantitative Comparison of Atomistic Simulations with Experiment for a Cross-Linked Epoxy: A Specific Volume–Cooling Rate Analysis, Macromolecules (2018).
[220] M. William, R. Landel, J. Ferry, The temperature dependence of relaxation mechanisms in amorphous polymers and other glass-forming liquids, J. Am. Chem. Soc. 77(14) (1955) 3701-3707.
[221] J. Kim, T.J. Moon, J.R. Howell, Cure Kinetic Model, Heat of Reaction, and Glass Transition Temperature of AS4/3501-6 Graphite–Epoxy Prepregs, J. Compos. Mater. 36(21) (2002) 2479-2498.
[222] V. Bellenger, J. Verdu, E. Morel, Effect of structure on glass transition temperature of amine crosslinked epoxies, Journal of Polymer Science Part B: Polymer Physics 25(6) (1987) 1219-1234.
[223] J. Pascault, R. Williams, Relationships between glass transition temperature and conversion, Polym. Bull. 24(1) (1990) 115-121.
[224] J. Pascault, R. Williams, Glass transition temperature versus conversion relationships for thermosetting polymers, J. Polym. Sci., Part B: Polym. Phys. 28(1) (1990) 85-95.
[225] M.J. Marks, R.V. Snelgrove, Effect of Conversion on the Structure− Property Relationships of Amine-Cured Epoxy Thermosets, ACS Appl. Mater. Interfaces 1(4) (2009) 921-926.
[226] T.R. Mattsson, J.M.D. Lane, K.R. Cochrane, M.P. Desjarlais, A.P. Thompson, F. Pierce, *et al.*, First-principles and classical molecular dynamics simulation of shocked polymers, Phys Rev B 81(5) (2010) 054103.
[227] S. Yang, Z. Cui, J. Qu, A coarse-grained model for epoxy molding compound, J. Physi. Chem. B 118(6) (2014) 1660-1669.
[228] J. Moller, S. Barr, E. Schultz, T. Breitzman, R. Berry, Simulation of fracture nucleation in cross-linked polymer networks, JOM 65(2) (2013) 147-167.
[229] S. Yang, J. Qu, Coarse-grained molecular dynamics simulations of the tensile behavior of a thermosetting polymer, Phys. Rev. E 90(1) (2014) 012601.
[230] N. Yoshiharu, K. Shigenori, W. Masahisa, O. Takeshi, Cellulose microcrystal film of high uniaxial orientation, Macromolecules 30(20) (1997) 6395-6397.
[231] H. Brown, I. Ward, Craze shape and fracture in poly (methyl methacrylate), Polymer 14(10) (1973) 469-475.
[232] H. Brown, A molecular interpretation of the toughness of glassy polymers, Macromolecules 24(10) (1991) 2752-2756.
[233] C. Hui, A. Ruina, C. Creton, E. Kramer, Micromechanics of crack growth into a craze in a polymer glass, Macromolecules 25(15) (1992) 3948-3955.
[234] Y. Sha, C. Hui, A. Ruina, E. Kramer, Continuum and discrete modeling of craze failure at a crack tip in a glassy polymer, Macromolecules 28(7) (1995) 2450-2459.
[235] Y. Sha, C. Hui, A.a. Ruina, E. Kramer, Detailed simulation of craze fibril failure at a crack tip in a glassy polymer, Acta Mater. 45(9) (1997) 3555-3563.
[236] M.D. Glad, E. Kramer, Microdeformation and network structure in epoxies, J. Mater. Sci. 26(9) (1991) 2273-2286.
[237] H.-H. Kausch, Polymer fracture, Springer -Verlag Berlin Heidelberg1987.
[238] R.J. Morgan, J.E. O'Neal, The microscopic failure processes and their relation to the structure of amine-cured bisphenol-A-diglycidyl ether epoxies, J. Mater. Sci. 12(10) (1977) 1966-1980.
[239] R.J. Morgan, J.E. O'neal, The durability of epoxies, Polym.-Plast. Technol. Eng. 10(1) (1978) 49-116.
[240] R.J. Morgan, E.T. Mones, W.J. Steele, Tensile deformation and failure processes of amine-cured epoxies, Polymer 23(2) (1982) 295-305.

[241] A. Kinloch, Mechanics and mechanisms of fracture of thermosetting epoxy polymers, Epoxy Resins and Composites I, Springer1985, pp. 45-67.
[242] W. Bascom, R. Cottington, R. Jones, P. Peyser, The fracture of epoxy-and elastomer-modified epoxy polymers in bulk and as adhesives, J. Appl. Polym. Sci. 19(9) (1975) 2545-2562.
[243] W. Bascom, R. Ting, R. Moulton, C. Riew, A. Siebert, The fracture of an epoxy polymer containing elastomeric modifiers, J. Mater. Sci. 16(10) (1981) 2657-2664.
[244] F.F. de Nograro, R. Llano-Ponte, I. Mondragon, Dynamic and mechanical properties of epoxy networks obtained with PPO based amines/mPDA mixed curing agents, Polymer 37(9) (1996) 1589-1600.
[245] E. Crawford, A.J. Lesser, The effect of network architecture on the thermal and mechanical behavior of epoxy resins, J. Polym. Sci., Part B: Polym. Phys. 36(8) (1998) 1371-1382.
[246] S. Shin, J. Jang, The effect of amine/epoxy ratio on the fracture toughness of tetrafunctional epoxy resin, Polym. Bull. 39(3) (1997) 353-359.
[247] Q. Sun, Z. Meng, G. Zhou, S.-P. Lin, H. Kang, S. Keten*, et al.*, Multi-Scale Computational Analysis of Unidirectional Carbon Fiber Reinforced Polymer Composites under Various Loading Conditions, Composite Structures 196 (2018) 30-43.
[248] T. Giesa, M.J. Buehler, Nanoconfinement and the Strength of Biopolymers, Annual review of biophysics 42 (2013) 651-673.
[249] H.D. Espinosa, J.E. Rim, F. Barthelat, M.J. Buehler, Merger of structure and material in nacre and bone–Perspectives on de novo biomimetic materials, Progress in Materials Science 54(8) (2009) 1059-1100.
[250] R. Wang, Z. Suo, A. Evans, N. Yao, I. Aksay, Deformation mechanisms in nacre, Journal of Materials Research 16(9) (2001) 2485-2493.
[251] Y. Chen, B. Liu, X. He, Y. Huang, K. Hwang, Failure analysis and the optimal toughness design of carbon nanotube-reinforced composites, Composites Science and Technology 70(9) (2010) 1360-1367.
[252] P. Lawrence, Some theoretical considerations of fibre pull-out from an elastic matrix, Journal of Materials Science 7(1) (1972) 1-6.
[253] T. Vaughan, C. McCarthy, Micromechanical modelling of the transverse damage behaviour in fibre reinforced composites, Composites Science and Technology 71(3) (2011) 388-396.
[254] M. Herráez, C. González, C. Lopes, R.G. de Villoria, J. LLorca, T. Varela*, et al.*, Computational micromechanics evaluation of the effect of fibre shape on the transverse strength of unidirectional composites: an approach to virtual materials design, Composites Part A: Applied Science and Manufacturing 91 (2016) 484-492.
[255] M. Pathan, V. Tagarielli, S. Patsias, Effect of fibre shape and interphase on the anisotropic viscoelastic response of fibre composites, Composite Structures 162 (2017) 156-163.
[256] C. González, J. LLorca, Mechanical behavior of unidirectional fiber-reinforced polymers under transverse compression: microscopic mechanisms and modeling, Composites Science and Technology 67(13) (2007) 2795-2806.
[257] Q. Wu, M. Li, Y. Gu, Y. Li, Z. Zhang, Nano-analysis on the structure and chemical composition of the interphase region in carbon fiber composite, Composites Part A: Applied Science and Manufacturing 56 (2014) 143-149.
[258] P. Upadhyaya, S. Kumar, Micromechanics of stress transfer through the interphase in fiber-reinforced composites, Mechanics of Materials 89 (2015) 190-201.
[259] H. Liu, M. Li, Z.-Y. Lu, Z.-G. Zhang, C.-C. Sun, T. Cui, Multiscale simulation study on the curing reaction and the network structure in a typical epoxy system, Macromolecules 44(21) (2011) 8650-8660.
[260] M. Langeloth, T. Sugii, M.C. Böhm, F. Müller-Plathe, The glass transition in cured epoxy thermosets: A comparative molecular dynamics study in coarse-grained and atomistic resolution, J. Chem. Phys. 143(24) (2015) 243158.

[261] M. Nishikawa, T. Okabe, N. Takeda, Determination of interface properties from experiments on the fragmentation process in single-fiber composites, Materials Science and Engineering: A 480(1) (2008) 549-557.
[262] G. Anagnostopoulos, P.-N. Pappas, Z. Li, I.A. Kinloch, R.J. Young, K.S. Novoselov*, et al.*, Mechanical stability of flexible graphene-based displays, ACS applied materials & interfaces 8(34) (2016) 22605-22614.
[263] R. Yang, A. Zaheri, W. Gao, C. Hayashi, H.D. Espinosa, AFM Identification of Beetle Exocuticle: Bouligand Structure and Nanofiber Anisotropic Elastic Properties, Advanced Functional Materials 27(6) (2017).
[264] N. Guarín-Zapata, J. Gomez, N. Yaraghi, D. Kisailus, P.D. Zavattieri, Shear wave filtering in naturally-occurring Bouligand structures, Acta biomaterialia 23 (2015) 11-20.
[265] G.X. Gu, M. Takaffoli, M.J. Buehler, Hierarchically enhanced impact resistance of bioinspired composites, Advanced Materials 29(28) (2017).